Plasma Physics Reports, Vol. 30, No. 4, 2004, pp. 277–283. Translated from Fizika Plazmy, Vol. 30, No. 4, 2004, pp. 307–313.

TOKAMAKS

The Effect of Error Fields on the Dynamics of a Tearing Mode in a Tokamak

A. M. Kakurin and I. I. Orlovsky

Russian Research Centre Kurchatov Institute, pl. Kurchatova 1, Moscow, 123182 Russia

Received May 14, 2003

Abstract—The features of the tearing mode dynamics in a tokamak that manifest themselves in an irregular mode rotation are demonstrated by using an algorithm for data processing that is based on the concept of the instantaneous frequency of an analytic signal. A model is developed in which the tearing mode is treated as an object to be controlled by means of an external quasistatic magnetic field with an appropriate spatial structure. It is shown that the model dynamics of the mode agrees well with the dynamics of tearing modes observed in experiments in which they are influenced by the magnetic field of the halo current. © *2004 MAIK "Nauka/Interperiodica".*

1. INTRODUCTION

In recent years, tearing-mode instabilities have attracted great interest in connection with work on the designs for large devices, including the ITER tokamak reactor, because the potential danger of triggering neoclassical tearing modes restricts the variety of possible discharge regimes with improved confinement. The situation is aggravated by the fact that a rotating tearing mode can be locked by an external action, so that the rotation slows down and the mode may even stop rotating (the so-called mode locking effect), which often leads to discharge disruption. A possible explanation for this is that, in experimental devices, there exist error fields, one of the spatial harmonics of which may correspond to the tearing mode. This harmonic may affect the instability dynamics and sometimes bring the rotating mode to a stop. One of the most efficient ways of stabilizing the tearing modes is to use a feedback system to control the instability. The development of such systems requires a detailed knowledge of the dynamics of tearing modes in the presence of error fields and the development of a model in which the tearing-mode instability is treated as an object to be controlled.

In tokamaks, the dynamics of tearing modes is usually investigated by means of MHD diagnostics. In classical MHD diagnostics, information about MHD plasma processes is derived by analyzing the signals from magnetic pick-up coils (Mirnov probes). The Mirnov signals have the form of (sometimes nonlinear) oscillations whose frequencies and amplitudes vary over time. These oscillations are associated with the rotation of magnetic islands produced in a plasma due to the onset of tearing-mode instability. Generally, the frequency of the signal oscillations is equal to $f_{MHD} = mf_\theta \pm nf_\phi$, where m and n are the poloidal and toroidal wavenumbers and f_θ and f_ϕ are the frequencies of rotation of the magnetic islands in poloidal and toroidal directions. The sign of the second term is determined by the twist direction of the magnetic field line.

The theory predicts that the tokamak plasma rotates predominantly in the toroidal direction, because its poloidal rotation is rapidly damped by high neoclassical viscosity [1]. This prediction is confirmed by the experimental data from different tokamaks [2, 3]. This is why, when speaking about rotation, we mean precisely the toroidal rotation of the plasma and of magnetic islands, assuming that the frequency of the signal oscillations is equal to $f_{MHD} = nf_\phi$. Because of the helical nature of tearing modes, their toroidal rotation produces the illusion of poloidal rotation with the frequency $f_\theta = (n/m)f_\phi$ when measuring these modes with poloidally arranged Mirnov probes.

The unsteady character of the signals from Mirnov probes considerably complicates their processing by standard spectral methods. For this reason, the methods of the theory of time–frequency distributions (TFD) [4] turn out to be more efficient because they make it possible to follow the time evolution of the frequency spectra.

Modern TFD theory rests on such mathematically rigorous and highly developed methods as the wavelet transform, the windowed Fourier transform, and others. However, these methods are all subject to a serious restriction: they are unable to ensure good spatial and temporal resolution simultaneously, because reduction of the time window used to analyze the spectral distribution leads to a poorer frequency resolution. An alternative approach, free from this restriction, is based on the representation of experimental data in the form of the so-called analytic signal and makes use of the related notion of instantaneous frequency [5, 6].

1063-780X/04/3004-0277$26.00 © 2004 MAIK "Nauka/Interperiodica"

2. ANALYTIC SIGNAL AND THE NOTION OF INSTANTANEOUS FREQUENCY

The analytic signal $z(t)$ is a complex function,

$$z(t) = A(t)\exp(i\varphi(t)) = u(t) + iv(t), \quad (1)$$

whose real part is an original signal $u(t)$ and whose imaginary part is the Hilbert transformed original signal,

$$v(t) = \mathrm{H}[u(t)] = \frac{1}{\pi}\mathrm{v.p.}\int_{-\infty}^{+\infty}\frac{u(\tau)}{t-\tau}d\tau, \quad (2)$$

where v.p. stands for the Cauchy principal value. The relationships

$$A(t) = \sqrt{u^2(t) + v^2(t)}, \quad (3)$$

$$\varphi(t) = \arctan\left(\frac{v(t)}{u(t)}\right), \quad (4)$$

$$f(t) = \frac{1}{2\pi}\frac{d\varphi(t)}{dt} \quad (5)$$

determine, respectively, the amplitude $A(t)$ of the envelope of the signal, its generalized phase $\varphi(t)$, and the instantaneous frequency $f(t)$.

Although the instantaneous frequency is defined for any signal $u(t)$, it is physically meaningful only for the so-called monocomponent signal [7], which has the following two characteristic properties: (i) the number of its local extremes and the number of zeros are either the same or differ by no more than unity and (ii) its upper and lower envelopes are symmetric with respect to its zero level. Such a signal corresponds to an individual (generally nonlinear) oscillatory process whose frequency and amplitude vary over time [8].

In practice, an analytic signal is constructed by using spectral representations. With allowance for the fact that $\mathrm{H}[u(t)]$ is the convolution $u(t) \times 1/\pi t$, the spectral representations satisfy the relationship

$$\mathrm{F}[\mathrm{H}[u(t)]] = \mathrm{F}\left[\frac{1}{\pi t}\right]\mathrm{F}[u(t)] = -i\,\mathrm{sgn}(f)U(f), \quad (6)$$

where $\mathrm{F}[\ldots]$ is the Fourier-transform operator and $U(f)$ is the spectrum of the original signal $u(t)$. In an algorithm that makes use of the spectral representation, the analytic signal $z(t)$ is constructed from the original signal $u(t)$ in accordance with the expressions

$$z(t) = \mathrm{F}^{-1}[(1 + \mathrm{sgn}(f))\mathrm{F}[u(t)]]. \quad (7)$$

It can be seen from this expression that the Fourier spectrum of an analytic signal is nonzero only for positive frequencies.

According to formula (5), the instantaneous frequency is calculated from the expression

$$f(t) = \frac{1}{2\pi}\frac{u(t)v'(t) - u'(t)v(t)}{u^2(t) + v^2(t)}, \quad (8)$$

where the prime denotes the derivative with respect to t.

3. INSTANTANEOUS FREQUENCY AND FEATURES OF THE DYNAMICS OF A TEARING MODE

Let us consider a particular example of how the concept of instantaneous frequency can be used in experiments on studying the locking of a rotating tearing mode in the T-10 tokamak [9]. The mode locking means that the rotation frequency of the $m/n = 2/1$ tearing mode becomes equal to the frequency of the halo current J_{halo} flowing along the rail limiter–plasma–vacuum chamber–high-power amplifier–rail limiter circuit. For a pulse of a unipolar halo current of several hundred amperes flowing through the circuit, mode locking resulted in the stopping of mode rotation. The mechanism underlying this effect is the influence of the corresponding spatial harmonic of the magnetic field of the halo current on the tearing mode dynamics. Here, we focus on the shape and instantaneous frequency of the poloidal magnetic field rather than on the mode locking phenomenon.

In the experiments under review, the working gas was deuterium and the discharge parameters were as follows: the magnetic field was $B_T = 2.5$ T, the discharge current was $I_p = 250$ kA, and the mean plasma density was $\langle n_e\rangle \approx 6 \times 10^{18}$ m^{-3}. The minor plasma radius was determined by the position of the movable rail limiter and was $a = 0.27$ m.

Large-scale perturbations of the poloidal magnetic field due to tearing-mode instability were measured by poloidally arranged Mirnov probes. The fields of the perturbations were expanded in the sine, $B_s(t)$, and cosine, $B_c(t)$, quadrature components of the spatial Fourier harmonics by processing the signals from the probes with the help of analog schemes.

The measurements were carried out in discharge regimes with a steady-state poloidal-field perturbation with an amplitude of $B \approx 8 \times 10^{-4}$ T and a frequency of about 1 kHz. The spatial structure of the perturbation corresponded to the $m/n = 2/1$ tearing mode. The quadrature components shown in Fig. 1 have different shapes and are nonharmonic, while being highly periodic. Figure 1 also shows the instantaneous frequencies $f_c(t)$ and $f_s(t)$ of the components. The good coincidence between $f_c(t)$ and $f_s(t)$ indicates that the instantaneous frequency can be determined from any of the two components.

The shape of the observed oscillations of the quadrature components and the large-amplitude oscillations of the instantaneous frequencies clearly demon-

strate the irregular character of the rotation of magnetic islands during the steady discharge stage, even when the islands do not stop rotating spontaneously. Earlier, an analogous feature of the behavior of magnetic islands in a situation in which they may spontaneously come to a stop was thoroughly investigated in the T-10 tokamak. It was suggested that a possible reason why the islands stop rotating spontaneously is steady-state magnetic perturbations due to imperfections in the assembly of the tokamak magnetic system [10].

The irregular character of the rotation of a tearing mode under the action of the corresponding spatial harmonic of a static magnetic field was also demonstrated theoretically by Fitzpatrick [11].

4. DYNAMIC MODEL OF THE TEARING MODE

In order to describe the behavior of a tearing mode in a tokamak under the action of external currents having a spatial structure similar to that of the mode, we use a single-mode model in which the mode dynamics is described by a set of ordinary differential equations. This fairly efficient approach is often used to analyze systems for controlling the tearing-mode instability in tokamaks [12–14]. The model approach to describing the dynamics of a tearing mode under an external action begins with the following equation for the nonlinear evolution of the mode [15]:

$$\frac{d\psi}{dt} = C\frac{\eta}{\mu_0}\frac{\Delta'(w)}{w}\psi. \qquad (9)$$

Here, ψ is the perturbation of the helical magnetic flux, η is the plasma resistivity, and the width w of the magnetic island is related to the perturbed flux $\psi(r_s)$ at a resonant magnetic surface of radius r_s by the relationship

$$w = 4\sqrt{\frac{q(r_s)\psi(r_s)}{B_P}\left(\frac{dq(r_s)}{dr}\right)^{-1}}, \qquad (10)$$

where $q(r) = (rB_T)/(RB_P)$. In different studies, the values of the coefficient C lie in the range $C \approx 1$–3.

We approximate the function $\Delta'(w)$ by the widely used expression $\Delta'(w) = \Delta'_0(1 - w/w_{st})$, which describes how a magnetic island of width w widens at a progressively decreasing rate until it saturates at $w = w_{st}$. The parameter Δ'_0 is equal to the jump in the logarithmic derivative of ψ at the resonant magnetic surface at which the tearing mode under analysis develops. The effect of an external current on the tearing mode evolution is described through the replacement $\Delta'(w) \longrightarrow \Delta'(w) + \psi^{-1}(r_s)\partial\psi_h(r_s)/\partial r$, where $\psi_h(r)$ is the amplitude of the corresponding spatial harmonic of the helical magnetic flux perturbed by an external current.

The radial and poloidal components of the perturbed magnetic field are related to ψ by the relationships $B_r = (1/r)\partial\psi/\partial\theta$ and $B_\theta = -\partial\psi/\partial r$, respectively. Outside the plasma column, at the radius r_p at which the Mirnov probes are located, the helical magnetic flux perturbation obeys the relationship $\psi(r) \sim r^{-m}$. In the free-boundary plasma problem, the poloidal and radial components of the magnetic field of the tearing mode at this radius have the same amplitude, $B_\theta = B_r = (m/r)\psi$, but their phases are shifted with respect to one another by $\pi/2$. Below, we will denote the poloidal component B_θ by B.

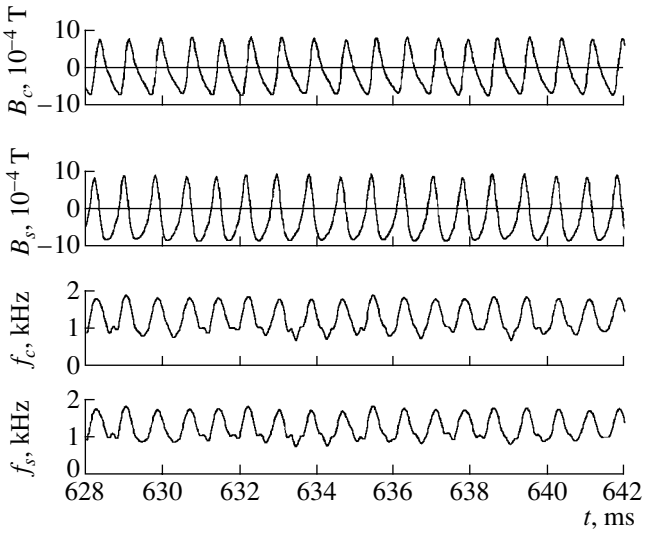

Fig. 1. Evolution of the quadrature components $B_c(t)$ and $B_s(t)$ of the magnetic field and their instantaneous frequencies $f_c(t)$ and $f_s(t)$.

Taking into account the above relationships, we arrive at the following equation describing the evolution of the poloidal magnetic field of the tearing mode at the radius r_p outside the plasma:

$$\frac{dB}{dt} = g\left[\sqrt{\frac{B_{st}}{B}} - 1\right]B + h\sqrt{\frac{B_{st}}{B}}j, \qquad (11)$$

where j [A/m] is the corresponding spatial harmonic of the surface density of the external current at the radius r_c and B_{st} [T] is the perturbed field of the saturated magnetic island. The coefficients in the equation, g [s^{-1}] and h [(T m)/(A s)], depend on r_s, r_c, and r_p and also on the inverse skin time $\omega_R = \eta/(\mu_0 r_s^2)$ and the plasma current density distribution.

Following [12, 17], we account for the plasma rotation by introducing the cosine and sine quadrature components of the poloidal magnetic field of the tearing mode, namely, $B_c(t)$ and $B_s(t)$, whose spatial structures are described by the functions $\cos(m\theta + n\phi)$ and $\sin(m\theta + n\phi)$, respectively. Using Eq. (11), we obtain the following equations for the evolution of these component under an external action:

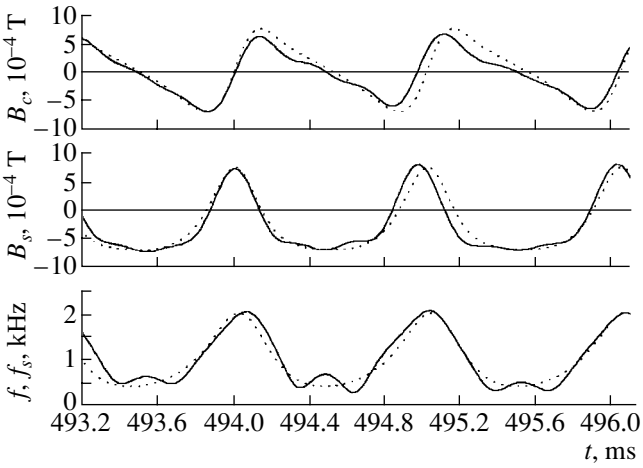

Fig. 2. Comparison of the calculated evolution (dotted curves) of the quadrature components $B_c(t)$ and $B_s(t)$ of the magnetic field and of the instantaneous frequency $f(t)$ with the experimental data (solid curves).

$$\frac{dB_c}{dt} = g\left[\sqrt{\frac{B_{st}}{B}} - 1\right]B_c - n\omega B_s + h\sqrt{\frac{B_{st}}{B}}j_c, \quad (12)$$

$$\frac{dB_s}{dt} = g\left[\sqrt{\frac{B_{st}}{B}} - 1\right]B_s + n\omega B_c + h\sqrt{\frac{B_{st}}{B}}j_s, \quad (13)$$

where $\omega(t)$ is the toroidal rotation frequency of the plasma, $B = (B_c^2 + B_s^2)^{1/2}$, and $j_c(t)$ and $j_s(t)$ are the cosine and sine components of the external current.

In order to describe the evolution of the rotation frequency $\omega(t)$, we apply the approach proposed in [11, 13, 14], in which the motion of the plasma within magnetic islands is considered as a toroidal rotation of a solid body in a viscous medium, with the frequency ω and the angular momentum

$$I = 4\pi^2 R^3 r_s w\rho, \quad (14)$$

where ρ is the plasma density within the island. The body is subjected to a rotational torque in the toroidal direction that arises from the interaction of an external current j with the radial magnetic field B_r of the tearing mode:

$$M_\phi = -R\int B_r j dv. \quad (15)$$

The plasma within the island is also subjected to a frictional torque M_{fr} produced by the frictional force in a plasma that surrounds the island and rotates with the frequency ω_{pl}:

$$M_{fr} = 8\pi^2\frac{\nu}{d}R^3 r_s(\omega_{pl} - \omega), \quad (16)$$

where ν is the plasma viscosity and d is the boundary layer thickness. We take into account the relationship

$$I\frac{d\omega}{dt} = M_\phi + M_{fr}, \quad (17)$$

to see that, in a simple dynamic model, the evolution of the rotation frequency $\omega(t)$ is described by the equation

$$\frac{d\omega}{dt} = p\sqrt{\frac{B_{st}}{B}}(B_s j_c - B_c j_s) + q\sqrt{\frac{B_{st}}{B}}(\omega_{pl} - \omega), \quad (18)$$

where the coefficient p depends on R, r_s, r_p, r_c, w, and ρ and the coefficient q depends on R, r_s, r_p, w, ρ, and ν/d. In model calculations, the ratio ν/d is adjusted to achieve the best possible agreement with experiment.

5. INTERPRETATION OF EXPERIMENTAL DATA AND NUMERICAL RESULTS

As was mentioned above, one of the factors influencing the dynamics of a tearing mode in a tokamak is the presence of error fields that are relatively weak in comparison with the field of the discharge current. One of the spatial harmonics of the error fields may correspond to the spatial structure of the tearing mode developed in the plasma and can thereby affect the mode dynamics. Similar effects were investigated in tokamaks, with emphasis on the remarkable phenomenon known as the spontaneous stopping of rotation [10].

Here, we focus on the relatively weak effect of the external magnetic fields on the tearing mode, as a result of which the rotation of magnetic islands becomes irregular. In order to interpret the experimental data presented above, we carried out a mathematical modeling of the effect of the halo current on the dynamics of a tearing mode in a tokamak discharge with parameters corresponding to those in the experiment. In simulations, we assumed that the effect of the field of the halo current described by the density j_{er} with the quadrature components j_{erc} and j_{ers} is analogous to that of the error fields.

As input to model simulations, we used the experimental parameters $B_T = 2.5$ T, $I_p = 250$ kA, $B_{st} = 8 \times 10^{-4}$ T, $R = 1.5$ m, $a = r_c = 0.27$ m, and $r_p = 0.42$ m. Under the assumption that the plasma current density in the region $r > r_s$ is zero, the radius of the resonant magnetic surface and the island width are estimated to be $r_s \approx 0.24$ m and $w \approx 0.07$ m. Setting the plasma temperature and ion density within the magnetic island equal to $T_e \approx 100$ eV and $n_i \approx 2 \times 10^{18}$ m^{-3}, respectively, and making the same assumption about the distribution of the plasma current density, we obtain the following values of the coefficients in Eqs. (12), (13), and (18): $g \approx 500$ s^{-1}, $h \approx 0.3 \times 10^{-4}$ T/(A s), $p \approx 2.5 \times 10^8$ m/(T A s^2), and $q \approx 10^4$ s^{-1}. In the set of Eqs. (12), (13), and (18), describing the evolution of the fields of the perturbation in terms of these dimensional parameters, the fields are expressed in teslas, the external current density and angular frequency being given in units of A/m and rad/s, respectively. In model computations, we set $\omega_{pl} =$

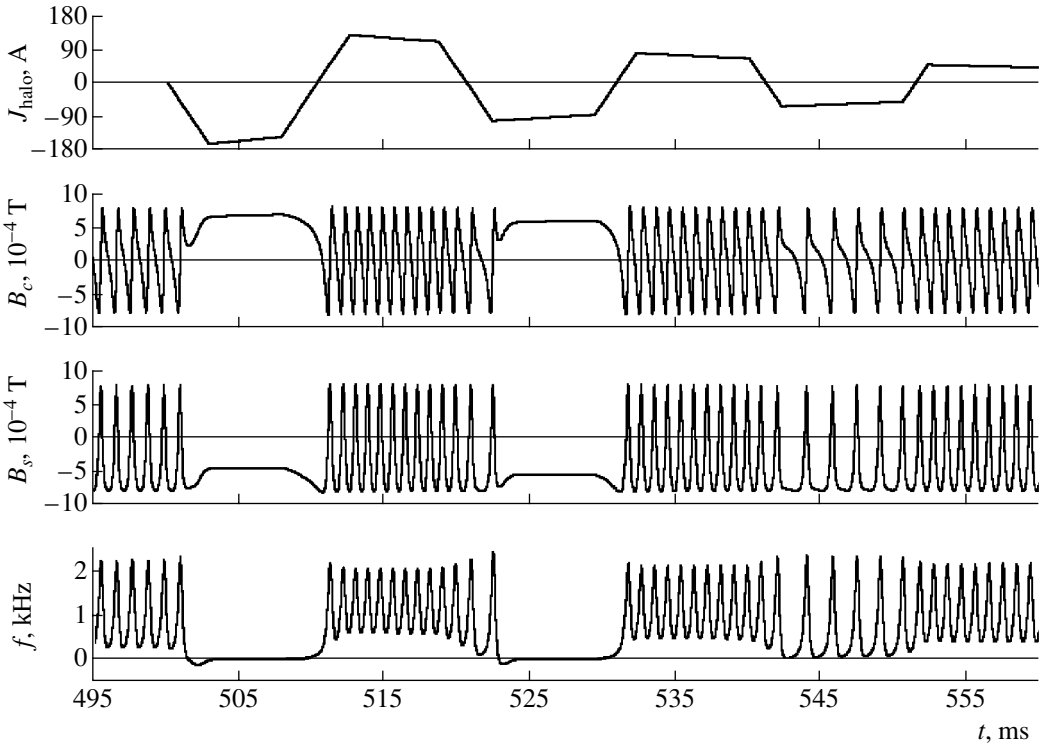

Fig. 3. Evolution of the quadrature components of the magnetic field of the perturbation, $B_c(t)$ and $B_s(t)$, and of the instantaneous frequency $f(t)$, calculated for a given time evolution of the halo current $J_{halo}(t)$.

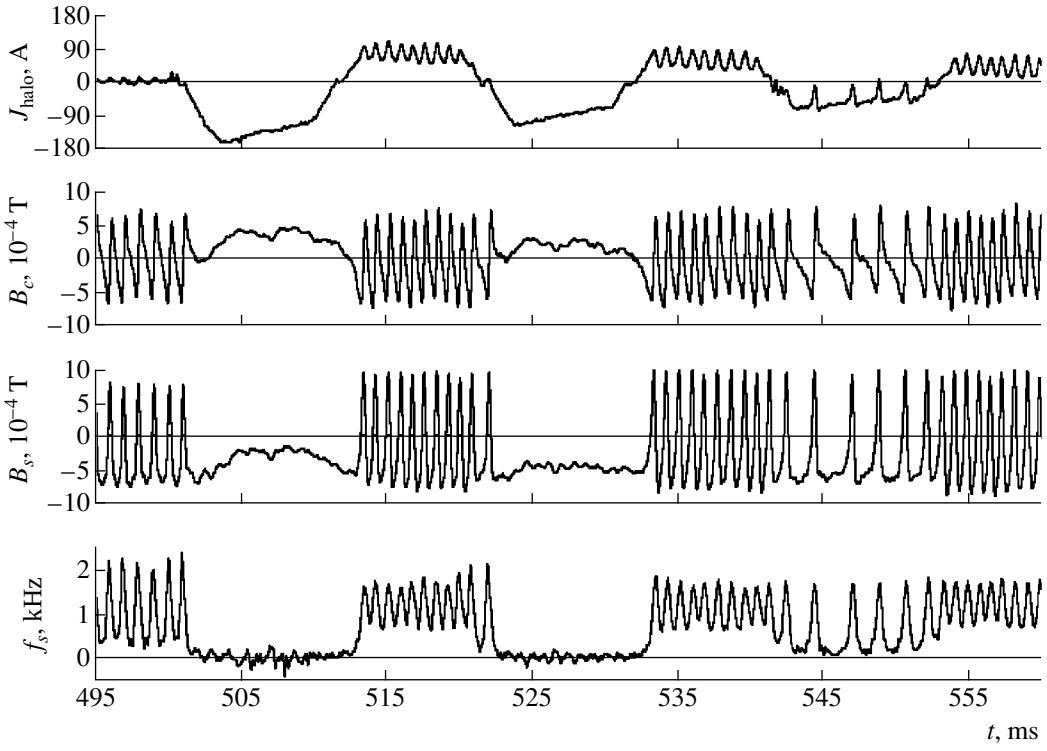

Fig. 4. Evolution of the halo current $J_{halo}(t)$, quadrature components $B_c(t)$ and $B_s(t)$ of the magnetic field of the perturbation, and frequency $f_s(t)$.

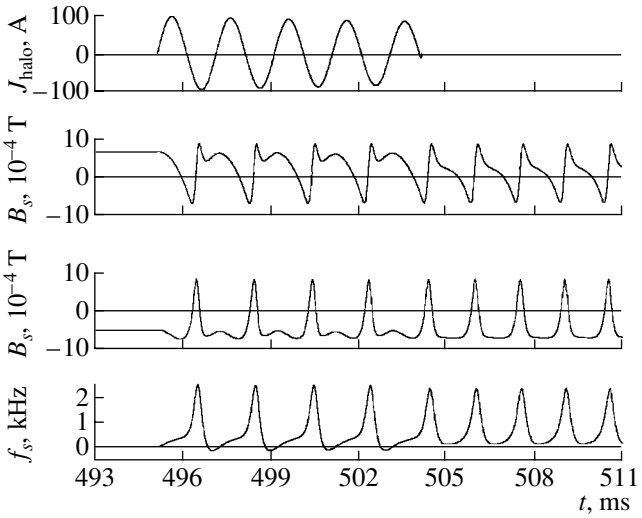

Fig. 5. Numerical simulation of an experiment on the spinup of a tearing mode by an alternating halo current: evolutions of the halo current amplitude $J_{halo}(t)$, quadrature components $B_c(t)$ and $B_s(t)$ of the magnetic field, and instantaneous mode frequency $f(t)$.

8700 rad/s and varied the ratio ν/d in the small vicinity of 2×10^{-6} n s m^{-3}.

The spatial phase and the quantity j_{er} were adjusted so that the calculated shapes of oscillations of the quadrature components of the field B were as close as possible to the experimental shapes. In Fig. 2, the numerically calculated time evolutions of the quadrature components $B_c(t)$ and $B_s(t)$ and of the frequency $f(t) = \omega(t)/2\pi$ are compared with the experimentally obtained evolutions of B_c and B_s and of the instantaneous frequency f_s of the component B_s. In these computations, the poloidal field near the plasma boundary that corresponds to the given value of j_{er} was $\sim 1.5 \times 10^{-3}$ T.

Having adjusted the j_{er} value, we additionally specified the surface current density j_h to correspond to the experimentally measured halo current J_{halo}. The poloidal field near the plasma boundary that corresponds to the maximum amplitude of J_{halo} was $\sim 6 \times 10^{-4}$ T. A comparison of our numerical results (Fig. 3) with the experimental data (Fig. 4) shows good agreement between the numerical and experimental time evolutions of the sine and cosine components of the poloidal magnetic field of the $m/n = 2/1$ tearing mode and between the calculated time evolution of the frequency $f(t) = \omega(t)/2\pi$ and instantaneous frequency $f_s(t)$.

It was because of the low output resistance of the high-power amplifier that the experimentally measured halo current J_{halo} contained an oscillating component that was coherent with the poloidal field oscillations. This phenomenon is analogous to that investigated earlier in the T-10 tokamak—the synchronism between the MHD mode and the current oscillations in a circuit containing a rail limiter connected electrically to the chamber [16]. In those studies, the amplitude of the current oscillations was observed to reach values of about 60 A. When the amplitude of the current was at its maximum value, the MHD mode frequency decreased by 25%. In the case of interest to us, the current oscillation amplitude was as large as 25 A, which, according to [16], corresponds to a deviation in the MHD mode frequency by an amount of 10%. Since, in our model experiment, the frequency deviation was ~ 100%, the oscillating component of J_{halo} was ignored in simulations.

We also applied our dynamic model to simulate experiments that had earlier been carried out in the T-10 tokamak [9], namely, the spinup of a stopped tearing mode by an alternating halo current. The results of these simulations are illustrated in Fig. 5.

6. CONCLUSIONS

The results obtained in this work provide evidence that the method based on the concept of the instantaneous frequency of an analytic signal holds promise for experimental investigation of the dynamics of MHD perturbations. This method can be extended to the case of frequency deviation during the oscillation period, which would make it possible to examine the fine structure of the spectral dynamics of the MHD perturbations.

The dynamic model described above can be used to develop a system for controlling tearing-mode instability. This model has an important feature peculiar to the model developed in [12, 17, 18]: it is capable of describing a forced perturbation in the form of a tearing mode excited by an external current. In this respect, the model is quite different from another widely accepted model in which the rotation of magnetic islands is attributed exclusively to plasma rotation [11, 13, 14]. It should be noted that, for a highly viscous dense plasma, the effect of external fields on the plasma rotation within a magnetic island can be neglected, in which case the model proposed here reduces to that of [12, 17, 18].

ACKNOWLEDGMENTS

We are grateful to V.V. Volkov, N.V. Ivanov, Yu.D. Pavlov, V.D. Pustovitov, and A.N. Chudnovskiĭ for their interest in this study and many fruitful discussions. We would like to acknowledge the T-10 scientific group and operations team for help in carrying out the experiments. This work was supported in part by the Department of Atomic Science and Technology of the RF Ministry of Atomic Industry.

REFERENCES

1. S. P. Hirshman and D. J. Sigmar, Nucl. Fusion **21**, 1079 (1981).

2. O. Kluber, H. Zohm, H. Bruhns, *et al.*, Nucl. Fusion **31**, 907 (1991).
3. T. C. Hender, R. Fitzpatrick, A. W. Morris, *et al.*, Nucl. Fusion **32**, 2091 (1992).
4. L. Cohen, Proc. IEEE **77** (10), 72 (1989).
5. D. E. Vakman and L. A. Vaĭnshteĭn, Usp. Fiz. Nauk **123**, 657 (1977) [Sov. Phys. Usp. **20**, 1002 (1977)].
6. E. D. Taylor, C. Cates, M. E. Mauel, *et al.*, Rev. Sci. Instrum. **70**, 4545 (1999).
7. L. Cohen, *Time-Frequency Analysis* (Prentice-Hall, Englewood Cliffs, 1995).
8. N. E. Huang, Z. Shen, S. Long, *et al.*, Proc. R. Soc. London, Ser. A **454**, 903 (1998).
9. N. V. Ivanov, A. N. Chudnovskiy, A. M. Kakurin, *et al.*, in *Proceedings of the 19th IAEA Fusion Energy Conference, Lyon, 2002* (IAEA, Vienna, 2002), Report EX/S2-3.
10. V. V. Volkov, N. V. Ivanov, A. M. Kakurin, *et al.*, Fiz. Plazmy **21**, 931 (1995) [Plasma Phys. Rep. **21**, 881 (1995)].
11. R. Fitzpatrick, Nucl. Fusion **33**, 1049 (1993).
12. A. M. Kakurin, Vopr. At. Nauki Tekh., Ser. Termoyad. Sint., No. 3, 40 (1987).
13. G. Bosia and E. Lazzaro, Nucl. Fusion **31**, 1003 (1991).
14. P. Savrukhin, D. J. Campbell, M. DeBenedetti, *et al.*, Joint European Torus (JET) Report, JET-R(95)-06 (1995).
15. R. B. White, D. A. Monticello, M. N. Rothenbluth, and B. V. Waddel, Phys. Fluids **20**, 800 (1977).
16. N. V. Ivanov, A. N. Chudnovskiy, Yu. V. Gvozdkov, *et al.*, in *Proceedings of the 18th IAEA Fusion Energy Conference, Sorrento, 2000* (IAEA, Vienna, 2001), CD-ROM file No. Exp2_02.
17. Yu. V. Gvozdkov, N. V. Ivanov, and A. M. Kakurin, Fiz. Plazmy **6**, 234 (1980) [Sov. J. Plasma Phys. **6**, 130 (1980)].
18. N. V. Ivanov and A. M. Kakurin, Fiz. Plazmy **5**, 969 (1979) [Sov. J. Plasma Phys. **5**, 541 (1979)].

Translated by O.E. Khadin

Plasma Physics Reports, Vol. 30, No. 4, 2004, pp. 284–298. Translated from Fizika Plazmy, Vol. 30, No. 4, 2004, pp. 314–329.

DUSTY PLASMA

Dissipative Processes during the Propagation of Nonlinear Dust Ion-Acoustic Perturbations

S. I. Popel*, S. N. Andreev, A. A. Gisko**, A. P. Golub'*, and T. V. Losseva***

** Institute of Geosphere Dynamics, Russian Academy of Sciences, Leninskiĭ pr. 38-1, Moscow, 119334 Russia*

*** Prokhorov Institute of General Physics, Russian Academy of Sciences, ul. Vavilova 38, Moscow, 119991 Russia*

Received August 1, 2003

Abstract—A comparative analysis of various dissipative processes occurring on ion-acoustic time scales during the excitation and propagation of nonlinear dust ion-acoustic perturbations in a complex (dusty) plasma is performed in terms of a purely kinetic approach and a hydrodynamic approach. It is found that the most important dissipative processes are the charging of dust grains, the absorption of ions by grains, the transfer of the ion momentum to the grains, and Landau damping. The damping rate of dust ion-acoustic waves is derived based on a purely kinetic approach to describing complex plasmas; this makes it possible to eliminate all of the earlier contradictions in the description of Landau damping in a complex plasma. The relative roles played by dissipative processes in different laboratory experiments with dusty plasmas are compared. © *2004 MAIK "Nauka/Interperiodica".*

1. INTRODUCTION

At present, the problem of the excitation and propagation of nonlinear ion-acoustic perturbations occupies an important place in the physics of complex (dusty) plasma. Since 1996, dust ion-acoustic shock-wave and soliton-like structures have been actively studied both theoretically [1–7] and experimentally [8–10]. Interest in this kind of research is associated primarily with the fact that the processes of dust grain charging are far from equilibrium precisely on ion-acoustic time scales, so that the anomalous dissipation, which, by its very nature, originates from the charging process, often plays a decisive role [1, 11]. It is this anomalous dissipation mechanism that is responsible for the existence of a new kind of shock wave that is "collisionless" in the sense that it is almost completely insensitive to electron–ion collisions. However, in contrast to classical collisionless shock waves, the dissipation due to dust charging involves interaction of electrons and ions with dust grains through microscopic electron and ion currents to the grain surfaces. This anomalous dissipation plays a very important role in the propagation of the so-called "weakly dissipative" dust ion-acoustic solitons [7], whose shape is described by soliton solutions in a certain range of values of the Mach number. Because of anomalous dissipation, these solitons are slowed down and damped.

Dust structures are usually described theoretically by solving a set of hydrodynamic equations that is specially derived for a complex plasma from the kinetic equations for electrons, ions, and dust grains [12]. Of course, in this derivation, such an important, purely kinetic effect as Landau damping is not taken into consideration. However, there is indirect evidence that, in some situations, Landau damping can play an important role. Thus, in a paper by Luo *et al.* [9], the fact that, in laboratory experiments at the University of Iowa, dust ion-acoustic waves were not observed at quite low dust densities was attributed precisely to this damping.

It should be noted that there are different approaches to describing Landau damping. First of all, we must mention the papers in which the corresponding damping rates were calculated without allowance for grain charging (see, e.g., [13]). As early as 1993 [11], it became clear that the charging of dust grains has a significant impact on the damping described at the kinetic level (which will be referred to below as kinetic damping), part of which is Landau damping. Consequently, dust grain charging should be taken into account in calculations. Nevertheless, theoretical studies (see, e.g., [9, 14]) are still often conducted based on the results of [13], in particular, because the expression for the kinetic damping rate of ion-acoustic waves that takes dust grain charging into account and could be used to analyze the results of dusty plasma experiments has not yet been derived in a compact form. As for the results that are presented in [11, 15] and could be used to calculate the corresponding damping rates, they either have a complicated integro-operator form or refer to limiting cases irrelevant to the present-day experiments. Moreover, in [11, 15], the final formula for the dielectric function of a dusty plasma, which is important for deriving the expression for the kinetic damping rate, involves contradictions. All this goes to show that it is necessary to refine the expression for the kinetic damping rate of dust ion-acoustic waves and to reduce it to a compact form convenient for analyzing the experimental results.

1063-780X/04/3004-0284$26.00 © 2004 MAIK "Nauka/Interperiodica"

Since dissipation is one of the processes that play a key role in the formation and propagation of such nonlinear structures as shock waves and solitons, the hydrodynamic approach to describing these structures is valid only if the dissipative processes that are taken into account in the hydrodynamic equations turn out to be more important than Landau damping. Hence, it is important to classify dissipative processes and determine the ranges of plasma parameters in which some particular processes dominate.

Our objective here is to analyze the dissipative processes that occur during the propagation of ion-acoustic structures in a dusty plasma. In Section 2, we derive an expression for the kinetic damping rate of the ion-acoustic waves on the basis of a purely kinetic approach to describing a dusty plasma. In Section 3, we analyze anomalous dissipative processes in terms of hydrodynamic equations, which are usually used to describe nonlinear dust ion-acoustic structures. In Section 4, we describe the main results of experiments that have so far been carried out on the generation of dust ion-acoustic shock waves. We also present the results of numerical simulations of shock waves in these experiments by means of a hydrodynamic ionization source model. In Section 5, we investigate the effect of kinetic damping and compare this effect with the relative effects of anomalous dissipative processes in different experiments with nonlinear dust ion-acoustic structures. In Section 6, we summarize the main results and conclusions of our study.

2. KINETIC DAMPING OF DUST ION-ACOUSTIC WAVES

The dust ion-acoustic mode in a complex plasma is analogous to the ion-acoustic mode in a conventional two-component plasma consisting of electrons and one ion species. The difference in the dispersion relations for the modes is explained as being due to the effects peculiar to dusty plasmas (processes at the surfaces of dust grains, fluctuations of the grain charges, recombination of electrons and ions on the grain surfaces, etc.). An essential feature of dust ion-acoustic waves is that they can exist at $T_e \sim T_i$, where $T_{e(i)}$ is the plasma electron (ion) temperature [16]. We present the derivation of a dispersion relation and expressions for the kinetic damping rate of dust ion-acoustic waves on the basis of a standard, purely kinetic approach, with the use of the method developed by Tsytovich and de Angelis [15].

2.1. Dielectric Function

We begin with the derivation of an expression for the dielectric function of a dusty plasma. Since we are interested here in ion-acoustic time scales, each dust grain can be considered to be immobile. We assume that the grains are influenced by an electrostatic field (the extent of this influence is determined by the variable grain charge q) and also by the plasma particles (electrons and ions). The cross section for the interaction of plasma particles with dust grains is given by the formula (see, e.g., [17])

$$\begin{cases} \sigma_\alpha = \pi a^2 (1 - 2e_\alpha q / a m_\alpha |\mathbf{v}_\alpha|^2) \\ \text{for} \quad 2e_\alpha q / a m_\alpha |\mathbf{v}_\alpha|^2 < 1 \\ \sigma_\alpha = 0, \quad \text{for} \quad 2e_\alpha q / a m_\alpha |\mathbf{v}_\alpha|^2 \geq 1. \end{cases} \tag{1}$$

Here, a is the grain size; e_α, m_α, and v_α are the charge, mass, and velocity of plasma particles of species α; and the subscript $\alpha = e, i$ stands for the electrons and ions, respectively.

The distribution function of the plasma particles of species $f_\alpha(t, \mathbf{r}, \mathbf{p})$ is chosen to be normalized to their density n_α as follows:

$$n_\alpha = \int f_\alpha(t, \mathbf{r}, \mathbf{p}) \frac{d^3\mathbf{p}}{(2\pi)^3}. \tag{2}$$

Since the dust grains are assumed to be immobile, their distribution function depends only on their charge q, $f_d(q)$. The normalization of the grain distribution function is chosen to satisfy the relationship

$$n_d = \int f_d(q) dq, \tag{3}$$

where n_d is the dust density.

The distribution function of dust grains can be represented as the sum of the unperturbed function $\Phi_d = \langle f_d \rangle$ and the perturbation δf_d, which is induced, e.g., by the electric field of a dust ion-acoustic wave. Here, the angle brackets stand for averaging over the statistical ensemble. Since the distribution of plasma particles is also perturbed in their interaction with dust grains, we can write

$$f_\alpha = \Phi_\alpha + \delta f_\alpha, \quad \Phi_\alpha = \langle f_\alpha \rangle. \tag{4}$$

The currents to a dust grain can also be represented as the sum of the unperturbed and perturbed components.

The interaction of plasma electrons and ions with dust grains is described by the equation

$$\left(\frac{\partial}{\partial t} + \mathbf{v}\frac{\partial}{\partial \mathbf{r}} + e_\alpha \mathbf{E}\frac{\partial}{\partial \mathbf{p}}\right) f_\alpha = S_\alpha - \int \sigma_\alpha(q, \mathbf{v}) |\mathbf{v}| f_d(q) f_\alpha dq, \tag{5}$$

where the terms S_α account for all external sources of the particles of species α.

The kinetic equation for dust grains has the form

$$\frac{\partial f_d}{\partial t} + \frac{\partial}{\partial q}\left(I_{\text{ext}} + \sum_\alpha I_\alpha\right) f_d = 0, \tag{6}$$

where $I_\alpha(q, \mathbf{r}, t)$ are the electron and ion currents to a grain at the point $\mathbf{r}$ and at the time t. The remaining currents, which are generated, e.g., by the photoelectric effect and/or secondary electron emission, are incorporated into the term I_{ext}.

The currents to a dust grain of charge q at the point $\mathbf{r}$ can be determined using interaction cross sections (1):

$$I_\alpha(q, \mathbf{r}, t) = \int e_\alpha \sigma_\alpha(q, \mathbf{v})|\mathbf{v}| f_\alpha(t, \mathbf{r}, \mathbf{p}) \frac{d^3\mathbf{p}}{(2\pi)^3}. \quad (7)$$

The equation for the unperturbed distribution function of the plasma particles can be written as

$$\left(\frac{\partial}{\partial t} + \mathbf{v}\frac{\partial}{\partial \mathbf{r}}\right)\Phi_\alpha = S_\alpha - \nu_{d,\alpha} f_\alpha + J_\alpha, \quad (8)$$

where

$$\nu_{d,\alpha} = \int \sigma_\alpha(q, \mathbf{v})|\mathbf{v}|\Phi_d(q)dq, \quad (9)$$

and the collision integral J_α has the form

$$J_\alpha = -e_\alpha\left\langle \delta\mathbf{E}\frac{\partial \delta f_\alpha}{\partial \mathbf{p}}\right\rangle - \int |\mathbf{v}|\sigma_\alpha(q, \mathbf{v})\langle \delta f_\alpha \delta f_d(q)\rangle dq. \quad (10)$$

For the perturbed distribution function, we obtain

$$\left(\frac{\partial}{\partial t} + \mathbf{v}\frac{\partial}{\partial \mathbf{r}}\right)\delta f_\alpha = -e_\alpha \delta\mathbf{E}\frac{\partial \Phi_\alpha}{\partial \mathbf{p}} - e_\alpha\left(\delta\mathbf{E}\frac{\partial \delta f_\alpha}{\partial \mathbf{p}} - \left\langle \delta\mathbf{E}\frac{\partial \delta f_\alpha}{\partial \mathbf{p}}\right\rangle\right) - \int |\mathbf{v}|\sigma_\alpha(q, \mathbf{v})(\Phi_d(q)\delta f_\alpha + \delta f_d(q)\Phi_\alpha + \delta f_d(q) f_\alpha - \langle \delta f_\alpha \delta f_d(q)\rangle)dq. \quad (11)$$

We ignore the nonlinear terms in the equation for the perturbed distribution function and assume that the terms containing the perturbed quantities change only slightly over time. As a result, we arrive at the following equation for the Fourier components:

$$\delta f_{\alpha,\mathbf{k},\omega} = \frac{1}{i(\omega - \mathbf{k}\cdot\mathbf{v} + i\nu_{d,\alpha})} \times\left(e_\alpha \delta\mathbf{E}_{\mathbf{k},\omega}\frac{\partial \Phi_{\alpha,\mathbf{p}}}{\partial \mathbf{p}} + \delta\nu_{d,\alpha,\mathbf{k},\omega}\Phi_{\alpha,\mathbf{p}}\right), \quad (12)$$

where $\delta\nu_{d,\alpha,\mathbf{k},\omega} = \int |\mathbf{v}|\sigma_\alpha(q, \mathbf{v})\delta f_d(q)dq$.

The unperturbed part of the distribution function of the dust grains is given by the equation

$$\frac{\partial \Phi_d}{\partial t} = -\frac{\partial}{\partial q}\left(\left(I_{ext} + \sum_\alpha \langle I_\alpha(q)\rangle\right)\Phi_d + \sum_\alpha \langle \delta I_\alpha(q)\delta f_d(q)\rangle\right), \quad (13)$$

whose right-hand side describes the kinetics of dust charging.

Assuming that all the currents to a dust grain, except for the currents of the plasma electrons and ions, are unperturbed, we obtain from kinetic equation (6) the following equation for the perturbed part of the distribution function of the dust grains:

$$\frac{\partial \delta f_d}{\partial t} = -\frac{\partial}{\partial q}\left(\left(I_{ext} + \sum_\alpha \langle I_\alpha(q)\rangle\right)\delta f_d(q) + \sum_\alpha \delta I_\alpha(q)\Phi_d(q) + \sum_\alpha \delta I_\alpha(q)\delta f_d(q) - \sum_\alpha \langle \delta I_\alpha(q)\delta f_d(q)\rangle\right). \quad (14)$$

Again, we ignore the nonlinear terms and assume that the terms containing the perturbed quantities are nearly constant over time in order to arrive at the following expression for the Fourier component of the perturbed distribution function of the dust grains:

$$i\omega(\delta f_{d,\mathbf{k},\omega}(q)) - \frac{\partial}{\partial q}\left[\left(I_{ext} + \sum_\alpha \langle I_\alpha(q)\rangle\right)\delta f_{d,\mathbf{k},\omega}\right] = \frac{\partial}{\partial q}\left[\left(\sum_\alpha \delta I_{\alpha,\mathbf{k},\omega}(q)\right)\Phi_d\right], \quad (15)$$

where

$$\delta I_{\alpha,\mathbf{k},\omega}(q) = \int e_\alpha |\mathbf{v}|\sigma_\alpha(q, \mathbf{v})\delta f_{\alpha,\mathbf{k},\omega}\frac{d^3\mathbf{p}}{(2\pi)^3}. \quad (16)$$

Equations (12) and (15) constitute a set of equations for describing the perturbations of the plasma and of the dust.

The general solution δf_d to Eq. (15) is the sum of the homogeneous solution $\delta f_d^{(0)}$, which satisfies Eq. (15) with zero on the right-hand side and describes free fluctuations of the dust grain charges, and the inhomogeneous solution $\delta f_d^{(ind)}$, which describes the perturbations of the dust distribution function that are induced by the electric field of a dust ion-acoustic wave and by the perturbed currents to the grain surfaces. To deter-

mine the plasma dielectric function, it is sufficient to take into account only the perturbed distribution function $\delta f_d^{(\mathrm{ind})}$. Hence, in what follows, we will assume that $\delta f_d = \delta f_d^{(\mathrm{ind})}$.

In order to solve Eq. (15), we consider an equation determining the equilibrium charge q_0 of a grain, i.e., the charge at which the averaged current to the grain surface vanishes:

$$I_{\mathrm{ext}} + \sum_\alpha \langle I_\alpha(q_0)\rangle = I_{\mathrm{ext}} + \sum_\alpha \int e_\alpha |\mathbf{v}| \sigma_\alpha(q_0, \mathbf{v}) \Phi_\alpha \frac{d^3\mathbf{p}}{(2\pi)^3} = 0. \quad (17)$$

If we regard the quantity $\Delta q = q - q_0$ as a new variable, then, for small Δq values, we can use the expansion

$$I_{\mathrm{ext}} + \sum_\alpha \langle I_\alpha(q_0)\rangle \approx \Delta q \frac{\partial}{\partial q} \sum_\alpha \langle I_\alpha(q)\rangle\big|_{q=q_0}. \quad (18)$$

We introduce the slowly varying rate of charging ν_q through the standard relationship [17]

$$\nu_q = -\frac{\partial}{\partial q} \sum_\alpha \langle I_\alpha(q)\rangle\big|_{q=q_0}. \quad (19)$$

In terms of charging rate (19), the dynamic equation for the charge of a dust grain, $\dot q = I_{\mathrm{ext}} + \sum_\alpha I_\alpha = 0$, has the form

$$\Delta \dot q = -\nu_q \Delta q, \quad (20)$$

and Eq. (15) becomes

$$\left(\frac{i\omega}{\nu_q} + \frac{\partial}{\partial \bar q}\right)\delta f_{d,\mathbf{k},\omega} = \frac{1}{\nu_q} R_{\mathbf{k},\omega}(q), \quad (21)$$

where $R_{\mathbf{k},\omega}(q)$ denotes the right-hand side of Eq. (15) and $\bar q = \Delta q/\Delta q_{t=0}$. The quantity $\Delta q_{t=0}$ is the solution to Eq. (20) at the initial time $t = 0$ and has the meaning of the initial charge of a dust grain.

The solution to inhomogeneous equation (21) can be written in terms of Green's function:

$$\delta f_{d,\mathbf{k},\omega} = \hat G R_{\mathbf{k},\omega}(q) = \int G(q, q', \omega) R_{\mathbf{k},\omega}(q') dq'. \quad (22)$$

Since $R_{\mathbf{k},\omega}(q) = (\partial/\partial q)\{(\sum_\alpha \delta I_{\alpha,\mathbf{k},\omega}(q))\Phi_d\}$ is the total derivative with respect to q, the Green's function has the form [15]

$$G(q, q', \omega) = \frac{1}{i(\omega + i\nu_q)}. \quad (23)$$

The perturbed currents to a dust grain are described by an integral equation that can be solved approximately under the condition that the charge of the dust grains is close to the equilibrium charge. Using expression (16) and Eq. (12), we get

$$\sum_\alpha \delta I_{\alpha,\mathbf{k},\omega}(q) = S_{\mathbf{k},\omega}(q)\delta E_{\mathbf{k},\omega} + \int \tilde S_{\mathbf{k},\omega}(q, q')\delta f_d(q') dq, \quad (24)$$

where $\mathbf{E}_{\mathbf{k},\omega} = (\mathbf{k}/k)E_{\mathbf{k},\omega}$ and

$$S_{\mathbf{k},\omega}(q) = \sum_\alpha \int \frac{\sigma_\alpha(q, \mathbf{v}) e_\alpha^2 |\mathbf{v}|}{i(\omega - \mathbf{k}\cdot\mathbf{v} + i\nu_{d,\alpha}(\mathbf{v}))} \times \left(\frac{\mathbf{k}}{|\mathbf{k}|}\cdot\frac{\partial \Phi_\alpha}{\partial \mathbf{p}}\right)\frac{d^3\mathbf{p}}{(2\pi)^3}, \quad (25)$$

$$\tilde S_{\mathbf{k},\omega}(q, q') = \sum_\alpha \int \frac{\sigma_\alpha(q, \mathbf{v}) e_\alpha^2 |\mathbf{v}| \sigma_\alpha(q', \mathbf{v})}{i(\omega - \mathbf{k}\cdot\mathbf{v} + i\nu_{d,\alpha}(\mathbf{v}))} \Phi_\alpha \frac{d^3\mathbf{p}}{(2\pi)^3}. \quad (26)$$

Substituting solution (22) into formula (24) and integrating over q' under the assumption that the charge of the dust grains is nearly equilibrium, we obtain an algebraic equation for $\sum_\alpha \delta I_{\alpha,\mathbf{k},\omega}(q)$. The solution to this equation has the form

$$\sum_\alpha \delta I_{\alpha,\mathbf{k},\omega}(q) = \beta_{\mathbf{k},\omega}\delta E_{\mathbf{k},\omega}, \quad (27)$$

where

$$\beta_{\mathbf{k},\omega} = \frac{S_{\mathbf{k},\omega}(q_{\mathrm{eq}})}{1 - \tilde S'_{\mathbf{k},\omega}(q_0)\chi_{\mathbf{k},\omega}}, \quad (28)$$

and where we have introduced the notation

$$\tilde S'_{\mathbf{k},\omega}(q_0) = \sum_\alpha \int \frac{\sigma_\alpha(q_0, \mathbf{v}) e_\alpha |\mathbf{v}|^2}{i(\omega - \mathbf{k}\cdot\mathbf{v} + i\nu_{d,\alpha}(\mathbf{v}))} \times \left.\frac{\partial \sigma_\alpha(q, \mathbf{v})}{\partial q}\right|_{q=q_0} \Phi_\alpha \frac{d^3\mathbf{p}}{(2\pi)^3}, \quad (29)$$

$$\chi_{\mathbf{k},\omega} = \frac{in_d}{\omega + i\nu_q}. \quad (30)$$

Inserting solution (27) into solution (22) and expressing $\delta f_{d,\mathbf{k},\omega}$ in terms of $\delta E_{\mathbf{k},\omega}$, we reduce Eq. (12)

for the perturbed distribution function of the plasma particles to

$$\delta f_{\alpha,\mathbf{k},\omega} = \frac{\delta E_{\mathbf{k},\omega}}{i(\omega - \mathbf{k}\cdot\mathbf{v} + i\nu_{d,\alpha})}\left\{e_\alpha\left(\frac{\mathbf{k}}{|\mathbf{k}|}\cdot\frac{\partial\Phi_\alpha}{\partial\mathbf{p}}\right)\right.$$
$$\left. - \Phi_\alpha\beta_{\mathbf{k},\omega}|\mathbf{v}|\frac{\partial\sigma_\alpha(q,\mathbf{v})}{\partial q}\right|_{q=q_0}\frac{n_d}{i(\omega + i\nu_q)}\Bigg\}. \quad (31)$$

Using Poisson's equation

$$\nabla\cdot\mathbf{E} = 4\pi\sum_\alpha\int e_\alpha f_\alpha\frac{d^3\mathbf{p}}{(2\pi)^3} + 4\pi\int q' f_d dq', \quad (32)$$

we arrive at the equation

$$i|\mathbf{k}|\delta E_{\mathbf{k},\omega} = 4\pi\sum_\alpha\int e_\alpha\delta f_{\alpha,\mathbf{k},\omega}\frac{d^3\mathbf{p}}{(2\pi)^3} + 4\pi\int q'\delta f_{d,\mathbf{k},\omega}dq', \quad (33)$$

which can be rewritten as $i\varepsilon_{\mathbf{k},\omega}|\mathbf{k}|\delta E_{\mathbf{k},\omega} = 0$, where the dielectric function $\varepsilon_{\mathbf{k},\omega}$ of the dusty plasma is given by the formula

$$\varepsilon_{\mathbf{k},\omega} = 1 + \sum_\alpha\int\frac{4\pi e_\alpha^2}{|\mathbf{k}|^2(\omega - \mathbf{k}\cdot\mathbf{v} + i\nu_{d,\alpha})}$$
$$\times\left(\mathbf{k}\cdot\frac{\partial\Phi_\alpha}{\partial\mathbf{p}}\right)\frac{d^3\mathbf{p}}{(2\pi)^3} + \frac{4\pi}{|\mathbf{k}|}\frac{n_d}{(\omega + i\nu_q)}\beta_{\mathbf{k},\omega}\Bigg(-1 \quad (34)$$
$$+ i\sum_\alpha\int\frac{e_\alpha|\mathbf{v}|\Phi_\alpha}{(\omega - \mathbf{k}\cdot\mathbf{v} + i\nu_{d,\alpha})}\frac{\partial\sigma_\alpha(q,\mathbf{v})}{\partial q}\Bigg|_{q=q_0}\frac{d^3\mathbf{p}}{(2\pi)^3}\Bigg).$$

In the notation of Tsytovich and Havnes [11], expression (34) coincides with the expression presented by them for the dielectric function of a dusty plasma. Note that, in paper [15] by Tsytovich and de Angelis, the more general expression for $\varepsilon_{\mathbf{k},\omega}$ contains a misprint: the sign between the terms in the brackets in the second row of formula (55) is incorrect. In particular, for dust grains with a zero velocity, formula (55) of [15] does not pass over to the formula that was obtained earlier in [11] for the dielectric function of a dusty plasma.

2.2. Kinetic Damping Rate

The expression for the damping rate of the dust ion-acoustic waves can be derived using formula (34). We will restrict ourselves to considering Maxwellian equilibrium distribution functions Φ_α. The unperturbed charge q_0 of a dust grain is determined from Eq. (17), which, in the case at hand, has the form

$$\frac{\omega_{pe}^2}{v_{Te}}\exp(-z_0) = \frac{\omega_{pi}^2}{v_{Ti}}(t + z_0), \quad (35)$$

where $t = T_i/T_e$, $z = Z_d e^2/aT_e$, $-e$ is the charge of an electron, $q = -Z_d e$, $\omega_{p\alpha}^2 = 4\pi n_{\alpha 0}e^2/m_\alpha$, $v_{T\alpha}^2 = T_\alpha/m_\alpha$, and the subscript 0 specifies unperturbed values of the quantities. The equilibrium charging rate of the dust grains is described by the expression (see, e.g., [17])

$$\nu_q = \frac{\omega_{pi}^2 a(1 + t + z_0)}{\sqrt{2\pi}v_{Ti}}. \quad (36)$$

Our objective here is to investigate the dispersion relation $\varepsilon_{\mathbf{k},\omega} = 0$ in the frequency range $|\mathbf{k}|v_{Ti} \ll \omega \ll |\mathbf{k}|v_{Te}$ of ion-acoustic waves. This will be done by using the following small parameters:

$$\xi_e = \frac{\omega}{|\mathbf{k}|v_{Te}} \ll 1, \quad \xi_i^{-1} = \frac{|\mathbf{k}|v_{Ti}}{\omega} \ll 1,$$
$$\xi_{\mathrm{dw}} = \frac{\pi a^2 n_d}{|\mathbf{k}|} \ll 1. \quad (37)$$

The last small parameter has a simple physical meaning: it implies that the perturbation wavelength does not exceed the mean free path of dust grains with respect to their interaction with one another. The assumption that this parameter is small is quite justified because, on ion-acoustic time scales, the dust grains can be treated as being immobile. We also assume that the charging rate of the dust grains is much less than the wave frequency, $\nu_q \ll \omega$. This case, which has not yet been considered in the most general, purely kinetic approach that accounts for dust grain charging, is of primary interest for the description of dust ion-acoustic perturbations because the main contribution to their spectrum comes, as a rule, from modes with frequencies $\omega \gg \nu_q$. As will be shown below, the results of analyzing this case by the kinetic approach that incorporates dust grain charging differ *qualitatively* from the results obtained by Rosenberg [13] in the approach in which dust grain charging was not taken into account.

The electron, ion, and dust densities are assumed to satisfy the plasma quasineutrality condition

$$n_{e0} + n_{d0}Z_{d0} = n_{i0}. \quad (38)$$

In the approximation adopted here, the dielectric function of a dusty plasma has the form

$$\varepsilon_{\mathbf{k},\omega} = 1 + \frac{1}{|\mathbf{k}|^2\lambda_{De}^2}(1 + \xi_{dw}(\sqrt{\pi z_0}e^{-z_0} + \pi(z_0 - 1/2)(1 + \mathrm{erf}(\sqrt{z_0})))) - \frac{\omega_{pi}^2}{\omega^2} + i\left(\sqrt{\frac{\pi}{2}}\frac{\omega_{pe}^2\omega}{|\mathbf{k}|^3 v_{Te}^3}\left(1 + \frac{4\xi_{dw}}{\pi}(z_0\Gamma(0, z_0) - e^{-z_0})\right) + \frac{4\xi_{dw}e^{-z_0}}{\sqrt{2\pi}\lambda_{De}^2|\mathbf{k}|^2\xi_e}\right), \quad (39)$$

where $\lambda_{De} = v_{Te}/\omega_{pe}$ is the electron Debye radius, $\mathrm{erf}(x)$ is the error function, and $\Gamma(\alpha, z_0) = \int_{z_0}^{\infty} x^{\alpha-1}\exp(-x)dx$.

Note that expression (39) contains terms proportional to ξ_{dw}. It is these terms that account for the presence of dust grains with variable charges. The largest of them is the last term with the small quantity ξ_e in the denominator and it is the only one among the terms proportional to ξ_{dw} that will be considered hereafter. This term can be interpreted as a correction that takes into account the presence of dust grains with *variable charge* in the conventional expression for the plasma dielectric function, which was used, e.g., in [13], where the dust can only be accounted for in terms of the dependence of the ion plasma frequency and electron Debye radius on the ion density and electron density, respectively. In [13], no account was taken of the effect of the variable dust charge on the plasma dielectric function and, accordingly, the terms proportional to ξ_{dw} were not taken into consideration.

The dispersion relation $\varepsilon_{\mathbf{k},\omega} = 0$ has a solution in the form $\omega_{\mathbf{k}} = \omega_{\mathbf{k}}^s + i\gamma_{\mathbf{k}}^L$, which yields the well-known dispersion relation for ion-acoustic waves,

$$\omega_{\mathbf{k}}^s \approx \frac{|\mathbf{k}|c_s\sqrt{n_i/n_e}}{\sqrt{1 + |\mathbf{k}|^2\lambda_{De}^2}}, \quad (40)$$

and the new expression for the kinetic damping rate,

$$\gamma_{\mathbf{k}}^L \approx -\sqrt{\frac{\pi}{8}\frac{m_e}{m_i}\frac{n_i}{n_e}}\frac{\omega_{\mathbf{k}}^s}{(1 + |\mathbf{k}|^2\lambda_{De}^2)^{3/2}} - \nu_q\sqrt{\frac{\pi}{2}}\frac{Z_{d0}d}{z_0}\frac{(t + z_0)}{(1 + t + z_0)(1 + |\mathbf{k}|^2\lambda_{De}^2)}, \quad (41)$$

where $c_s = \sqrt{T_e/m_i}$ is the ion-acoustic speed and $d = n_{d0}/n_{e0}$.

The first term on the right-hand side of relationship (41) describes ordinary Landau damping, while the second describes damping due to the interaction of electrons and ions with dust grains. The rates of these two damping processes are both referred to as the kinetic damping rate. The introduction of the common term is justified because, in a dusty plasma, these processes are inseparable. This is most strikingly exemplified in [11], in which the damping of dust ion-acoustic waves was considered in the case $\omega \ll \nu_q$, opposite to the case treated here. It follows from this example that, even when the resonant denominators describing the damping in the dielectric response functions of the electrons and ions correspond to conventional Landau poles, a new kind of collisionless damping arises that differs from ordinary Landau damping and is associated with the dust grain charging processes.

Relationships (40) and (41) constitute a solution to the initial-value problem, specifically, they determine the complex solutions $\omega_{\mathbf{k}}$ to the dispersion relation at real $\mathbf{k}$ values. In order to describe experiments, however, it is often of interest to know the solution to a boundary-value problem in which the frequency ω is real and the complex values of $\mathbf{k}$ are determined from the dispersion relation $\varepsilon_{\mathbf{k},\omega} = 0$.

For weakly damped waves, the real part of the wave vector $\mathbf{k}$ is determined from the equation $\mathrm{Re}(\varepsilon_{\mathbf{k},\omega}) = 0$ and has the form

$$\mathrm{Re}(\mathbf{k}) = \frac{\omega}{\lambda_{Di}}\sqrt{\frac{t}{(\omega_{pi}^2 - \omega^2)(1 + Z_{d0}d)}}, \quad (42)$$

where $\lambda_{Di} = v_{Ti}/\omega_{pi}$ is the ion Debye radius. The imaginary part of the wave vector is given by the expression [18]

$$\mathrm{Im}(\mathbf{k}) = -\frac{\mathrm{Im}(\varepsilon_{\mathbf{k},\omega})}{\partial\,\mathrm{Re}(\varepsilon_{\mathbf{k},\omega})/\partial\mathbf{k}}\bigg|_{\mathbf{k} = \mathbf{k}(\omega)}. \quad (43)$$

In the case at hand, this expression reduces to

$$\mathrm{Im}(\mathbf{k}) = -\sqrt{\frac{\pi}{8}}\frac{\omega}{v_{Te}} - \sqrt{\frac{2}{\pi}}\xi_{dw}e^{-z_0}\frac{\omega v_{Te}t}{(\omega_{pi}^2 - \omega^2)(1 + Z_{d0}d)\lambda_{Di}^2}, \quad (44)$$

which can also be rewritten as

$$\mathrm{Im}(\mathbf{k}) = -\sqrt{\frac{\pi}{8}}\frac{\omega}{v_{Te}} - \frac{\nu_q}{2\lambda_{De}\sqrt{\omega_{pi}^2 - \omega^2}}\frac{Z_{d0}d}{z_0}\frac{(t + z_0)}{(1 + t + z_0)}. \quad (45)$$

In [13], only the first term (which does not contain ν_q) in kinetic damping rate (41) was taken into account. However, in some situations typical of present-day experiments with complex plasmas, the second term (which contains ν_q) predominates over the first. In fact,

for $Z_{d0}d \sim 1$, the second term (with ν_q) in relationship (41) is larger than the first under the conditions

$$1 \ll \frac{\omega_{\mathbf{k}}^s}{\nu_q} \ll \sqrt{\frac{m_i}{m_e}}. \quad (46)$$

The conditions under which the second term (with ν_q) in expression (45) predominates over the first are also given by inequalities (46) but with $\omega_{\mathbf{k}}^s$ replaced by ω. Conditions (46) are easily satisfied for multimode ion-acoustic perturbations, because experiments are usually carried out with fairly heavy ions (Cs^+, Ar^+, etc.). We thus arrive at the conclusion that dust grain charging processes can substantially modify the rate of kinetic damping of dust ion-acoustic perturbations; moreover, in many situations, it is these charging processes that dominate the kinetic damping mechanism.

3. HYDRODYNAMIC MODELS OF A COMPLEX PLASMA

Since nonlinear processes occurring in a complex plasma are very difficult to describe by solving kinetic equations, they are often described in terms of hydrodynamic models. For shock-wave structures and solitons, a reasonably good agreement between theory and experiment is provided by the so-called ionization source model developed in [5, 19], or by its modified version [6, 7]. The necessity of modifying the model arises from the fact that, under different experimental conditions, the medium is ionized by different mechanisms, described by different ionization source terms.

The evolutionary equations of the ionization source model are obtained from kinetic equations (5) for plasma particles. An important point here is the derivation of the rates of dissipative processes [12, 20].

Let us consider the modified version of the ionization source model that was developed in [6] and made it possible to describe all the main features of laboratory experiments with dust ion-acoustic shock waves in a double plasma device [8] modified to enable the dust to be present in the plasma, and in a Q-machine device [9]. In the modified version of the model, the evolutionary equations for the ions in plane geometry have the form

$$\partial_t n_i + \partial_x(n_i v_i) = -\nu_{\text{ch}} n_i + S_i, \quad (47)$$

$$\partial_t(n_i v_i) + \partial_x(n_i v_i^2) = -\frac{e n_i}{m_i}\partial_x\varphi - \frac{T_i}{m_i}\partial_x n_i - \tilde{\nu} n_{0i} v_i. \quad (48)$$

Here, v_i is the directed ion velocity; S_i is the ionization source term; φ is the electrostatic potential; ν_{ch} is the rate of absorption of the ions by dust grains,

$$\nu_{\text{ch}} = \nu_q \frac{Z_{d0}d}{1 + Z_{d0}d}\frac{(t + z_0)}{z_0(1 + t + z_0)}; \quad (49)$$

$\tilde{\nu}$ is the rate at which the ions lose their momentum as a result of their absorption on the grain surfaces and their Coulomb collisions with dust grains; and

$$\tilde{\nu} = \nu_q \frac{Z_{d0}d}{(1 + Z_{d0}d)z_0(1 + t + z_0)} \times \left(z_0 + \frac{4t}{3} + \frac{2z_0^2}{3t}\Lambda\right), \quad (50)$$

where $\Lambda = \ln(\lambda_{Di}/\max\{a, b\})$ is the Coulomb logarithm, $\lambda_{Di} = \omega_{pi}/v_{Ti}$ is the ion Debye radius, and $b = Z_{d0}e^2/T_i$. Note that expressions (49) and (50) are valid in the range $v_i/c_s < 1$.

For the experimental conditions of [8, 9], the ionization source term S_i in the evolutionary equations for the ion density differs from the term that accounts for the conventional electron-impact ionization of neutrals and is traditionally used to describe dusty plasma. In fact, in the experiments of [8], the electron mean free paths were so long that the neutrals were most likely ionized in collisions with the wall. Thus, under the experimental conditions of [8] (the partial pressure of a neutral gas (argon) was $(3–6) \times 10^{-4}$ torr and the electron temperature was $T_e = 0.1$ eV), the electron mean free path with respect to electron–neutral collisions was on the order of 10^4 cm, which was much larger than the length (90 cm) and diameter (40 cm) of the device [21]. In the laboratory experiments of [9], a hot (~2000–2500 K) plate installed in the end region of the device was irradiated with a beam of cesium atoms, so that the cesium ions in the plasma were produced through ionization of cesium atoms at the plate surface. Hence, the ionization source term S_i is independent of the electron density and thus can be assumed to be constant.

In the evolutionary equation for the electron density, plasma electrons are described by the Boltzmann distribution (it is assumed that trapped electrons play an insignificant role):

$$n_e = n_{e0}\exp\left(\frac{e\varphi}{T_e}\right). \quad (51)$$

The model equations also include Poisson's equation for the electrostatic potential,

$$\partial_{xx}^2\varphi = 4\pi e(n_e + Z_d n_d - n_i) \quad (52)$$

and the equation for the variable charge of dust grains,

$$\partial_t q_d = I_e(q_d) + I_i(q_d), \quad (53)$$

where the electron and ion microscopic currents to a grain are obtained from formulas (7) and (1) under the assumption that the ions (moving with a finite directed velocity v_i) and electrons obey Maxwellian distribution functions:

$$I_e \approx -\pi a^2 e\left(\frac{8T_e}{\pi m_e}\right)^{1/2} n_e \exp\left(\frac{e q_d}{a T_e}\right), \quad (54)$$

$$I_i = \sqrt{\frac{\pi}{2}}a^2 \nu_{Ti} e n_i \left[2\exp\left(-\frac{v_i^2}{2v_{Ti}^2}\right) + \sqrt{2\pi}\frac{v_{Ti}}{v_i}\left(1 + \frac{v_i^2}{v_{Ti}^2} - \frac{2eq_d}{am_i v_{Ti}^2}\right)\mathrm{erf}\left(\frac{v_i}{\sqrt{2}v_{Ti}}\right)\right]. \quad (55)$$

We linearize Eqs. (47), (48), and (51)–(55) and carry out a Fourier transformation to obtain the following dispersion relation for ion-acoustic waves:

$$-|\mathbf{k}|^2\lambda_{De}^2 = 1 + \frac{(1 + Z_{d0}d)|\mathbf{k}|^2 c_s^2}{(i\omega - \nu_{ch})(i\omega - \tilde{\nu}) + |\mathbf{k}|^2 v_{Ti}^2} + \left[1 + \frac{|\mathbf{k}|^2 c_s^2}{(i\omega - \nu_{ch})(i\omega - \tilde{\nu}) + |\mathbf{k}|^2 v_{Ti}^2}\right] \times \frac{t + z_0}{t}(1 + Z_{d0}d)\frac{4\sqrt{\pi/2}n_d a^2 \nu_{Ti}}{\nu_q - i\omega}. \quad (56)$$

This dispersion relation has a solution in the form $\omega_\mathbf{k} = \omega_R + i\gamma_\mathbf{k}$, which, under the third of inequalities (37) and under the conditions $\{\nu_{ch}, \tilde{\nu}, \nu_q\} \ll \omega_\mathbf{k}^s$, gives the dispersion relation $\omega_R = \omega_\mathbf{k}^s$ for ion-acoustic waves [see dispersion relation (40)] and also yields the following expression for the damping rate:

$$\gamma_\mathbf{k} \approx -\Gamma \equiv -\frac{\nu_{ch} + \tilde{\nu}}{2}. \quad (57)$$

Other modified versions of the ionization source model that make use of the constant ionization source term S_i lead to analogous results. Among these is the modified model that was utilized in [7, 20] to describe solitons with trapped electrons. In this way, switching to the electron distribution function proposed by Gurevich [22] produces the same final result.

Under conditions of a complex plasma in typical experiments with glow discharges or with high-frequency discharges (see, e.g., [23, 24]), the main mechanism for ionizing neutrals is, as a rule, conventional electron-impact ionization. In this case, the ionization source term S_i is proportional to the electron density [25], $S_i = \nu_i n_e$, where ν_i is the gas ionization rate, which increases exponentially with the electron temperature T_e and depends also on the neutral gas parameters. The equations of the relevant modified version of the ionization source model are presented, e.g., in [5, 19]. They differ from Eqs. (47) and (48) in two respects: first, in Eqs. (47) and (48), the ionization source term is represented in another form; second, in [5, 19], the effect of the gas-kinetic ion pressure on the evolution of the system was not taken into consideration. An analysis of the dispersion properties of ion-acoustic waves on the basis of the set of equations presented in [5, 19] yields results that differ from those following from formulas (56) and (57). Thus, the dispersion relation has the form

$$-|\mathbf{k}|^2\lambda_{De}^2 = \left(1 - \frac{1}{\nu_{ch} - i\omega}\left[\nu_i + \frac{(1 + Z_{d0}d)|\mathbf{k}|^2 c_s^2}{i\omega - \tilde{\nu}}\right]\right) \times \frac{t + z_0}{t}\left(1 + \frac{4\sqrt{\pi/2}n_d a^2 \nu_{Ti}}{\nu_q - i\omega}\right), \quad (58)$$

and the imaginary part of the frequency is equal to

$$\gamma_\mathbf{k} \approx -\Gamma + \frac{\nu_i}{2(1 + |\mathbf{k}|^2\lambda_{De}^2)}. \quad (59)$$

The second term on the right-hand side of expression (59) is positive. The situation in which the second term becomes larger than the first corresponds to the development of the ionization instability. Nevertheless, as in expression (57), the dissipation in expression (59) is also characterized by the term Γ.

From expression for Γ, it is clear that, in terms of the ionization source model, the dissipation in a complex plasma is governed by the processes of the absorption of ions by dust grains and also by Coulomb collisions between ions and dust grains. All these processes are closely related to the mechanisms by which the grains are charged. In fact, on the one hand, we have $\Gamma \propto \nu_q$; and, on the other, we see that the absorbed ions participate directly in dust grain charging. However, it is not the only mechanism for anomalous dissipation peculiar to a complex plasma. An important role can also be played by the kinetic damping mechanism—the damping described at the kinetic level, including the Landau damping—which is not taken into account in the ionization source model. In the next section, we will analyze the ratio between the kinetic damping rate and Γ. Then, based on the results of this analysis, we will discuss the role of the kinetic damping mechanism and investigate the conditions under which it operates as the main mechanism for generating nonlinear waves in a complex plasma.

Along with the ionization source model for describing nonlinear dust ion-acoustic structures, a hydrodynamic model [8, 26] was developed that leads to the Korteweg–de Vries–Burgers (KdVB) equation with the dissipative viscosity coefficient proportional to the ion–grain collision rate. Note, however, that, in a classical approach to describing dusty plasmas in terms of Eqs. (1)–(7), it is impossible to derive a general hydrodynamic equation that would describe the evolution of the momentum of the ions and would contain the viscosity term in conventional hydrodynamic form (it is precisely this general equation that served as the basis for deriving the KdVB equation used in [8, 26]).

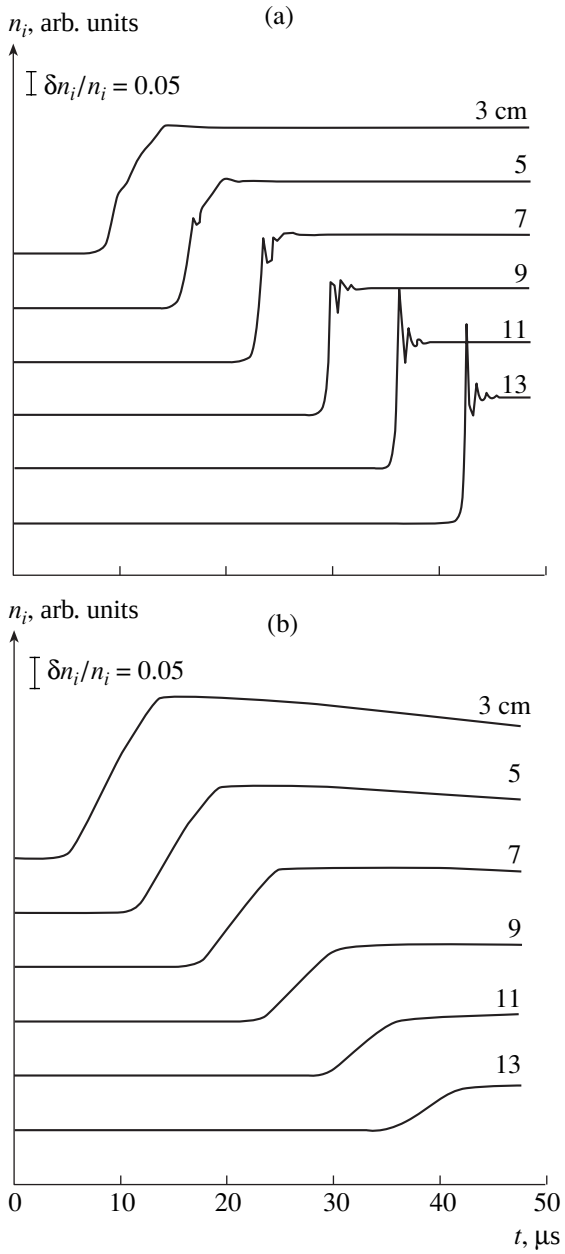

Fig. 1. Time evolutions of the ion density n_i at different distances from the grid for two different values of the dust density: n_{d0} = (a) 0 and (b) 1.46×10^4 cm^{-3}. The remaining dusty plasma parameters are $T_e = T_i = 1.5$ eV, $n_{i0} = 2.3 \times 10^8$ cm^{-3}, and $a = 4.4$ μm. As in the experiment of [8], the oscillations in the shock wave profile due to the separation of charges (electrons and ions) are suppressed by the dust.

4. INTERPRETATION OF EXPERIMENTS IN TERMS OF THE IONIZATION SOURCE MODEL

As was noted above, the ionization source model [6] makes it possible to describe all the main results of laboratory experiments that have been carried out so far on the generation of dust ion-acoustic shock waves [8, 9]. We now describe these experiments and present the main conclusions derived from them.

4.1. Experiment at the Institute of Space and Astronautical Science (Japan)

This experiment [8] revealed the following main feature of ion-acoustic waves in a dusty plasma:

In the absence of dust, there are oscillations in the vicinity of the front of shock waves due to the separation of charges (electrons and ions). The presence of dust suppresses these oscillations.

In the experiments of [8], the parameters of the dusty plasma were as follows: $T_e \approx 1$–1.5 eV, $T_i < 0.1$ eV, $n_{e0} \sim 10^8$–10^9 cm^{-3}, and $a \approx 4.4$ μm. The dust density was varied from 0 to about 10^5 cm^{-3}. Ion-acoustic shock waves were excited by applying a triangular voltage pulse with a peak amplitude of 2.0 V and a duration of ≈10 μs to the driver anode.

In [6], the calculations were performed for different dust densities and for $T_e = T_i = 1.5$ eV, $n_{i0} = 2.3 \times 10^8$ cm^{-3} (the ion background density was the same for all cases), and $a = 4.4$ μm. The width of the perturbation ($\Delta x \approx 20$ cm) and its shape were determined self-consistently, in accordance with the method for exciting a shock wave. It should be noted that Nakamura and Bailung [21] compared the theoretical results on the dependence of the potential difference between a grain and a plasma on the plasma parameters with the measurement data obtained with the same device under essentially the same conditions as those prevailing in the experiment of [8]. They found that, although the ion temperature was significantly lower than the electron temperature ($T_i \ll T_e$), the experimental results were best fitted by the theoretical curve calculated for $T_i = T_e$. They attributed this circumstance to the possible ion acceleration to energies comparable to the electron energy. That is why, in our calculations, the values of T_i and T_e were taken to be the same.

In Fig. 1 (which is analogous to Fig. 3 from [8]), we illustrate the time evolution of the ion density at different distances from the grid. The evolutions were calculated for (a) $n_{d0} = 0$ (the electron density being $n_{e0} = 2.3 \times 10^8$ cm^{-3}) and (b) $n_{d0} = 1.46 \times 10^4$ cm^{-3} (the electron density being $n_{e0} = 4.6 \times 10^8$ cm^{-3}). We can see that, in both theory and experiment, oscillations in the shock-wave profile due to the separation of charges (electrons and ions) are suppressed by the dust. The theoretically calculated duration of the shock front is about 5 μs, which corresponds to the measurement data.

According to [27], Fig. 1a, which was obtained in terms of the ionization source model, correctly reflects qualitatively the experimentally observed effect that cannot be captured, e.g., by a model based on the KdVB equation [8]—the excitation of oscillations in

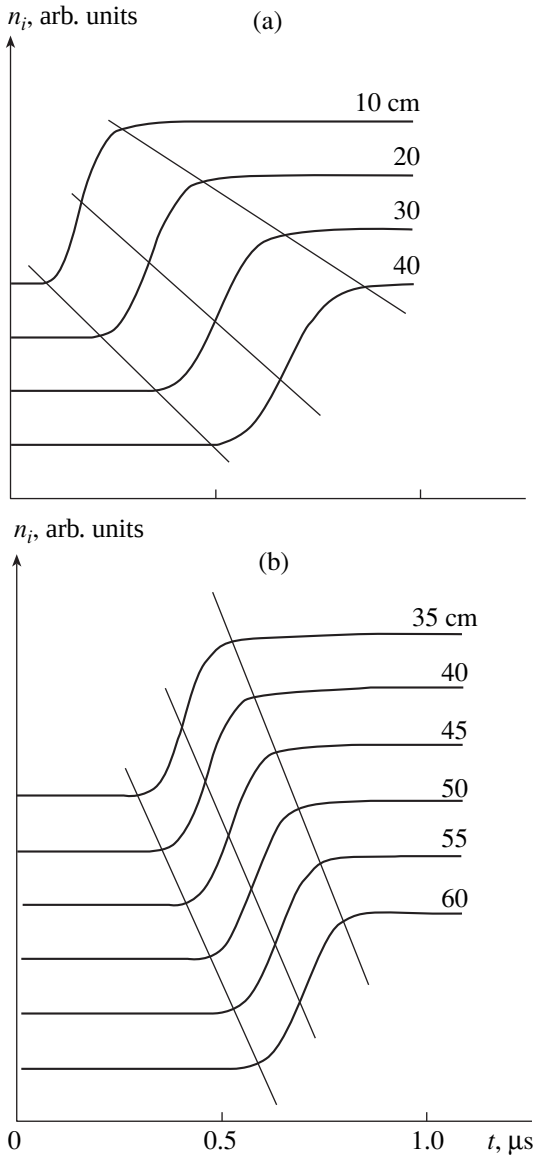

Fig. 2. Time evolutions of the ion density n_i (heavy curves) at different distances from the grid for ϵZ_{d0} = (a) 0 and (b) 0.75. The remaining parameters of the dusty plasma and of the perturbation are as follows: $T_e = T_i = 0.2$ eV, $n_{i0} = 1.024 \times 10^7$ cm^{-3}, $a = 0.1$ μm, $\Delta x = 25$ cm, and $\Delta n_i/n_{i0} = 2$. The light lines show the widening of the wave front (at $\epsilon Z_{d0} = 0$) and its steepening (at $\epsilon Z_{d0} = 0.75$), which agrees with the experimental data of [9].

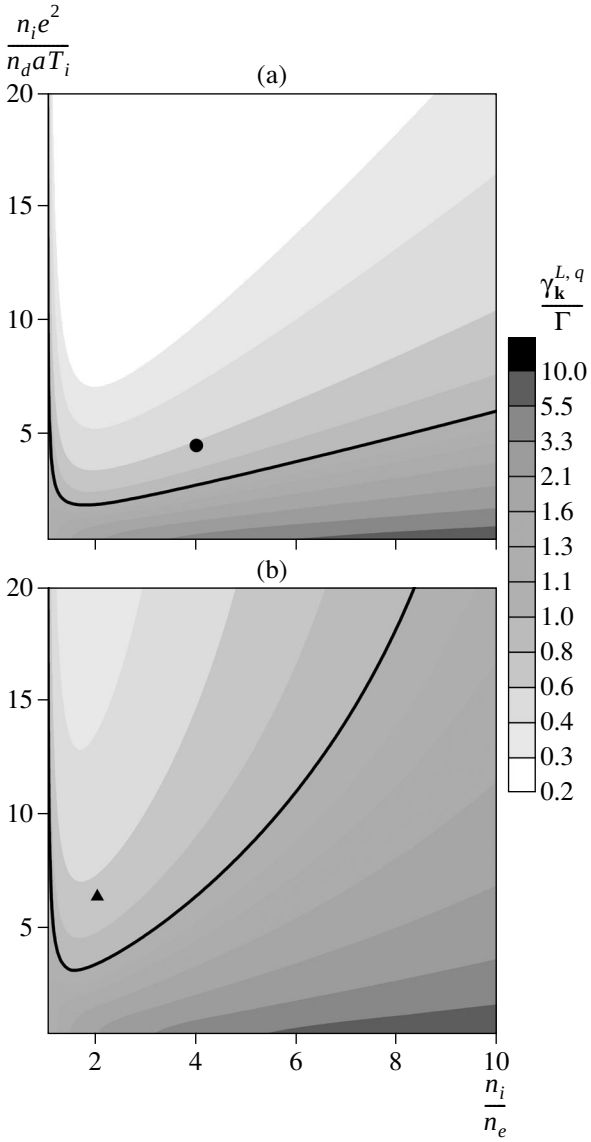

Fig. 3. Relief of the ratio $\gamma_{\mathbf{k}}^{L,q}/\Gamma$ on the plane ($n_i e^2/n_d a T_i$, n_i/n_e) for the plasma parameters (a) in the experiment of [9] ($T_e = T_i = 0.2$ eV, $n_i = 1.024 \times 10^7$ cm^{-3}, Cs^+ ions, $a = 0.1$ μm) and (b) in the experiments of [8, 10] ($T_e = 1.5$ eV, $T_i < 0.1$ eV, $n_i = 2.3 \times 10^8$ cm^{-3}, Ar^+ ions, $a = 4.4$ μm). The closed circle in plot (a) corresponds to $\epsilon Z_{d0} = 0.75$ and to the plasma parameters in the experiment of [9]. The closed triangle in plot (b) corresponds to $\epsilon Z_{d0} = 0.5$ and to the plasma parameters in the experiments of [8, 10]. The heavy curves correspond to $\gamma_{\mathbf{k}}^{L,q} = \Gamma$.

the shock-wave profile due to charge separation. Figure 1a shows the onset of a perturbation in the shock front at a distance of 3 cm from the grid; at longer distances from the grid, this perturbation is seen to develop into oscillations in the shock front that are attributed to the separation of charges. This picture of the excitation of oscillations agrees completely with the experimental observations.

Hence, the ionization source model is capable of describing the main features of the experiment in [8].

4.2. Experiment at the University of Iowa

The main results of the experiment in a Q-machine device [9] are as follows:

(i) Dust ion-acoustic shock waves form at sufficiently high dust densities (under the experimental conditions of [9], at dust densities such that $\epsilon Z_{d0} \equiv$

$n_{d0}Z_{d0}/n_{i0} \geq 0.75$). In [9], the conclusion regarding the formation of a shock wave was drawn from the fact that the perturbation front steepens as time elapses. At sufficiently low dust densities, the perturbation front does not steepen but widens instead.

(ii) When the shock wave structure has formed, the shock front width $\Delta\xi$ corresponds to the following theoretical estimate, which is based on the model developed in [1]:

$$\Delta\xi \sim Mc_s/\nu_q, \tag{60}$$

where Mc_s is the speed of the shock wave structure and M is the Mach number.

(iii) The velocity of the dust ion-acoustic waves increases considerably with increasing ϵZ_{d0}.

The plasma parameters in the experiment of [9] were as follows: $T_e \approx T_i \approx 0.2$ eV, $n_{i0} \sim 10^6$–10^7 cm^{-3}, and $a \sim 0.1$–1 μm. The parameter ϵZ_{d0} was varied from 0 to 0.95. The goal of the experiment was to study the evolution of a rectangular perturbation that was initiated in the initial ion density profile by a grid held at an electrostatic potential of about –6 V with respect to the potential of the hot plate. The width of the initial perturbation was about 25 cm [28].

In [6], the calculations were carried out based on the ionization source model for different values of the parameter ϵZ_{d0} and for the following values of the plasma parameters: the electron and ion temperatures were equal to one another, $T_e = T_i = 0.2$ eV; the background ion density $n_{i0} = 1.024 \times 10^7$ cm^{-3} was the same for all cases; the grain radius was $a = 0.1$ μm; the width of the rectangular initial perturbation was $\Delta x = 25$ cm; and the excess initial perturbed ion density above the background ion density in the remaining unperturbed plasma of the device was $\Delta n_i/n_{i0} = 2$ (see Fig. 2 in [9]).

The ionization source model made it possible to explain [6] all of the above three features of the experiment carried out in [9]. In this section, we present only the profiles of nonlinear perturbations in a plasma with and without dust. In Fig. 2 (which is analogous to Fig. 2 from [9]), the heavy curves show the time evolutions of the ion density at different distances from the grid for ϵZ_{d0} = (a) 0 and (b) 0.75. The light lines show the widening of the wave front (at $\epsilon Z_{d0} = 0$) and its steepening (at $\epsilon Z_{d0} = 0.75$), which agrees with the experimental data of [9].

5. THE EFFECT OF KINETIC DAMPING

Here, we apply the results of the above analysis to investigate the effect of the damping described at the kinetic level (including Landau damping) and to understand its relative role versus other dissipative processes in different experiments with complex plasmas. Historically, the most typical dusty plasma experiments were carried out with glow discharges or with RF discharges (see, e.g., [23, 24]), whereas nonlinear dust ion-acoustic structures were observed in a double plasma device (modified to enable the dust to be present in the plasma) [8, 10] and in a Q-machine device [9]. This is why it is of interest to examine the relative roles of the damping described at the kinetic level and of the dissipative processes described in the hydrodynamic approach for the above four kinds of experiments.

It should be noted that, although the theoretical ionization source model, which does not take into account Landau damping, is capable of interpreting all the main experimental results on dust ion-acoustic shock waves, the fact that, in the experiment at the University of Iowa, such waves were observed to be excited at sufficiently high dust densities was explained in terms of the dissipation associated with Landau damping [9]. Moreover, the kinetic damping rate was described without allowance for the processes of dust grain charging [13]. Following the logic of [9], the presence of negatively charged dust weakens the Landau damping because the phase velocity of linear dust ion-acoustic waves increases with the dust density (or, more precisely, with the parameter $\epsilon Z_d \equiv Z_d n_d/n_i$).

However, in terms of the description developed by Rosenberg [13], the Landau damping rate increases with the dust density at a faster rate than the phase velocity v_{ph} of the waves. In fact, $v_{\text{ph}} \equiv \omega_{\mathbf{k}}^s/|\mathbf{k}| \propto \sqrt{n_i/n_e} = 1/\sqrt{1-\epsilon Z_d}$ (see dispersion relation (40)), while, in Rosenberg's description [13], the Landau damping rate has the form

$$\gamma_{\mathbf{k}}^{L,R} \approx -\sqrt{\frac{\pi}{8}\frac{m_e}{m_i}\frac{n_i}{n_e}}\frac{\omega_{\mathbf{k}}^s}{(1+|\mathbf{k}|^2\lambda_{De}^2)^{3/2}}, \tag{61}$$

which gives $\gamma_{\mathbf{k}}^{L,R} \propto n_i/n_e = 1/(1-\epsilon Z_d)$. Consequently, an increase in the parameter ϵZ_d implies that Landau damping plays an increasingly important role; but this result contradicts the above conclusion in [9]. If the Landau damping rate begins to exceed in absolute value the frequencies ν_{ch}, ν_q, and $\tilde{\nu}$, then either the shock waves cannot exist at all or they will be different in nature from the shock waves associated with anomalous dissipation (it is most likely that they will occur as a sort of collisionless shock waves).

Note that the above conclusions were reached on the basis of the portion of the kinetic damping rate that is given by formula (61), but they can actually be somewhat refined by using the general formula (41) for the kinetic damping rate. First, the characteristic width $\Delta\xi$ of the front of the shock wave associated with anomalous dissipation is given by expression (60). This implies that the characteristic wave vector corresponding to the shock-wave profile has the form $|\mathbf{k}| \sim 2\pi/\Delta\xi \sim \nu_q/Mc_s$. Substituting this characteristic wave vector into dispersion relation (40) and kinetic damping rate (41)

enables us to compare the first and second terms in the latter formula. The result is that the second term

$$\gamma_{\mathbf{k}}^{L,q} = -\nu_q\sqrt{\frac{\pi}{2}}\frac{Z_{d0}d}{z_0}\frac{(t+z_0)}{(1+t+z_0)(1+|\mathbf{k}|^2\lambda_{De}^2)} \quad (62)$$

is approximately $\sqrt{m_i/m_e}$ times larger than the first term $\gamma_{\mathbf{k}}^{L,R}$.

The characteristic value of $|\mathbf{k}|$ in the wave spectrum corresponding to a particular shock-wave profile can be estimated by taking the Fourier transform of the profile. Thus, for the shock-wave profile that is shown Fig. 2b and is calculated for a distance of 60 cm from the grid, we obtain $|\mathbf{k}| \approx 0.12$ cm^{-1}. For this $|\mathbf{k}|$ value, the term $\gamma_{\mathbf{k}}^{L,q}$ is about one order of magnitude larger than the term $\gamma_{\mathbf{k}}^{L,R}$ in the kinetic damping rate.

Since the term $\gamma_{\mathbf{k}}^{L,q}$ in the kinetic damping rate accounts for dust grain charging, the shock waves under consideration are dominated by anomalous dissipation. The question then arises of whether this situation can be described in terms of the ionization source model. The above hydrodynamic model can be applied if the term Γ in expression (57) is larger than $\gamma_{\mathbf{k}}^{L,q}$. Hence, it is of interest to determine the ranges of plasma parameters in which Γ exceeds $\gamma_{\mathbf{k}}^{L,q}$.

Figures 3 and 4 present the relief of the ratio $\gamma_{\mathbf{k}}^{L,q}/\Gamma$ on the plane (n_ie^2/n_daT_i, n_i/n_e) for the parameters of complex plasmas in experiments in a Q-machine device, a double plasma device, and devices based on glow discharges and high-frequency discharges. Figure 3a corresponds to the experimental conditions of [9] ($T_e = T_i = 0.2$ eV, $n_i = 1.024 \times 10^7$ cm^{-3}, Cs^+ ions, $a = 0.1$ μm). The closed circle in Fig. 3a corresponds to $\epsilon Z_{d0} = 0.75$. Figure 3b was drawn for the experimental conditions of [8, 10] ($T_e = 1.5$ eV, $T_i < 0.1$ eV, $n_i = 2.3 \times 10^8$ cm^{-3}, Ar^+ ions, $a = 4.4$ μm). The closed triangle in Fig. 3b corresponds to $\epsilon Z_{d0} = 0.5$. It can be seen that the experimental parameters of [8–10] satisfy the inequality $\gamma_{\mathbf{k}}^{L,q}/\Gamma < 1$. This indicates that the ionization source model is applicable to nonlinear dust ion-acoustic structures in a double plasma device and a Q-machine device. Figure 4a refers to the plasma parameters of experiments carried out on board the International Space Station [24] ($T_e \approx 1$ eV, $T_i \approx 0.03$ eV, $n_i \approx 2 \times 10^9$ cm^{-3}, Ar^+ ions, $a = 3.4$ μm). Figure 4b was obtained for the plasma parameters in experiments with glow discharges [23] ($T_e \approx 3$ eV, $T_i \approx 0.03$ eV, $n_e \approx 10^9$ cm^{-3}, Ne^+ ions, $a \approx 4$ μm). We can see that, for $n_i/n_e = 1/(1-\epsilon Z_d) > 3$ in the experiments of [24] and for $n_i/n_e = 1/(1-\epsilon Z_d) > 1$ in the experiments of [23], the ratio $\gamma_{\mathbf{k}}^{L,q}/\Gamma$ is always larger than unity. This means that, over fairly wide ranges of the dust grain parameters, dust ion-acoustic structures in typical experiments carried out with complex plasmas on devices based on glow and RF discharges should be described in terms of kinetic theory. Thus, the condition $\gamma_{\mathbf{k}}^{L,q}/\Gamma > 1$ serves as a criterion for determining whether or not the kinetic

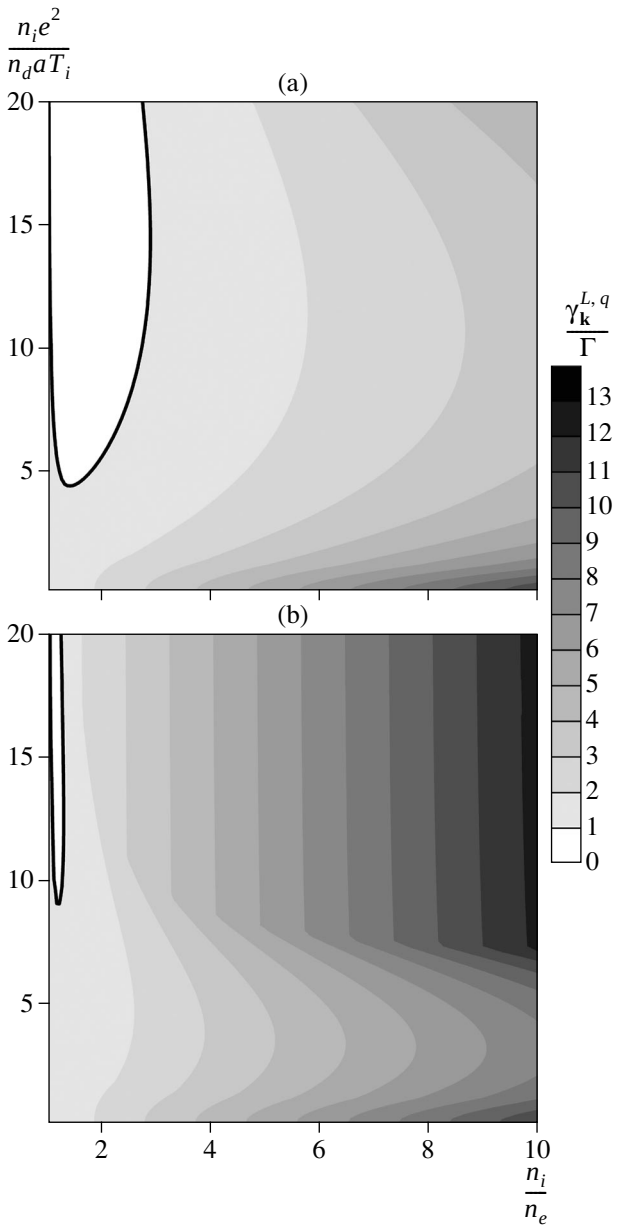

Fig. 4. Relief of the ratio $\gamma_{\mathbf{k}}^{L,q}/\Gamma$ on the plane (n_ie^2/n_daT_i, n_i/n_e) for the plasma parameters (a) in the experiment of [24] ($T_e \approx 1$ eV, $T_i \approx 0.03$ eV, $n_i \approx 2 \times 10^9$ cm^{-3}, Ar^+ ions, $a = 3.4$ μm) and (b) in the experiment of [23] ($T_e \approx 3$ eV, $T_i \approx 0.03$ eV, $n_e \approx 10^9$ cm^{-3}, Ne^+ ions, $a \approx 4$ μm). The heavy curves correspond to $\gamma_{\mathbf{k}}^{L,q} = \Gamma$.

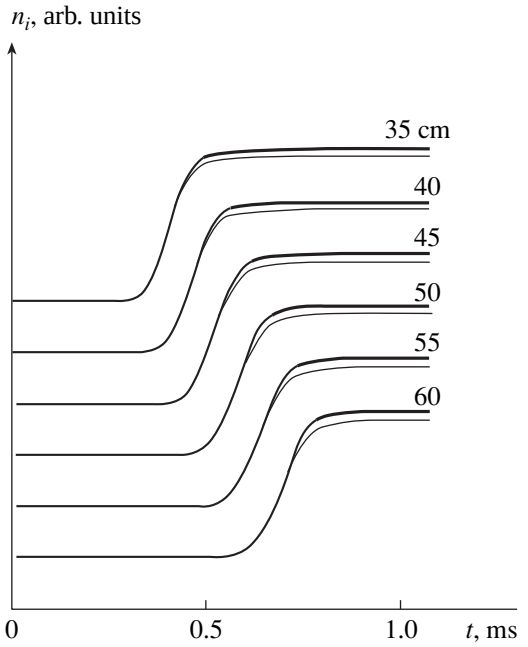

Fig. 5. Time evolutions of the ion density at different distances from the grid for $\epsilon Z_{d0} = 0.75$. The parameters of the dusty plasma and of the perturbation correspond to those in the experiment of [9]: $T_e = T_i = 0.2$ eV, $n_{i0} = 1.024 \times 10^7$ cm^{-3}, $a = 0.1$ μm, $\Delta x = 25$ cm, and $\Delta n_i/n_{i0} = 2$. The heavy curves show the time evolutions of the ion density calculated by using the ionization source model. The light curves illustrate the deviations from these time evolutions due to kinetic damping (including Landau damping).

approach is applicable to the nonlinear dust ion-acoustic structures observed in experiments.

It should be noted that, in applying the ionization source model to explain the fact that, in the experiment in [9], the dust ion-acoustic shock waves formed at sufficiently high dust densities, a fairly important role was played by the boundary condition that was imposed on the hot plate in the end region of the Q-machine device (this boundary condition is analogous to the relevant boundary condition in the surface evaporation problem [29]). A cesium atom striking the hot plate becomes ionized. The newly produced cesium ion flies away from the plate at a certain directed velocity. Hence, we can expect that, in the immediate vicinity of the plate, an ion flux will be generated whose intensity and density are strongly sensitive to the plate temperature. The boundary condition in question, which reflects the fact that a cesium vapor plasma is created through surface ionization, was obtained under the following assumptions:

(i) at the plate surface, not only are the atoms ionized, but the inverse process also takes place—the surface recombination of the ions that strike the plate;

(ii) all the ions striking the plate recombine;

(iii) at the initial instant (just before the perturbation starts evolving), the ionization and recombination processes are in dynamic equilibrium (i.e., the ion gas temperature is equal to the plate temperature and the intensity of the flux of the ions that strike the plate and recombine on it is the same as the intensity of the flux of the ions that fly away from the plate surface); and

(iv) the ions flying away from the plate obey a Maxwellian distribution function with a temperature T_i equal to the plate temperature, the directed ion velocity is zero, and the ion density is equal to the initial density of the ion gas.

During the evolution of the initial perturbation, the ions in the vicinity of the plate acquire a nonzero directed velocity v_i, so that their density n_i and their temperature T_i both change. These three parameters of the ions are calculated from the conservation conditions for the ion flux from the plate surface and the ion momentum flux. As at the initial instant, the ions are assumed to obey a Maxwellian distribution function that now corresponds to a nonzero directed ion velocity and an ion density different from the initial ion density near the plate surface.

This model of the ionization process implies that, within the volume of the Q-machine device, the ion temperature T_i is at least two times lower than the electron temperature T_e, which is equal to the plate temperature ($T_i \approx 0.503 T_e$). Possible turbulent electron heating should produce a further increase in the ratio T_e/T_i in the device. In this case, the necessary condition for the existence of dust ion-acoustic perturbations (which follows from the inequality $\omega \gg |\mathbf{k}| v_{Ti}$),

$$\frac{T_e}{T_i} > 1 - \epsilon Z_d \tag{63}$$

is easily satisfied. This indicates that relationship (41) can be used to describe the kinetic damping rate, which turns out to be negligibly slow for the experimental conditions of [9]. The small effect of the kinetic damping on the evolution of the dust ion-acoustic structures in the experiment of [9] is illustrated in Fig. 5, which was obtained for the same parameter values as in Fig. 1b, but with allowance for the change in the rates characterizing dissipative processes in the ionization source model. Hence, in order to reflect the fact that, in the experiment of [9], dust ion-acoustic shock waves formed at sufficiently high dust densities, it is sufficient to correctly incorporate the ionization process into the hydrodynamic ionization source model.

6. CONCLUSIONS

We have presented the main models used in the kinetic and the hydrodynamic description of nonlinear dust ion-acoustic perturbations. The kinetic damping rate, which includes the Landau damping rate, was derived on the basis of a purely kinetic approach to

describing complex plasmas. The expression for the kinetic damping rate is found to contain the conventional terms that account for Landau damping in a plasma consisting of electrons, ions, and dust grain with a constant (unperturbed) charge and the terms that arise from the variable charge of the dust grains. It is shown that, in certain situations, the latter group of terms may play a dominant role. In particular, the condition under which the terms incorporating the variable grain charge into the kinetic damping rate predominate over the remaining terms is easily satisfied for multimode ion-acoustic perturbations in a plasma with fairly heavy ions (Cs^+, Ar^+, etc.), as is often the case in experiments with complex plasmas. These latter terms play a leading role in describing the propagation of dust ion-acoustic shock waves that dissipate their energy in the dust grain charging processes, in the absorption of ions by dust grains, and in the Coulomb collisions between ions and grains. For dust ion-acoustic shock-wave structures and solitons, a fairly good agreement between theory and experiment is provided by the hydrodynamic ionization source model. In this model, the dissipation in a complex plasma is governed by the processes of absorption of ions by dust grains and also by Coulomb collisions between ions and grains. All these processes are closely related to the mechanisms by which the grains are charged. The ionization source model is applicable to the nonlinear dust ion-acoustic structures in a double plasma device and Q-machine device, in which case the dissipation due to kinetic damping (including Landau damping) turns out to be negligibly low. However, in order to provide an adequate description of experimental situations, it is necessary to correctly take into account the ionization processes in the plasma. In typical experiments with complex plasmas in devices based on glow and RF discharges, the effect of kinetic damping on the generation and propagation of dust ion-acoustic structures is significant over fairly wide ranges of the dust grain parameters; it therefore becomes necessary to apply the kinetic approach. We have derived a criterion for determining whether or not the kinetic approach is applicable to nonlinear dust ion-acoustic structures observed in experiments.

The nonlinear dust ion-acoustic structures described in this paper may have important applications in the description of natural phenomena (such as those occurring in the interaction of the solar wind with dusty cometary comas [30]) and may also find significant technological applications in, e.g., so-called hypersonic aerodynamics. The main difficulties of hypersonic flight in the atmosphere are associated with the generation of shock waves; this leads to heavy mechanical and thermal loads on the structural components of an aircraft, considerably increases the resisting forces, and lowers the engine efficiency. Usually, these negative effects are reduced through the optimum streamlining of the aircraft. However, a more promising possibility seems to be changing the properties of the air surrounding the aircraft. In this way, the negative effects may be lessened by modifying the mechanisms for the formation and propagation of shock waves by plasma methods (such as the local heating of air around the aircraft). However, the dust (aerosol) that is produced due to condensation from the surrounding air can, in turn, modify the behavior of the shock-wave structures. This is why an understanding of the dissipation mechanisms in shock-wave structures is of key importance in such situations.

ACKNOWLEDGMENTS

We are grateful to Y. Nakamura and R.L. Merlino for their fruitful discussions of this study. We also thank A.M. Ignatov and A.V. Gordeev for amending the manuscript. This work was supported in part by INTAS (grant no. 01-0391), NATO (grant no. PDD(CP)-PST.CLG 980094), and the Russian Foundation for Basic Research (project nos. 03-02-16664-a and 03-05-64813-a).

REFERENCES

1. S. I. Popel, M. Y. Yu, and V. N. Tsytovich, Phys. Plasmas **3**, 4313 (1996).
2. S. I. Popel, V. N. Tsytovich, and M. Y. Yu, Astrophys. Space Sci. **256**, 107 (1998).
3. S. I. Popel and V. N. Tsytovich, Astrophys. Space Sci. **264**, 219 (1999).
4. S. I. Popel, A. A. Gisko, A. P. Golub', *et al.*, Phys. Plasmas **7**, 2410 (2000).
5. S. I. Popel, A. P. Golub', T. V. Losseva, *et al.*, Phys. Plasmas **8**, 1497 (2001).
6. S. I. Popel, A. P. Golub', and T. V. Loseva, Pis'ma Zh. Éksp. Teor. Fiz. **74**, 396 (2001) [JETP Lett. **74**, 362 (2001)].
7. S. I. Popel, A. P. Golub', T. V. Losseva, *et al.*, *Dusty Plasmas in the New Millennium*, Ed. by R. Bharuthram, M. A. Hellberg, P. K. Shukla, and F. Verheest (AIP, New York, 2002), p. 386.
8. Y. Nakamura, H. Bailung, and P. K. Shukla, Phys. Rev. Lett. **83**, 1602 (1999).
9. Q.-Z. Luo, N. D'Angelo, and R. L. Merlino, Phys. Plasmas **6**, 3455 (1999).
10. Y. Nakamura and A. Sarma, Phys. Plasmas **8**, 3921 (2001).
11. V. N. Tsytovich and O. Havnes, Comments Plasma Phys. Controlled Fusion **15**, 267 (1993).
12. S. Benkadda, P. Gabbai, V. N. Tsytovich, and A. Verga, Phys. Rev. E **53**, 2717 (1996).
13. M. Rosenberg, Planet. Space Sci. **41**, 229 (1993).
14. R. L. Merlino, A. Barkan, C. Thompson, and N. D'Angelo, Phys. Plasmas **5**, 1607 (1998).
15. V. N. Tsytovich and U. de Angelis, Phys. Plasmas **6**, 1093 (1999).
16. P. K. Shukla and V. P. Silin, Phys. Scr. **45**, 508 (1992).
17. V. N. Tsytovich, Usp. Fiz. Nauk **167**, 57 (1997) [Phys. Usp. **40**, 53 (1997)].

18. A. F. Aleksandrov and A. A. Rukhadze, *Lectures on the Electrodynamics of Plasma-Like Media* (Izd. Mosk. Gos. Univ., Moscow, 1999).
19. S. I. Popel, A. P. Golub', T. V. Losseva, and R. Bingham, Pis'ma Zh. Éksp. Teor. Fiz. **73**, 258 (2001) [JETP Lett. **73**, 223 (2001)].
20. S. I. Popel, A. P. Golub', T. V. Losseva, *et al.*, Phys. Rev. E **67**, 056402 (2003).
21. Y. Nakamura and H. Bailung, Rev. Sci. Instrum. **70**, 2345 (1999).
22. E. M. Lifshitz and L. P. Pitaevskiĭ, *Physical Kinetics* (Nauka, Moscow, 1979; Pergamon, Oxford, 1981).
23. A. P. Nefedov, O. F. Petrov, and V. E. Fortov, Usp. Fiz. Nauk **167**, 1215 (1997) [Phys. Usp. **40**, 1163 (1997)].
24. D. Samsonov, G. Morfill, H. Thomas, *et al.*, Phys. Rev. E **67**, 036404 (2003).
25. M. A. Lieberman and A. J. Lichtenberg, *Principles of Plasma Discharges and Material Processing* (Wiley, New York, 1994).
26. P. K. Shukla, Phys. Plasmas **7**, 1044 (2000).
27. Y. Nakamura, private communication (2003).
28. R. L. Merlino, private communication (2001).
29. S. Knake and I. N. Stranskiĭ, Usp. Fiz. Nauk **68**, 261 (1959).
30. S. I. Popel, A. A. Gisko, T. V. Losseva, and S. V. Vladimirov, in *Proceedings of the 30th EPS Conference on Plasma Physics and Controlled Fusion, St. Petersburg, 2003*, p. 4.125.

Translated by G.V. Shepekina

Plasma Physics Reports, Vol. 30, No. 4, 2004, pp. 299–306. Translated from Fizika Plazmy, Vol. 30, No. 4, 2004, pp. 330–338.

WALL PLASMA

Structure of Steady-State Debye Layers in a Low-Density Plasma near a Dielectric Surface

A. I. Morozov* and V. V. Savel'ev**

** Russian Research Centre Kurchatov Institute, pl. Kurchatova 1, Moscow, 123182 Russia*

*** Keldysh Institute of Applied Mathematics, Russian Academy of Sciences, Miusskaya pl. 4, Moscow, 125047 Russia*

Received August 1, 2003; in final form, October 20, 2003

Abstract—Exact steady-state analytic solutions describing kinetic processes in a low-density plasma layer near a dielectric surface are found in a time-dependent one-dimensional model with allowance for secondary electron emission. It is shown that, at low electron temperatures, both the electric potential and electron density monotonically decrease toward the dielectric surface (Debye layer). As the electron temperature increases, an anti-Debye layer first forms, in which the potential monotonically increases toward the wall, and regimes with a nonmonotonic potential profile then arise. © *2004 MAIK "Nauka/Interperiodica".*

1. INTRODUCTION

There is an extensive literature (both general theoretical and special purpose) concerning the structure of Debye layers (DLs), which always emerge in plasma near dielectric surfaces (see, e.g., [1–3]). In these studies, the temperature is generally assumed to be sufficiently low in order for secondary electron emission (SEE) to be of minor importance, and the problem can be reduced to an analysis of the balance between the fluxes of charged particles onto the dielectric wall:

$$(1-\sigma)j_{en}\exp\left(-\frac{eU_D}{kT_e}\right) = j_{in}, \qquad (1)$$

where j_{en} and j_{in} are the electron and ion flux densities far from the Debye layer, σ is the SEE coefficient, and $U_D > 0$ is the Debye potential jump. In some cases, the DL's properties determine the plasma behavior as a whole, which corresponds to a much more intricate situation than that described by Eq. (1). In particular, this concerns the processes occurring in the plasma of stationary plasma thrusters (SPTs) [1, 4, 5], where there is always a significant fraction of hot electrons with energies ε corresponding to the SEE coefficient $\sigma(\varepsilon) > 1$.

The development of adequate theoretical DL models applicable to a wide temperature range is a very important problem, primarily, because such models will allow one to determine the near-wall electron conductivity and heat fluxes onto the wall in various plasma devices [4–8]. To do this requires knowledge of the distribution function of the secondary electrons. For a given distribution of the incident particles, the DL theory should be based on the Vlasov equation for the electron distribution function (EDF) $f(t, \mathbf{r}, \mathbf{v})$ in a self-consistent electric field $\mathbf{E}$ and a given magnetic field $\mathbf{H}$,

$$\frac{\partial f}{\partial t} + \mathbf{v}\cdot\frac{\partial f}{\partial \mathbf{r}} - \frac{e}{m}\left(\mathbf{E} + \frac{1}{c}\mathbf{v}\times\mathbf{H}\right)\cdot\frac{\partial f}{\partial \mathbf{v}} = 0,$$
$$\Delta\Phi = -4\pi e(n_i - \int f d\mathbf{v}) \qquad (2)$$

supplemented with the relevant boundary conditions. In a number of important applications, the effect of the magnetic field on the electrons can be ignored because the Debye length is usually one order of magnitude less than the electron Larmor radius.

In [9], we proposed a time-dependent one-dimensional kinetic model that was aimed at describing the general features of DLs with allowance for SEE over a wide temperature range. In this model, a number of simplifying assumptions were made. The main assumptions (besides ignoring the effect of the magnetic field) were as follows: (i) the velocity and density of the incident ions are fixed and (ii) the electrons arriving at the wall from infinity obey a Maxwellian distribution. For low electron temperatures, the model predicts that, regardless of the initial conditions, a steady-state Debye layer with a width on the order of the Debye length forms near the wall, the wall is charged negatively, and the electron density is minimal near the wall. When the electron temperature exceeds a certain critical value, the situation changes radically and an anti-Debye layer forms near the wall, that is, the wall is positively charged, so that its potential is higher than the plasma potential and the electron density is maximal near the wall. This regime turned out to be nonsteady. Further analysis showed that the nonsteady behavior of the layer stems from the boundary condition for plasma electrons: regardless of the processes in the layer, the density of the incident electrons was assumed to be fixed and, therefore, the plasma

1063-780X/04/3004-0299$26.00 © 2004 MAIK "Nauka/Interperiodica"

quasineutrality condition could be violated at large distances from the wall. The boundary condition used in [9], while quite reasonable from both mathematical and physical points of view, corresponds, however, to a somewhat different physical situation. It therefore becomes necessary to answer the questions about the existence and properties of steady-state solutions of the anti-Debye type and to give an adequate formulation of the problem. It is these issues that will be considered in the present paper.

2. TIME-DEPENDENT ONE-DIMENSIONAL MODEL

In [9], we proposed one of the possible formulations of a time-dependent one-dimensional problem of the DL structure near a dielectric wall with allowance for SEE. The model can be briefly described as follows: Let x be a coordinate across the DL ($x = 0$ corresponds to a certain plane located in the plasma far away from the wall, while $x = L$ corresponds to the wall position) and V be the x component of the electron velocity. For the electron distribution function $f(t, x, V)$, we have

$$\frac{\partial f}{\partial t} + V\frac{\partial f}{\partial x} - \frac{e}{m}E\frac{\partial f}{\partial V} = 0, \quad (3)$$

where E is the x component of the electric field, whose potential $\phi(x)$ satisfies Poisson's equation

$$\frac{d^2\phi}{dx^2} = -4\pi e(n_i - n_e) \quad (4)$$

with the boundary condition $\phi(0) = 0$.

In [9], the ion density n_i and velocity V_i were assumed to be fixed within the layer: $n_i = n_{i0} \equiv \text{const}$, and $V_i = V_{i0} \equiv \text{const}$. If the potential decreases monotonically toward the wall, then the deviation of the ion velocity and density from being constant can easily be found in the hydrodynamic approximation:

$$\frac{\partial n_i}{\partial t} + \frac{\partial (n_i V_i)}{\partial x} = 0, \quad \frac{\partial (n_i V_i)}{\partial t} + \frac{\partial (n_i V_i^2)}{\partial x} = \frac{e n_i}{M}E. \quad (5)$$

The boundary condition for the EDF in plasma is set as follows: at $x = 0$ and $V > 0$, the electrons obey the Maxwellian distribution

$$f(t, 0, V) = n_{e0}\left(\frac{m}{2\pi T_{e0}}\right)^{1/2}\exp\left(-\frac{mV^2}{2T_{e0}}\right) \equiv f_0\left(\frac{mV^2}{2}\right), \quad (6)$$

where n_{e0} and T_{e0} are the plasma electron density and temperature, which are assumed to be known.

In order to deduce the equation for the surface charge density ρ on the dielectric wall and to set the boundary condition for f at $x = L$, it is necessary to assume a certain model of SEE at the wall. We suppose that, when an electron with energy ε_p collides with the wall, one of three possible events occurs: (i) the incident electron disappears and the wall acquires a negative charge, (ii) one secondary electron with energy ε is knocked out of the wall, and (iii) two secondary electrons with energies ε_1 and ε_2 are knocked out of the wall. Let $P_0(\varepsilon_p)$ be the probability of the first event, $P_1(\varepsilon, \varepsilon_p)$ be the probability of the second event, and $P_2(\varepsilon_1, \varepsilon_2, \varepsilon_p)$ be the probability of the third event. We introduce the following quantities: $W_0(\varepsilon_p) = P_0(\varepsilon_p)$, $W_1(\varepsilon_p) = \int P_1(\varepsilon, \varepsilon_p)d\varepsilon$ (the probability of one secondary electron emerging), and $W_2(\varepsilon_p) = \int P_2(\varepsilon_1, \varepsilon_2, \varepsilon_p)d\varepsilon_1 d\varepsilon_2$ (the probability of two secondary electrons emerging). We then find that the SEE coefficient $\sigma(\varepsilon_p)$, which is the average number of the secondary electrons knocked out by an electron with energy ε_p, is

$$\sigma(\varepsilon_p) = W_1(\varepsilon_p) + 2W_2(\varepsilon_p),$$

and the normalizing condition is

$$W_0(\varepsilon_p) + W_1(\varepsilon_p) + W_2(\varepsilon_p) = 1. \quad (7)$$

We also introduce the quantity $P_{21}(\varepsilon, \varepsilon_p) = P_{22}(\varepsilon, \varepsilon_p) = \int P_2(\varepsilon_1, \varepsilon_2, \varepsilon_p)d\varepsilon_1$, which is the probability that exactly two secondary electrons are emitted, one of which has energy ε.

Assuming that every ion incident onto the wall is neutralized by an electron residing on the wall, the equation for the surface charge density ρ can be written in the form

$$\frac{d\rho}{dt} = e(n_i V_i)\big|_{x=L} - e\int_0^\infty Vf(t, L, V)[1 - \sigma(\varepsilon)]dV. \quad (8)$$

To set the boundary condition for EDF at $x = L$, we first write out the expression for the number of secondary electrons

$$|V|F^-(\varepsilon)d\varepsilon = \int_0^\infty V_p F^+(\varepsilon_p)d\varepsilon_p[P_1(\varepsilon, \varepsilon_p) + 2P_{21}(\varepsilon, \varepsilon_p)]d\varepsilon,$$

where the functions $F^+(\varepsilon)$ and $F^-(\varepsilon)$ are the electron energy distribution functions of the primary (incident) and secondary (reflected) electrons, respectively. Finally, in terms of velocity distribution, we have

$$f(t, L, V) = m\int_0^\infty [P_1(\varepsilon, \varepsilon_p) + 2P_{21}(\varepsilon, \varepsilon_p)]V_p f(t, L, V_p)dV_p, \quad (9)$$

$$V < 0.$$

The functions describing SEE were chosen as follows:[1]

$$W_0(\varepsilon) = P_0 \exp\left(-\frac{\varepsilon^2}{\alpha_0^2}\right), \quad W_2(\varepsilon) = 1 - \exp\left(-\frac{\varepsilon^2}{\alpha_2^2}\right). \quad (10)$$

The function $W_1(\varepsilon)$ was then determined from normalizing condition (7). The parameters P_0, α_0, and α_2 must be chosen such that $W_1(\varepsilon) \geq 0$. The model functions describing the spectrum of secondary electrons are chosen to agree with expressions (10). It is also taken into account that the total energy of secondary electrons cannot exceed the energy of the incident electron. We assume that

$$P_1(\varepsilon, \varepsilon_p) = \begin{cases} 4P_{10}\dfrac{\varepsilon}{\varepsilon_p}\left(1 - \dfrac{\varepsilon}{\varepsilon_p}\right), & \varepsilon \leq \varepsilon_p, \\ 0, & \varepsilon > \varepsilon_p, \end{cases} \quad (11)$$

$$P_2(\varepsilon_1, \varepsilon_2, \varepsilon_p) = \begin{cases} 4P_{20}\dfrac{\varepsilon_1 + \varepsilon_2}{\varepsilon_p}\left(1 - \dfrac{\varepsilon_1 + \varepsilon_2}{\varepsilon_p}\right), & \varepsilon_1 + \varepsilon_2 \leq \varepsilon_p, \\ 0, & \varepsilon_1 + \varepsilon_2 > \varepsilon_p, \end{cases} \quad (12)$$

where P_{10} and P_{20} are functions of ε_p. We then obtain $P_{10}(\varepsilon_p) = \dfrac{3}{2\varepsilon_p} W_1(\varepsilon_p)$ and $P_{20}(\varepsilon_p) = \dfrac{3}{\varepsilon_p^2} W_2(\varepsilon_p)$. We also have

$$P_{21}(\varepsilon, \varepsilon_p) = \begin{cases} 2\dfrac{W_2(\varepsilon_p)}{\varepsilon_p}\left[2\left(\dfrac{\varepsilon}{\varepsilon_p}\right)^3 - 3\left(\dfrac{\varepsilon}{\varepsilon_p}\right)^2 + 1\right], & \varepsilon \leq \varepsilon_p, \\ 0, & \varepsilon > \varepsilon_p. \end{cases} \quad (13)$$

Equations (3)–(5) and (8) are the basic equations of our time-dependent model. To complete the formulation of the problem, we also need to set a certain boundary condition for ϕ at $x = L$.

3. TIME-INDEPENDENT ONE-DIMENSIONAL MODEL

The main aim of this paper is to obtain and investigate steady-state solutions to the problem formulated above. The basic equations then reduce to

$$V\frac{\partial f(x, V)}{\partial x} - \frac{e}{m}E(x)\frac{\partial f(x, V)}{\partial V} = 0, \quad (14)$$

$$\frac{d}{dx}(n_i V_i) = 0, \quad \frac{d}{dx}(n_i V_i^2) = \frac{en_i}{M}E, \quad (15)$$

$$\frac{d^2\phi}{dx^2} = -4\pi e(n_i - n_e), \quad (16)$$

$$(n_i V_i)\big|_{x=L} = \int_0^\infty V f(L, V)[W_0(\varepsilon) - W_2(\varepsilon)]dV, \quad \varepsilon = \frac{mV^2}{2}, \quad (17)$$

where $n_e(x) = \int f(x, V)dV$ and $E(x) = -\dfrac{d\phi}{dx}$, and the boundary conditions are

$$x = 0: \phi = 0, \quad n_i = n_{i0}, \quad V_i = V_{i0}, \quad f(0, V) = f_0\left(\frac{mV^2}{2}\right), \quad V > 0, \quad (18)$$

$$x = L: \phi = \phi_L, \quad f(L, V) = \int_0^\infty G(V, V_p) f(L, V_p)dV_p, \quad V < 0. \quad (19)$$

Here, the potential ϕ, which is still unknown, can be either positive or negative (at $\phi_L < 0$, we have $|\phi_L| = U_D$) and

$$G(V, V_p) = m\left[P_1\left(\frac{mV^2}{2}, \frac{mV_p^2}{2}\right) + 2P_{21}\left(\frac{mV^2}{2}, \frac{mV_p^2}{2}\right)\right]V_p.$$

For ions, we have

$$n_i V_i = n_{i0} V_{i0}, \quad \frac{MV_i^2}{2} + e\phi(x) = \frac{MV_{i0}^2}{2}.$$

Our main aim here is to find layer-type solutions to Eqs. (14)–(17). In this case, the plasma parameters vary significantly only near the wall (within a layer with a thickness on the order of the Debye length). As the distance from the wall increases, all the parameters must tend to constant values. The method for solving the problem depends significantly on the function $\phi(x)$, which, in turn, is mainly determined by the electron temperature T_{e0} and the SEE parameters P_0, α_0, and α_2. For definiteness, we set $P_0 = 0.9$ and assume the length L to be much longer than the Debye length r_D ($L = 10r_D$, where $r_D^2 = T_{e0}/(4\pi e^2 n_{i0})$).

4. THE CASE OF LOW ELECTRON TEMPERATURES (DEBYE LAYER)

We will vary the electron temperature T_{e0} starting from a sufficiently low value (more exactly, sufficiently high values of the parameters α_0/T_{e0} and α_2/T_{e0}). Figure 1 shows, as an example, the SEE parameters $W_0(\varepsilon)$,

[1] As far as we know, these functions have not yet been determined experimentally.

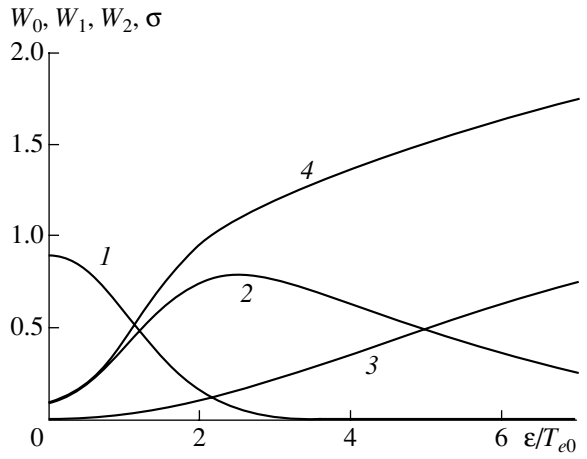

Fig. 1. SEE functions for $\alpha_0/T_{e0} = 1.5$ and $\alpha_2/T_{e0} = 6$: (*1*) $W_0(\varepsilon)$, (*2*) $W_1(\varepsilon)$, (*3*) $W_2(\varepsilon)$, and (*4*) $\sigma(\varepsilon)$.

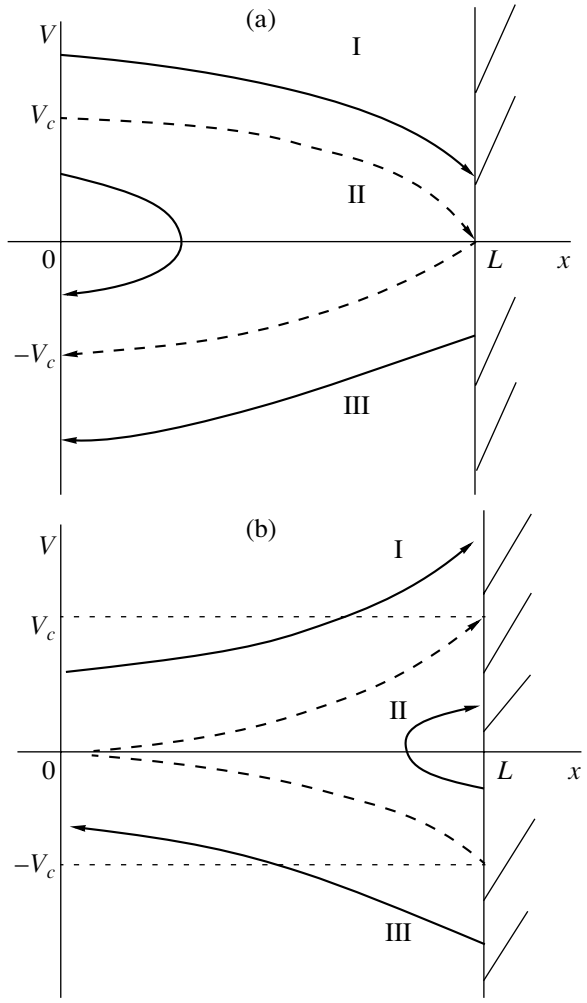

Fig. 2. Electron phase portraits for (a) low and (b) high electron temperatures.

$W_1(\varepsilon)$, $W_2(\varepsilon)$, and $\sigma(\varepsilon)$ as functions of the electron energy for $\alpha_0/T_{e0} = 1.5$ and $\alpha_2/T_{e0} = 6$. We assume that the potential $\phi(x)$ decreases monotonically, so that $\phi_L < 0$. The electron phase portrait for this case is shown in Fig. 2a, where $V_c = (-2e\phi_L/m)^{1/2}$. The problem is solved as follows: Any solution to Eq. (14) is a function of the total electron energy $\varepsilon = mV^2/2 - e\phi(x)$. Phase space in Fig. 2a can be divided into three domains: (I) $\varepsilon > -e\phi_L$, $V > 0$; (II) $\varepsilon \le -e\phi_L$; and (III) $\varepsilon > -e\phi_L$, $V < 0$. Within domains I and II, the EDF is dominated by the electrons arriving from the left boundary. Hence, in these domains, we have $f(x, V) = f_0(mV^2/2 - e\phi(x))$, and the EDF at $x = L$ can be expressed through the potential: $f(L, V) = f_0(mV^2/2 - e\phi_L)$ for $V > 0$. From balance relation (17), we determine ϕ_L (the parameters of the problem must be such that $\phi_L < 0$). From boundary condition (19), we then find that $f(L, V) = \int_0^\infty Gf(L, V_p)dV_p$ for $V_p < 0$. Finally, integrating the kinetic equation along characteristics, we find the EDF in domain III: $f(x, V) = f\left(L, -\sqrt{V^2 - \frac{2e}{m}(\phi(x) - \phi_L)}\right)$. Thus, we have found the EDF and, therefore, the electron density $n_e(\phi) = \int f dV$ as functions of the potential ϕ. Hence, the problem is reduced to a nonlinear boundary-value problem for the electric potential:

$$\frac{d^2\phi}{dx^2} = -4\pi e[n_i(\phi) - n_e(\phi)], \quad \phi(0) = 0, \qquad \phi(L) = \phi_L, \tag{20}$$

where $n_i(\phi) = \frac{n_{i0}V_{i0}}{\sqrt{V_{i0}^2 - \frac{2e\phi}{M}}}$. By solving (20), we find $\phi(x)$, $n_i(x)$, $V_i(x)$, and $f(x, V)$.

For the chosen SEE parameters, balance relation (17) yields the following equation for ϕ_L:

$$\phi_L = -\frac{T_{e0}}{e}\ln\left(\frac{A}{\sqrt{2\pi}}\frac{n_{e0}V_{e0}}{n_{i0}V_{i0}}\right). \tag{21}$$

Here,

$$V_{e0} = \sqrt{\frac{T_{e0}}{m}}, \quad A = -1 + P_0\varsigma\left(\frac{\alpha_0}{T_{e0}}\right) + \varsigma\left(\frac{\alpha_2}{T_{e0}}\right),$$

$$\varsigma(x) = x\int_0^\infty \frac{t\exp(-t^2)}{\sqrt{t^2 + \left(\frac{x}{2}\right)^2}}dt = \frac{\sqrt{\pi}}{2}x\exp\left[\left(\frac{x}{2}\right)^2\right]\left[1 - \mathrm{erf}\left(\frac{x}{2}\right)\right],$$

where $\mathrm{erf}(x)$ is the error function.

At low electron temperatures (i.e., at $\alpha_0/T_{e0} \gg 1$ and $\alpha_2/T_{e0} \gg 1$), we have $A \approx P_0 > 0$ and, accordingly, $\phi_L < 0$. In this case, it is natural to assume that $n_{e0} \approx n_{i0}$ and $V_{i0} \ll V_{e0}$. We will assume below that $V_{i0} = 0.1V_{e0}$ and $n_{e0} = 1.05n_{i0}$ (we recall that n_{e0} is the density of the electrons incident onto the wall). For definiteness, we will also assume in our numerical calculations, that $\alpha_2 = 4\alpha_0$. For $\mu = m/M < 0.01$, the ion motion affects the profiles of the potential and the electron density only slightly. In this case, the only parameter on which the solution to the problem depends is $\lambda_0 = \alpha_0/T_{e0}$. As an illustration, the table presents ϕ_L and $n_e(L)$ as functions of this parameter (the case of low temperatures, considered in this section, corresponds to the first three rows). The profiles of the potential and the electron density are shown in Figs. 3 and 4 (curves *1–3*). Finally, Fig. 5 shows the EDFs at three spatial points corresponding to three values of the potentials for two different values of the parameter λ_0.

Therefore, when the electron temperature is low enough, both the potential and the electron density monotonically decrease toward the wall. At the wall, the potential ϕ_L and the electron density $n_e(L)$ increase with temperature. The wall surface is charged negatively. It can be seen from Fig. 2 that the EDF has a discontinuity at the electron characteristic passing through the point $x = L$, $V = 0$. The amplitude of this discontinuity depends on the SEE parameters.

There is a critical temperature (more exactly, a critical value of the parameter λ_0) at which the functions $\phi(x)$ and $n_e(x)$ become constants. This value can be found from the condition $\phi_L = 0$, from which we obtain the equation for λ_0

$$P_0\varsigma(\lambda_0) + \varsigma(4\lambda_0) = 1 + \sqrt{2\pi}\frac{V_{i0}n_{i0}}{V_{e0}n_{e0}}. \qquad (22)$$

Under the above assumptions, the critical value of the parameter λ is equal to $\lambda_0^* \approx 0.71$. At larger values of λ, there is no solution corresponding to an ordinary Debye layer.

Table

λ_0	$e\phi_L/T_{e0}$	$n_e(L)/n_{i0}$
3	–1.15	0.21
1.5	–0.85	0.32
0.75	–0.11	0.85
0.625	0.24	1.22
0.5	0.38	1.72
0.25	0.34	3.3
0.15	–0.16	8.8

5. THE CASE OF HIGH ELECTRON TEMPERATURES (ANTI-DEBYE LAYER)

As the electron temperature increases (λ_0 decreases), the solution changes qualitatively and the potential $\phi(x)$ becomes a monotonically increasing function. Let us briefly describe the method for solving the problem in this case. Figure 2b shows the electron

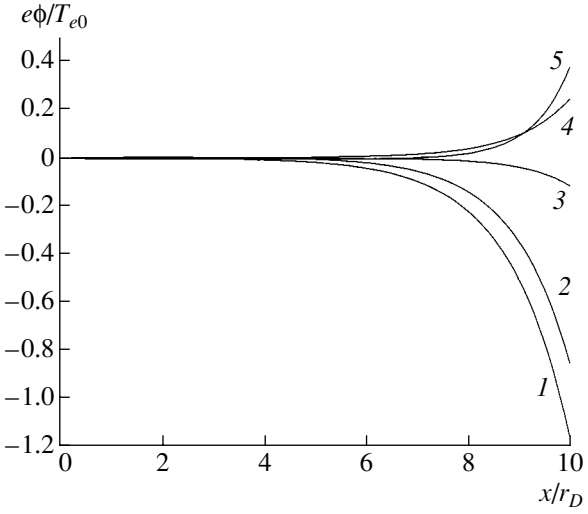

Fig. 3. Spatial profiles of the electric potential for different values of the parameter $\lambda_0 = \dfrac{\alpha_0}{T_{e0}}$ = (*1*) 3, (*2*) 1.5, (*3*) 0.75, (*4*) 0.625, and (*5*) 0.5.

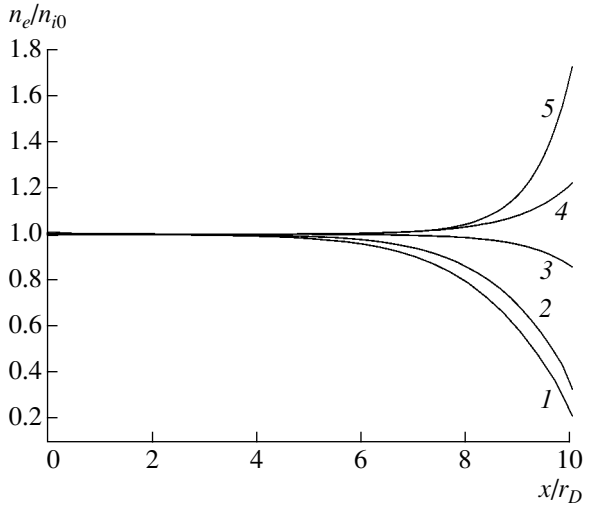

Fig. 4. Spatial profiles of the electron density for different values of the parameter $\lambda_0 = \dfrac{\alpha_0}{T_{e0}}$ = (*1*) 3, (*2*) 1.5, (*3*) 0.75, (*4*) 0.625, and (*5*) 0.5.

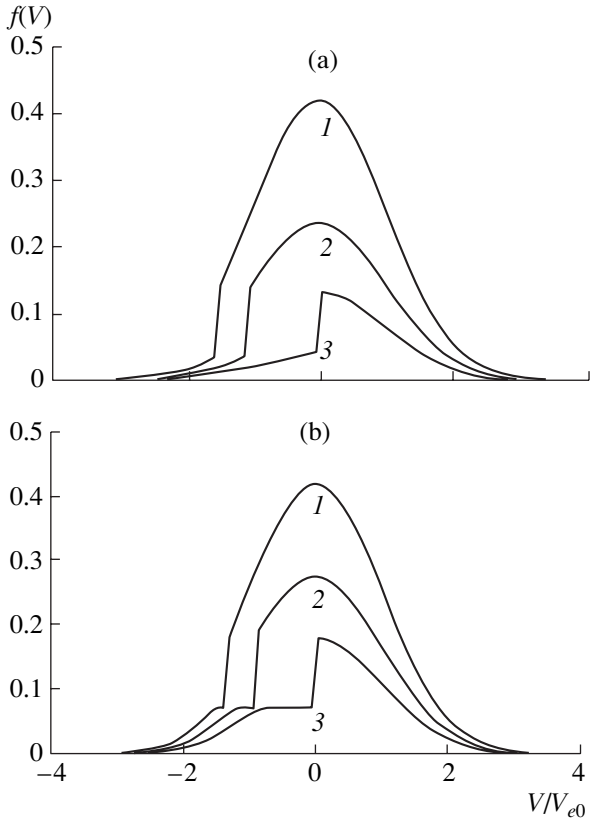

Fig. 5. Electron distribution function at three points corresponding to three values of the potential, ϕ = (*1*) 0, (*2*) $0.5\phi_L$, and (*3*) ϕ_L, in the case of a Debye layer for λ_0 = (a) 3 and (b) 1.5.

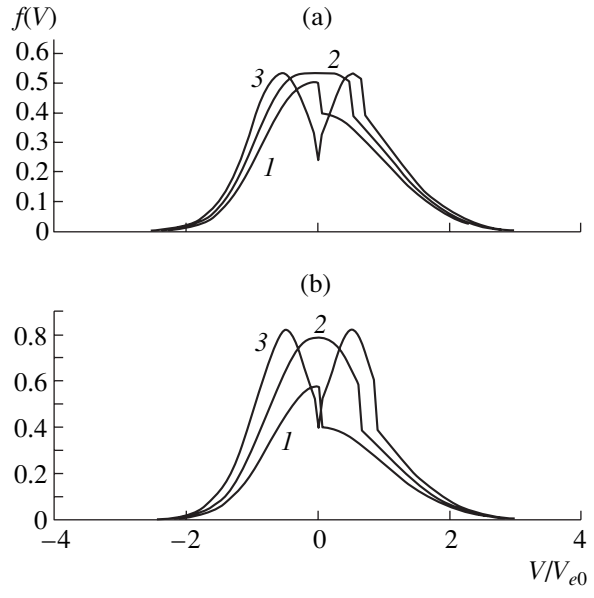

Fig. 6. Electron distribution function at three points corresponding to three values of the potential, ϕ = (*1*) 0, (*2*) $0.5\phi_L$, and (*3*) ϕ_L, in the case of an anti-Debye layer for λ_0 = (a) 0.625 and (b) 0.5.

phase portrait, where now $V_c = (2e\phi_L/m)^{1/2}$. There are three characteristic domains in Fig. 2b: (I) $\varepsilon > 0$, $V > 0$; (II) $\varepsilon \le 0$; and (III) $\varepsilon > 0$, $V < 0$, where, as before, $\varepsilon = mV^2/2 - e\phi(x)$ is the total electron energy. A characteristic feature of the phase portrait in this case is the presence of the secondary electrons that return to the wall (domain II). In domain I, the EDF is determined only by the electrons arriving from infinity, so that we have $f(x, V) = f_0(mV^2/2 - e\phi(x))$ (specifically, $f(L, V) = f_0(mV^2/2 - e\phi_L)$ for $V > V_c$). Obviously, $f(L, V) = f(L, -V)$ for $0 \le V < V_c$. In view of the boundary condition (19), we have

$$f(L, V) = \int_0^\infty G(V, V_p) f(L, V_p) dV_p$$
$$= \int_0^{V_c} Gf\, dV_p + \int_{V_c}^\infty Gf\, dV_p.$$

Thus, we obtain an integral equation for the distribution function of secondary electrons at the wall ($x = L$, $V < 0$):

$$f(L, V) = s(V) + \int_0^{V_c} G(V, V_p) f(L, -V_p) dV_p, \quad V < 0, \tag{23}$$

with $s(V) = \int_{V_c}^\infty G(V, V_p) f_0(mV_p^2/2 - \phi_L) dV_p$. This function depends parametrically on ϕ_L. By solving Eq. (23), we find the EDF at $x = L$ (this equation can easily be solved by the method of successive approximations; even the zero approximation yields a quite satisfactory result).

Next, we determine ϕ_L using balance relationship (17). Integrating the kinetic equation along characteristics at a given potential at the wall ($\phi_L > 0$), we find the EDF as a function of ϕ and V over the entire phase space. As a result, we again arrive at nonlinear Poisson's equation (20), but with another function $n_e(\phi)$ on the right-hand side.

To illustrate solutions with a monotonically increasing potential, Figs. 3 and 4 show the profiles of the electric potential and the electron density, respectively, for $\lambda_0 = 0.625$ and $\lambda_0 = 0.5$. As before, $V_{i0} = 0.1V_{e0}$ and $n_{e0} = n_{i0}$. The corresponding values of ϕ_L and $n_e(L)$ are shown in the table. Figure 6 shows the EDFs at three spatial points: $x = 0$, $x = L$, and the point corresponding to $\phi = 0.5\phi_L$. The discontinuity in the distribution function is now on a characteristic lying in the upper half-plane of electron phase space. In the case of an anti-Debye potential layer, the problem of the role of ions is more complicated. The above solutions correspond to

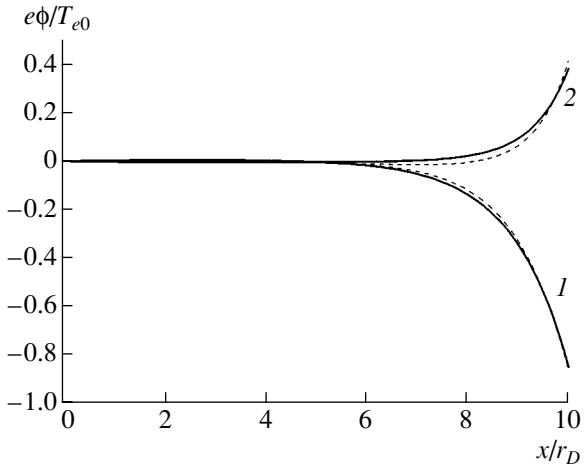

Fig. 7. Profiles of the electric potential calculated analytically (solid lines) and numerically (dashed lines) for λ_0 = (*1*) 1.5 and (*2*) 0.5.

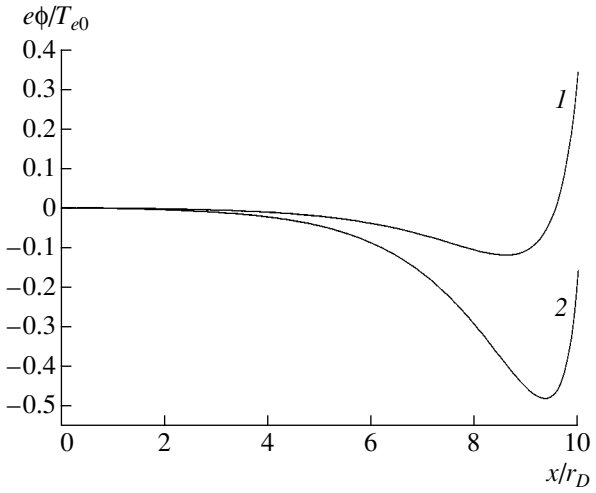

Fig. 8. Nonmonotonic profiles of the electrical potential for λ_0 = (*1*) 0.25 and (*2*) 0.15.

$\mu = m/M = 0.001$. For ions, the hydrodynamic approximation is certainly invalid when the ion energy at infinity is lower than the wall potential, $MV_{i0}^2/2 < e\phi_L$, so an ion is reflected from the wall.

Thus, we have shown that, at sufficiently high electron temperatures (such that $\lambda_0 < \lambda_0^*$), there exists a steady-state solution corresponding to an anti-Debye potential layer. The case of even higher temperatures ($\lambda_0 \le 0.3$) has not yet been studied analytically.

6. NON-STEADY-STATE SOLUTIONS AT HIGH ELECTRON TEMPERATURES

An alternative way of finding steady-state solutions is to solve the time-dependent problem numerically by the relaxation method, starting from rather arbitrary initial data. In this case, the question arises as to adequate boundary conditions for the EDF at $x = 0$. The previous boundary condition (6) does not automatically guarantee the physically obvious condition $n_i(0) = n_e(0)$, corresponding to plasma quasineutrality at large distances from the wall. For this reason, we set the condition $n_e(t, 0) = n_{i0}$ at $x = 0$. We also assume that $f(t, 0, V) = B(t)g(V)$, where $g(V) = (m/2\pi T_{e0})^{1/2}\exp(-mV^2/2T_{e0})$ is a known function and $B(t)$ is an unknown function to be determined from the quasineutrality condition $\int f(t, 0, V)dV = n_{i0}$. If we arrive at a steady-state solution at $t \longrightarrow \infty$, we then have $B(\infty) = n_{e0}$, which is the density of the incident particles in the steady-state case. It is in this boundary condition and the account taken of the ion dynamics in the hydrodynamic approximation [see Eqs. (5)] that the given model differs from the one proposed previously in [9]. The kinetic equation was solved numerically on 100×100 and 200×200 meshes by the finite difference method with an increased approximation order [10, 11].

The computations performed within the parameter range of interest (basically the parameter λ_0) show that the solution always relaxes to a steady-state one. The computed steady-state profiles of the potential and the electron density are very close to those obtained analytically (see Fig. 7). The EDF discontinuity in analytic solutions corresponds to a rather narrow zone in which the numerically calculated EDFs vary sharply.

Let us now consider the new features that are characteristic of numerical solutions only. The computations show that, as the temperature ($\lambda_0 \le 0.3$) increases further, the potential is no longer a monotonic function of x. Figure 8 shows the profiles of the potential for $\lambda_0 = 0.25$ and $\lambda_0 = 0.15$. Note that the electron density profiles remain monotonic (the values of the electron density at the wall are given in the table).

In fact, the above plasma quasineutrality condition, which was used to find the EDF, is only a certain idealization. It is of interest to study the effect of various non-steady-state perturbations on the solutions obtained. For this purpose, we performed calculations with a perturbed boundary condition, namely, it was assumed that the quasineutrality condition at $x = 0$ is slightly violated and holds only on average: $n_e(t, 0) = n_{i0}[1 + \delta\sin(\omega t)]$. The calculations were performed at $\delta = 0.05$, $\omega = k\omega_p$, $\omega_p^2 = 4\pi n_{i0}e^2/m$, and $k = 0.5$–2.0. The results obtained show that the oscillation amplitude of a periodic solution depends on k and is maximal at $k = 1$. The wall potential oscillates with the highest amplitude, and this amplitude increases with temperature. The evolution of $\phi(t, L)$ for three values of λ_0 is shown in Fig. 9. The time-averaged profiles of the potential and the electron density are close to the corresponding steady-state profiles. Thus, perturbations do

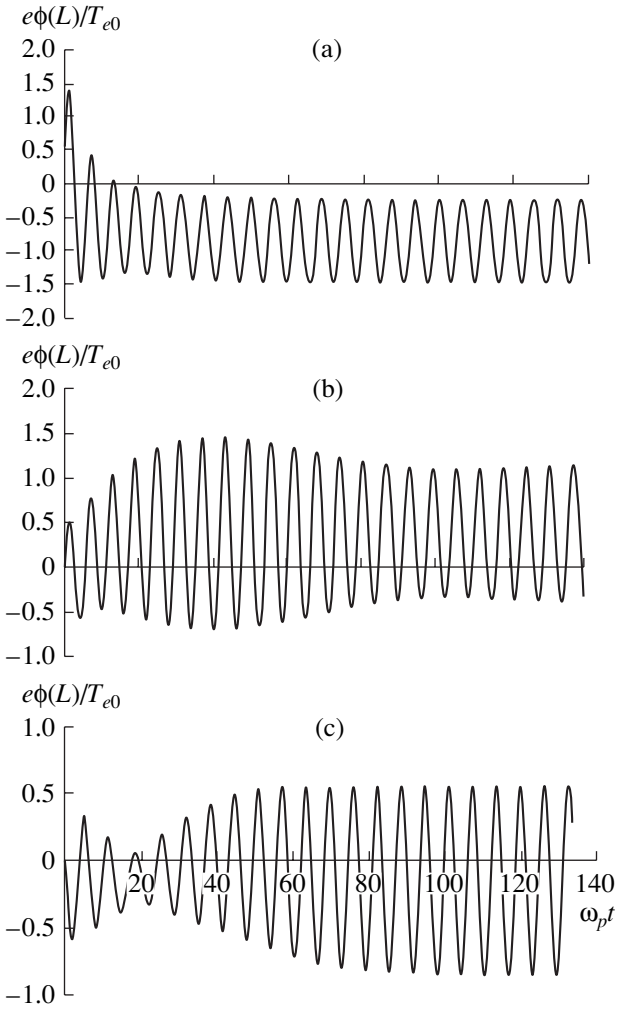

Fig. 9. Evolution of the wall potential for λ_0 = (a) 1.5, (b) 0.5, and (c) 0.15.

not affect the time-averaged (on a time scale much longer than the plasma period) profiles of the main plasma parameters. This is evidence in favor of the stability of the steady-state solutions obtained.

7. CONCLUSIONS

Exact steady-state analytic solutions describing kinetic processes in a low-density plasma layer near a dielectric surface have been found in a time-dependent one-dimensional kinetic model with allowance for secondary electron emission [9]. It has been shown that, at low electron temperatures, a Debye layer forms, in which the plasma potential and the electron density monotonically decrease toward the dielectric wall. As the electron temperature increases, an anti-Debye layer first forms, in which the potential monotonically increases toward the wall, and then regimes with a nonmonotonic potential profile arise. The solutions obtained are relatively stable against any small variation in the boundary conditions.

ACKNOWLEDGMENTS

This study was supported by the Russian Foundation for Basic Research, project nos. 03-01-00063 and 02-07-90027.

REFERENCES

1. A. I. Morozov, *Physical Principles of Electric Propulsion Engines* (Atomizdat, Moscow, 1978), p. 326.
2. O. A. Sinkevich and I. P. Stakhanov, *Plasma Physics* (Vysshaya Shkola, Moscow, 1991).
3. V. A. Rozhanskiĭ and L. D. Tsendin, *Collisional Transport in a Partially Ionized Plasma* (Énergoatomizdat, Moscow, 1988).
4. *Encyclopedia of Low-Temperature Plasma*, Ed. by V. E. Fortov (Nauka, Moscow, 2000), Introductory Volume, Part III, Section 9.5, p. 444.
5. A. I. Morozov and V. V. Savelyev, in *Reviews of Plasma Physics*, Ed. by B. B. Kadomtsev and V. D. Shafranov (Consultants Bureau, New York, 2000), Vol. 21, p. 203.
6. A. I. Bugrova, A. I. Morozov, and V. K. Kharchevnikov, Fiz. Plazmy **18**, 963 (1992) [Sov. J. Plasma Phys. **18**, 501 (1992)].
7. A. I. Morozov and V. V. Savel'ev, Fiz. Plazmy **27**, 607 (2001) [Plasma Phys. Rep. **27**, 570 (2001)].
8. A. I. Morozov, Fiz. Plazmy **17**, 672 (1991) [Sov. J. Plasma Phys. **17**, 393 (1991)].
9. A. I. Morozov and V. V. Savel'ev, Fiz. Plazmy **28**, 1103 (2002) [Plasma Phys. Rep. **28**, 1017 (2002)].
10. C. Z. Cheng and G. Knorr, J. Comput. Phys. **22**, 330 (1976).
11. P. K. Smolarkiewitcz, J. Comput. Phys. **54**, 325 (1984).

Translated by N.N. Ustinovskiĭ

Plasma Physics Reports, Vol. 30, No. 4, 2004, pp. 307–317. Translated from Fizika Plazmy, Vol. 30, No. 4, 2004, pp. 339–348.

PLASMA KINETICS

Turbulent Ion Heating in a Plasma with Two Ion Species

I. V. Kuzora, V. P. Silin, and S. A. Uryupin

Lebedev Physical Institute, Russian Academy of Sciences, Leninskiĭ pr. 53, Moscow, 119991 Russia

Received May 26, 2003; in final form, July 22, 2003

Abstract—A description of ion heating by ion-acoustic turbulence in a plasma containing two ion species of different charge-to-mass ratio is presented. It is shown that, when collisions between ions of different species are ignored, only one of the ion species is heated substantially while the temperature of the other species approaches a constant value that differs insignificantly from the initial ion temperature. The only exception to this is a case in which the plasma parameters are in a particular relationship. For an example of a fully ionized HO plasma, it is shown that taking into account the collisional energy exchange between different ion species removes this restriction on the ion temperature. © *2004 MAIK "Nauka/Interperiodica".*

1. INTRODUCTION

It is well known that, in a plasma with a developed ion-acoustic turbulence (IAT), the bulk of thermal ions with velocities lower than the ion-acoustic velocity are subject to efficient heating (see, e.g., [1, 2]). In the IAT theory, turbulent ion heating is attributed to the stimulated scattering of ion-acoustic waves by ions [3, 4]. In this case, the time scale on which the ion temperature doubles is much less than the inverse effective frequency of the energy relaxation in electron–ion collisions. There are a fairly large number of studies on the theory of turbulent ion heating in a plasma with a single ion species (see, e.g., [5–10]). Thus, Rudakov [6] formulated turbulent heating equations that qualitatively characterize the relationship between the energy transferred from the ion-acoustic waves to the ions and the energy lost by the ions in, e.g., collisions with electrons. Like Kovrizhnykh in his earlier paper [5], Rudakov pointed out that, because of the quasilinear resonant interaction with waves, the ions whose velocities exceed the ion-acoustic velocity are heated at a faster rate than the slower ions that are the subject of the present study. Kingsep [7] systematically derived equations for the ion distribution function from the nonlinear theory of wave interaction and noticed that, when ion–ion collisions are ignored, the solution to these equations can be substantially non-Maxwellian. In [8, 9], anisotropic turbulent ion heating was described in terms of the self-consistent IAT theory. However, for a plasma with several ion species, the theory of IAT spectra and the theory of turbulent ion heating yield a number of qualitatively new effects that stem primarily from the fact that, in a plasma containing several ion species of different charge-to-mass ratio, the probability of stimulated scattering is higher than in a plasma with a single ion species [11]. Interest in a plasma with several ion species has persisted for quite a long time (see, e.g., [12–18]); however, the IAT spectrum for such a plasma has been obtained only recently [11, 19, 20]. A description of turbulent ion heating in a plasma with two ion species of the same charge-to-mass ratio was given in our earlier paper [21], in which it was shown that, under conditions of turbulent ion heating, the temperatures of the two ion species are the same and increase linearly at equal rates, as is the case in a plasma with a single ion species. In the present work, we quantitatively describe a turbulent heating of the bulk of thermal ions in a plasma with two ion species of different charge-to-mass ratio.

In the next section, we will present the required information on the IAT spectrum in a plasma with several ion species. Then, using the ion kinetic equations, we will derive equations for the temperatures of different ion species. Further, we will investigate the time evolution of the ion temperatures in a turbulent plasma with two ion species. We will show that, when collisions between ions of different species are ignored, the temperature of only one ion species increases continuously over time while the temperature of the other species approaches a constant value, the only exception being a case in which the plasma parameters are in a particular relationship. Finally, we will demonstrate that, under conditions of collisional energy exchange between ions of different species, their temperatures both increase over time, but the rates at which they increase may be different.

2. IAT SPECTRUM

In this section, following [20], we present the main results on the IAT spectrum that are required for a further description of ion heating in a plasma with two species of ions of masses m_1 and m_2 such that $m_1 < m_2$. We are working under the conditions

$$r_{De} \gg r_{D\alpha}, \quad Z_\alpha T_e \gg T_\alpha. \tag{2.1}$$

1063-780X/04/3004-0307$26.00 © 2004 MAIK "Nauka/Interperiodica"

Here, $r_{D\alpha} = \sqrt{\kappa T_\alpha/4\pi n_\alpha e_\alpha^2}$, n_α, $e_\alpha - Z_\alpha|e|$, and T_α are the Debye radius, density, charge, and temperature of the ions of species $\alpha = 1$ and 2; e, T_e, and r_{De} are the charge, temperature, and Debye radius of the electrons; and κ is Boltzmann's constant. The dispersion relation of the ion-acoustic waves that can exist under these conditions has the form

$$\omega_s = kv_s/\sqrt{1 + (kr_{De})^2}, \tag{2.2}$$

where $v_s = \omega_L r_{De}$ is the ion-acoustic velocity, $\omega_L^2 = \omega_{L1}^2 + \omega_{L2}^2$, and $\omega_{L\alpha} = \sqrt{4\pi n_\alpha e_\alpha^2/m_\alpha}$ is the Langmuir frequency of the ions of species α. Generally, in a plasma with two ion species of vastly different masses, there may be, in addition to waves with frequency (2.2), low-frequency ion-acoustic waves with a much lower phase velocity. However, as was shown in [20], such low-frequency waves can exist only if the ratio of the Debye radius of the lighter ions to the Debye radius of the heavier ions is much larger than unity. Since the ratio r_{D1}/r_{D2} is equal to $(T_1 Z_2^2 n_2/T_2 Z_1^2 n_1)^{1/2}$, the condition $r_{D1} > r_{D2}$ is satisfied for a comparatively high density of heavier ions such that $n_2/n_1 \gg (Z_1^2/Z_2^2)(T_2/T_1)$. In what follows, however, we assume that this condition is not satisfied, thereby restricting ourselves to considering plasmas in which the only possible waves are those that obey dispersion law (2.2).

We consider a situation in which the IAT is driven by a force with the density $\mathbf{R} = (0, 0, R)$ acting on the electrons. Here, $R = en_e E - \partial p/\partial z > 0$, where n_e and p are the electron density and electron pressure. When the electron drift velocity is higher than the ion-acoustic velocity, the stimulated Cherenkov emission of ion-acoustic waves comes into play. In this case, the quasi-steady level to which the ion-acoustic noise relaxes in the plasma is determined by the competition between, on the one hand, Cherenkov emission of waves by electrons, and, on the other, Cherenkov absorption of waves by ions and nonlinear damping of ion-acoustic waves by stimulated scattering by ions of both species. The resulting distribution of the number N of ion-acoustic waves over the wavenumbers k and over the angles θ determining the orientation of the wave vector has the form [11, 20]

$$N(k, \cos\theta) = \Phi(\cos\theta)\sqrt{\frac{\pi}{2}}\frac{\omega_L^6 r_{De}}{\omega_{Le}} \times \frac{(r_{D1}^2 + r_{D2}^2)^2}{(v_{T1}^2 r_{D1}^2 + v_{T2}^2 r_{D2}^2)}\left(\frac{e_1}{m_1} - \frac{e_2}{m_2}\right)^{-2} k^{-4}(1 + k^2 r_{De}^2)^{-1} \times \left[\ln\frac{1 + \sqrt{1 + k^2 r_{De}^2}}{kr_{De}} - \frac{1}{(1 + k^2 r_{De}^2)^{1/2}} - \frac{1}{3(1 + k^2 r_{De}^2)^{3/2}}\right], \tag{2.3}$$

where θ is the angle between $\mathbf{k}$ and $\mathbf{R}$, ω_{Le} is the electron Langmuir frequency, and $v_{T\alpha} = \sqrt{\kappa T_\alpha/m_\alpha}$ is the thermal velocity of the ions of species α. The IAT spectrum in a plasma with two ion species can be described by formula (2.3) when the charge-to-mass ratios of the species differ greatly from one another:

$$\left(\frac{e_1}{m_1} - \frac{e_2}{m_2}\right)^2 \frac{r_{De}^2}{r_{D1}^2} \gg \frac{(r_{D1}^2 + r_{D2}^2)^2 \omega_{L1}^2}{v_{T1}^2 r_{D1}^2 + v_{T2}^2 r_{D2}^2}\left[\left(\frac{e_1\omega_{L1}}{m_1\omega_L}\right)^2 + \left(\frac{e_2\omega_{L2}v_{T2}}{m_2\omega_L v_{T1}}\right)^2\right]. \tag{2.4}$$

If condition (2.4) fails to hold, the IAT spectrum depends on $\mathbf{k}$ in the same manner as in a plasma with a single ion species. In distribution (2.3), the explicit form of the angular dependence $\Phi(\cos\theta)$ is determined by the value of the turbulent Knudsen number:

$$K_N = \left(\frac{e_1}{m_1} - \frac{e_2}{m_2}\right)^2 \frac{6\pi^2}{\lambda}\frac{R\omega_{Le}^2}{v_s\omega_L^7}\frac{v_{T1}^2 r_{D1}^2 + v_{T2}^2 r_{D2}^2}{(r_{D1}^2 + r_{D2}^2)^2}, \tag{2.5}$$

where $\lambda \cong 0.55$. In what follows, we need only the moments $M_n \equiv \int_0^1 dx\Phi(x)x^n$ of the function $\Phi(\cos\theta)$. In the limit of small Knudsen numbers, $K_N < (1 + \delta)^2$, the moments M_n have the form

$$M_n = \frac{4K_N}{3\pi(1 + \delta)}\left[\varepsilon^{\alpha_\varepsilon - 1} - \frac{1 - \varepsilon^{\alpha_\varepsilon}}{\alpha_\varepsilon}(n - 1)\right], \quad n = 0, 1, \ldots. \tag{2.6}$$

Here, the small parameters ε and α_ε are given by the approximate expressions [11] $\alpha_\varepsilon \cong \ln 2/\ln[(1 + \delta)^2/K_N]$ and $\varepsilon \cong 2K_N/[3\pi(1 + \delta)^2\alpha_\varepsilon]$, with $\delta = \delta_1 + \delta_2$, in which the parameter $\delta_\alpha = n_e\omega_{L\alpha}^2 f_\alpha(v_s)/n_\alpha\omega_{Le}^2 f_e(v_s)$ is proportional to the ratio of the value of the distribution function of hot resonant ions of species α to the value of the electron distribution function at $v = v_s$. In the opposite limit $K_N \gg (1 + \delta)^2$, the angular distribution contains the factor $\sqrt{K_N}$ and its moments are equal to [11]

$$M_0 = 2.47\sqrt{K_N}, \quad M_1 = 1.84\sqrt{K_N}, \quad M_2 = 1.44\sqrt{K_N}, \quad M_3 = 1.17\sqrt{K_N}. \tag{2.7}$$

3. EQUATIONS FOR THE ION TEMPERATURES

Here, using the above information on the IAT spectrum, we derive equations for the temperatures of the bulk of thermal ions with velocities $v < v_s$. The kinetic equation for thermal ions of species α has the form

$$\frac{\partial f_\alpha}{\partial t} = \sum_{\beta = 1, 2, e} \mathrm{St}[f_\alpha, f_\beta] + \frac{\partial}{\partial v_i}D_{ij}^{(\alpha)}\frac{\partial f_\alpha}{\partial v_j}, \tag{3.1}$$

where the Landau collision integral $\mathrm{St}[f_\alpha, f_\beta]$ describes collisions between ions of species α and ions of species β and the diffusion tensor $D_{ij}^{(\alpha)}$ in velocity space describes the stimulated scattering of waves by ions. We restrict ourselves to a Maxwellian distribution of ions with velocities $v < v_s$:

$$f_\alpha(v, t) = \frac{n_\alpha m_\alpha^{3/2}}{(2\pi\kappa T_\alpha(t))^{3/2}} \exp\left(-\frac{m_\alpha v^2}{2\kappa T_\alpha(t)}\right). \quad (3.2)$$

This can be the case if the frequencies of collisions between ions of species α are low in comparison with the characteristic frequencies of the interaction between ions of this species with waves [see formulas (3.9), (3.20) below]. The desired equations for the ion temperatures can be obtained from Eq. (3.1) by multiplying it by $\frac{m_\alpha}{3n_\alpha} v^2$ and then by integrating over velocities:

$$\frac{dT_\alpha}{dt} = -\frac{2m_\alpha}{3n_\alpha\kappa}\int d\mathbf{v}\, v_i D_{ij}^{(\alpha)} \frac{\partial f_\alpha}{\partial v_j} + \sum_{\beta = e, 1, 2} \frac{(T_\beta - T_\alpha)}{\tau_{\alpha\beta}}. \quad (3.3)$$

Here, the effective time scales on which the energy is transferred between ions and from ions to electrons are given by the expression [22]

$$\tau_{\alpha\beta}^{-1} = \frac{4}{3}\frac{\pi e_\alpha^2 e_\beta^2 \Lambda n_\beta (m_\alpha m_\beta)^{3/2}}{(\kappa T_\alpha \kappa T_\beta)^{5/2}(2\pi)^3}\int d\mathbf{v}_\alpha d\mathbf{v}_\beta \times \exp\left[-\frac{m_\alpha v_\alpha^2}{2\kappa T_\alpha} - \frac{m_\beta v_\beta^2}{2\kappa T_\beta}\right] \times v_{\alpha i} v_{\beta j} \frac{(\mathbf{v}_\alpha - \mathbf{v}_\beta)^2 \delta_{ij} - (\mathbf{v}_\alpha - \mathbf{v}_\beta)_i (\mathbf{v}_\alpha - \mathbf{v}_\beta)_j}{|\mathbf{v}_\alpha - \mathbf{v}_\beta|^3}, \quad (3.4)$$

with Λ the Coulomb logarithm. The diffusion tensor in Eq. (3.3) has the form

$$D_{ij}^{(\alpha)} \cong \frac{(2\pi)^3}{2m_\alpha^2\omega_L^4}\int d\mathbf{k} d\mathbf{k}' \omega\omega'^3 k_i'' k_j'' N(\mathbf{k}) \times N(\mathbf{k}')\delta(\omega'' - \mathbf{k}''\cdot\mathbf{v})|\Lambda_\alpha(\mathbf{k}, \mathbf{k}')|^2. \quad (3.5)$$

Here, $\mathbf{k}'' = \mathbf{k} - \mathbf{k}'$ and $\omega'' = \omega - \omega'$ are the wave vector and beat frequency of the interacting waves and the amplitude $\Lambda_\alpha(\mathbf{k}, \mathbf{k}')$ under condition (2.4) is equal to [20]

$$\Lambda_\alpha(\mathbf{k}, \mathbf{k}') = \frac{e_\alpha}{(2\pi)^3\omega'}\left(\frac{e_\alpha}{m_\alpha} - \frac{e_\beta}{m_\beta}\right)\frac{\mathbf{k}\cdot\mathbf{k}'}{kk'} \times \frac{\delta\varepsilon_\beta(\omega'', k'')}{\delta\varepsilon_1(\omega'', k'') + \delta\varepsilon_2(\omega'', k'')}, \quad \beta \neq \alpha, \quad (3.6)$$

where

$$\delta\varepsilon_\alpha(\omega'', k'') = (k''r_{D\alpha})^{-2}\left[1 - J_+\left(\frac{\omega''}{k''v_{T\alpha}}\right)\right] \quad (3.7)$$

are the dielectric susceptibilities of the ions of different species at the beat frequency of the interacting waves and

$$J_+(x) = xe^{-x^2/2}\int_0^x dt e^{t^2/2} - i\sqrt{\frac{\pi}{2}}xe^{-x^2/2}. \quad (3.8)$$

We calculate the integrals over velocities in expression (3.4) in terms of the center-of-mass variables $\mathbf{v}_{\alpha\beta} = \mathbf{v}_\alpha - \mathbf{v}_\beta$ and $\mathbf{P} = m_\alpha\mathbf{v}_\alpha + m_\beta\mathbf{v}_\beta$ for which we have $d\mathbf{v}_\alpha d\mathbf{v}_\beta = (m_\alpha + m_\beta)^{-3} d\mathbf{v}_{\alpha\beta} d\mathbf{P}$. As a result, we obtain

$$\tau_{\alpha\beta}^{-1} = \frac{8\sqrt{2\pi}}{3}\frac{e_\alpha^2 e_\beta^2 \Lambda n_\beta (m_\alpha m_\beta)^{1/2}}{(m_\beta\kappa T_\alpha + m_\alpha\kappa T_\beta)^{3/2}}. \quad (3.9)$$

Below, we will be interested in the case of a plasma with two ion species of very different masses, $m_2 \gg m_1$. In this case, expression (3.9) yields

$$\tau_{12} = \frac{n_1}{n_2}\tau_{21} = \frac{3}{8\sqrt{2\pi}}\frac{m_2(\kappa T_1)^{3/2}}{m_1^{1/2} e_1^2 e_2^2 \Lambda}\frac{1}{n_2}. \quad (3.10)$$

The assumption that the ion species have appreciably different masses is not of fundamental importance for our analysis but it makes it possible to simplify an analytic description of the effect of ion–ion collisions on the heating of ions of different species.

We now consider the first term on the right-hand side of Eq. (3.3). In our analysis, this is the ion heating source term. Since the values of the ion distribution function at $v \sim v_s$ are exponentially small, the main contribution to the integral comes from the velocity range $v \sim v_{T\alpha} \ll v_s$. In this range, the δ function in formula (3.5) can be expanded in powers of the small parameter $vk''/\omega'' \sim v/v_s \ll 1$, in which case the first term on the right-hand side of Eq. (3.3) becomes

$$-\frac{2m_\alpha}{3n_\alpha\kappa}\int d\mathbf{v}\, v_i D_{ij}^{(\alpha)}\frac{\partial f_\alpha}{\partial v_j} \cong \frac{e_\alpha^2}{3(2\pi)^3 m_\alpha\omega_L^4\kappa}\left(\frac{e_1}{m_1} - \frac{e_2}{m_2}\right)^2 \frac{r_{D\alpha}^4}{(r_{D1}^2 + r_{D2}^2)^2} \times \int d\mathbf{k} d\mathbf{k}' \frac{\omega\omega'}{d\omega/dk}\delta(k - k')N(\mathbf{k})N(\mathbf{k}')(\mathbf{k} - \mathbf{k}')^2\left(\frac{\mathbf{k}\cdot\mathbf{k}'}{kk'}\right)^2. \quad (3.11)$$

Then, using IAT spectrum (2.3), we reduce expression (3.11) to

$$-\frac{2m_\alpha}{3n_\alpha\kappa}\int d\mathbf{v}\,v_i D_{ij}^{(\alpha)}\frac{\partial f_\alpha}{\partial v_j}$$
$$\cong \frac{\eta}{12}\frac{e_\alpha^2}{m_\alpha}\left(\frac{e_1}{m_1}-\frac{e_2}{m_2}\right)^{-2}\frac{r_{D\alpha}^4(r_{D1}^2+r_{D2}^2)^2}{(v_{T1}^2r_{D1}^2+v_{T2}^2r_{D2}^2)^2}\frac{\omega_L^7 v_s^2}{\omega_{Le}^2\kappa} \quad (3.12)$$
$$\times[M_0^2-3M_1^2+3M_2^2-5M_3^2-2M_0M_2+6M_1M_3],$$

where $\eta \cong 1.09$. According to formula (2.6), the bilinear combination of the moments in the square brackets in expression (3.12) is equal to $8K_N/(3\pi)$ in the limit $K_N < (1+\delta)^2$ and, in the opposite limit $K_N \gg (1+\delta)^2$, it is equal to $1.12\,K_N$. Substituting formula (2.5) for K_N into expression (3.12), we arrive at the following final expression for the first term on the right-hand side of Eq. (3.3):

$$A\frac{Rv_s}{n_\alpha\kappa}\frac{r_{D\alpha}^2v_{T\alpha}^2}{v_{T1}^2r_{D1}^2+v_{T2}^2r_{D2}^2}, \quad (3.13)$$

where $A = \eta/(3\lambda) \cong 0.66$ for $K_N < (1+\delta)^2$ and $A = 1.12\eta\pi/(8\lambda) = 0.87$ for $K_N \gg (1+\delta)^2$. With expression (3.13), Eq. (3.3) takes the form

$$\frac{dT_\alpha}{dt} = A\frac{Rv_s}{n_\alpha\kappa}\frac{r_{D\alpha}^2v_{T\alpha}^2}{v_{T1}^2r_{D1}^2+v_{T2}^2r_{D2}^2} + \frac{T_e-T_\alpha}{\tau_{\alpha e}}+\frac{T_\beta-T_\alpha}{\tau_{\alpha\beta}}, \quad (3.14)$$

where $\alpha \neq \beta$. We multiply Eqs. (3.14) by κn_α and add the resulting equations to obtain the equation describing the heating of the ion plasma component as a whole:

$$\frac{d(n_1\kappa T_1+n_2\kappa T_2)}{dt} = ARv_s+\frac{n_1\kappa(T_e-T_1)}{\tau_{1e}} + \frac{n_2\kappa(T_e-T_2)}{\tau_{2e}}. \quad (3.15)$$

The first term on the right-hand side of Eq. (3.15) describes the collisionless heating of plasma ions, and the second and third terms account for the heat redistribution between electrons and ions. From Eq. (3.15) we see that, under the inequality

$$ARv_s \gg \frac{n_1\kappa(T_e-T_1)}{\tau_{1e}}+\frac{n_2\kappa(T_e-T_2)}{\tau_{2e}}, \quad (3.16)$$

the ion heating is governed primarily by stimulated scattering. Such is the case when the IAT is excited far above the threshold, i.e., when

$$Rv_s \gg \sqrt{\frac{2}{9\pi}}\left(\frac{n_1\kappa T_e}{\tau_{1e}}+\frac{n_2\kappa T_e}{\tau_{2e}}\right)\frac{Z_1^2n_1+Z_2^2n_2}{Z_1n_1+Z_2n_2}. \quad (3.17)$$

Under the conditions adopted in our study, the threshold for ion-acoustic instability is considerably exceeded, so that inequality (3.16) holds automatically. Along with condition (3.17), we assume that the second term on the right-hand side of Eq. (3.14) is much smaller than the first term, i.e., that the energy gained by ions in their collisions with electrons is low in comparison with the energy transferred from waves to ions in the stimulated scattering process. The consistency of this assumption with the above assumption that the ion distribution is Maxwellian [see formula (3.2)] is ensured by the large factor m_α/m_e, which characterizes the ratio $\tau_{\alpha e}/\tau_{\alpha\alpha}$. Taking into account this circumstance and ignoring ion–electron collisions, we obtain from Eq. (3.14) the following equations for the temperatures of each of the ion species:

$$\frac{dT_1}{dt} = \frac{T_{i0}}{\tau_1^{(0)}}\frac{1+\dfrac{\tau_2^{(0)}n_1}{\tau_1^{(0)}n_2}}{\dfrac{T_2^2}{T_1^2}+\dfrac{\tau_2^{(0)}n_1}{\tau_1^{(0)}n_2}}+\frac{T_2-T_1}{\tau_{12}(T_1)}, \quad (3.18)$$

$$\frac{dT_2}{dt} = \frac{T_{i0}}{\tau_2^{(0)}}\frac{1+\dfrac{\tau_2^{(0)}n_1}{\tau_1^{(0)}n_2}}{1+\dfrac{\tau_2^{(0)}n_1}{\tau_1^{(0)}n_2}\dfrac{T_1^2}{T_2^2}}+\frac{T_1-T_2}{\tau_{21}(T_1)}. \quad (3.19)$$

Here, $\tau_1^{(0)} = \dfrac{\kappa T_{i0}}{ARv_s}\dfrac{n_1(Z_1^2n_1m_1+Z_2^2n_2m_2)}{Z_2^2n_2m_2}$,

$$\frac{\tau_2^{(0)}}{\tau_1^{(0)}} = \frac{Z_2^2n_2^2m_2}{Z_1^2n_1^2m_1}, \quad (3.20)$$

$T_{i0} = T_1(0) = T_2(0)$ is the initial ion temperature, and the effective time scales for energy transfer in ion–ion collisions are given by expression (3.10) and change with the temperature of ions of species 1 according to the law $T_1^{-3/2}$. The above equations for the ion temperatures will serve as the basis for describing turbulent ion heating.

4. ION HEATING

In studying ion heating, we first consider the simplest limiting case in which the energy exchange in collisions between ions of different species is negligible. This is indeed the case at the very beginning of the heating, because, in the problem as formulated, it is assumed that, in the initial heating stage, the temperatures of the ion species are the same. The effect of collisions on ion heating in the case in which the temperatures of the ion species are markedly different will be

considered in the next section. In the limiting case in question, Eqs. (3.18) and (3.19) reduce to

$$\frac{dT_1}{dt} = \frac{T_{i0}}{\tau_1^{(0)}}\frac{1+\dfrac{\tau_2^{(0)}n_1}{\tau_1^{(0)}n_2}}{\dfrac{T_2^2}{T_1^2}+\dfrac{\tau_2^{(0)}n_1}{\tau_1^{(0)}n_2}}, \quad (4.1)$$

$$\frac{dT_2}{dt} = \frac{T_{i0}}{\tau_2^{(0)}}\frac{T_2^2}{T_1^2}\frac{1+\dfrac{\tau_2^{(0)}n_1}{\tau_1^{(0)}n_2}}{\dfrac{T_2^2}{T_1^2}+\dfrac{\tau_2^{(0)}n_1}{\tau_1^{(0)}n_2}}. \quad (4.2)$$

From this, in particular, we obtain the following equation, which describes the ratio of the temperatures of two ion species in the case of purely turbulent heating:

$$\frac{dT_1}{dT_2} = \frac{\tau_2^{(0)}}{\tau_1^{(0)}}\frac{T_1^2}{T_2^2}. \quad (4.3)$$

Assuming that $T_1(0) = T_2(0) = T_{i0}$, we write the solution to Eq. (4.3) in the form

$$\frac{1}{T_1}-\frac{1}{T_{i0}} = \frac{\tau_2^{(0)}}{\tau_1^{(0)}}\left(\frac{1}{T_2}-\frac{1}{T_{i0}}\right). \quad (4.4)$$

At the very beginning of the heating, the temperatures of the ion species differ insignificantly from T_{i0}. Consequently, we can represent the ion temperatures as $T_1 = T_{i0} + \Delta T_1$ and $T_2 = T_{i0} + T_2$ to arrive at the relationship

$$\frac{\Delta T_1}{\Delta T_2} = \frac{\tau_2^{(0)}}{\tau_1^{(0)}}, \quad (4.5)$$

according to which the parameter $\tau_2^{(0)}/\tau_1^{(0)}$ defined in formula (3.20) describes the ratio of the rates at which the ion temperatures increase at the very beginning of the heating.

Solution (4.4) implies that the stage of strongly turbulent heating ($T_1 \gg T_{i0}$, $T_2 \gg T_{i0}$) begins when

$$\tau_2^{(0)} = \tau_1^{(0)} \equiv \tau_0, \quad (4.6)$$

in which case, according to Eq. (4.3), we have

$$T_1 = T_2 \equiv T. \quad (4.7)$$

Under condition (4.6), Eqs. (4.1) and (4.2) take the same form $dT/dt = T_{i0}/\tau_0$ and, accordingly, have the solution

$$T(t) = T_{i0}\left(1+\frac{t}{\tau_0}\right). \quad (4.8)$$

If condition (4.6) is not satisfied, then solution (4.4) imposes an upper limit on the increase in the temperature of one of the ion species. Specifically, for $\tau_2^{(0)} > \tau_1^{(0)}$, we rewrite solution (4.4) as

$$T_2 = T_{i0}\frac{T_1}{T_1(1-\tau_1^{(0)}/\tau_2^{(0)}) + T_{i0}\tau_1^{(0)}/\tau_2^{(0)}}, \quad (4.9)$$

to obtain the limitation

$$T_2 < \frac{T_{i0}}{1-\tau_1^{(0)}/\tau_2^{(0)}}, \quad (4.10)$$

which is valid for any positive values of T_1 and T_2 because solution (4.9) increases monotonically with T_1 and, as $T_1 \longrightarrow \infty$, it approaches the value given by the right-hand side of this limitation. Analogously, for $\tau_1^{(0)} > \tau_2^{(0)}$, we arrive at the limitation

$$T_1 < \frac{T_{i0}}{1-\tau_2^{(0)}/\tau_1^{(0)}}. \quad (4.11)$$

Hence, we have shown that, when condition (4.6) is not satisfied, the temperature of one of the ion components increases insignificantly. Figure 1 shows T_2/T_{i0} versus T_1/T_{i0} for three different values of the parameter $\tau_2^{(0)}/\tau_1^{(0)}$: 0.1, 1, and 10. The straight line refers to the case given by formulas (4.6) and (4.7). In this case, an increase in the temperatures of both ion species is limited only by the applicability conditions of Eqs. (4.1) and (4.2). The curve that is below the straight line refers

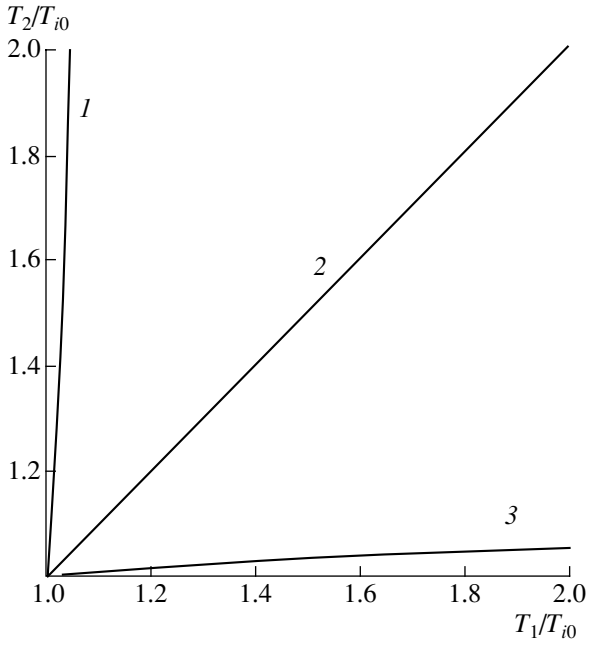

Fig. 1. Dependence of T_2/T_{i0} on T_1/T_{i0}, obtained from solution (4.9) for $\tau_2^{(0)}/\tau_1^{(0)}$ = (*1*) 0.1, (*2*) 1, and (*3*) 10.

to the case $\tau_2^{(0)} = 10\tau_1^{(0)}$, in which limitation (4.10) gives $T_2/T_{i0} < 10/9$. The curve that is above the straight line refers to the case $T_1/T_{i0} = 10/9$; in accordance with limitation (4.11), it asymptotically approaches the vertical line $\tau_2^{(0)}/\tau_1^{(0)} = 0.1$. It should be noted that Fig. 1 does not reflect the temporal behavior of the ion temperatures.

We now describe how the temperatures of the ion species change in time. For example, inserting solution (4.9) into Eq. (4.1), we obtain the following equation for $T_1(t)$:

$$\frac{dT_1}{dt} = \frac{T_{i0}}{\tau_1^{(0)}} \frac{1 + \dfrac{\tau_2^{(0)} n_1}{\tau_1^{(0)} n_2}}{\left[\dfrac{T_1}{T_{i0}}\left(1 - \dfrac{\tau_1^{(0)}}{\tau_2^{(0)}}\right) + \dfrac{\tau_1^{(0)}}{\tau_2^{(0)}}\right]^{-2} + \dfrac{\tau_2^{(0)} n_1}{\tau_1^{(0)} n_2}}. \quad (4.12)$$

Note that, since the right-hand side of Eq. (4.12) is positive, the temperature $T_1(t)$ increases monotonically over time. The solution to this equation can be represented as

$$\left(1 + \frac{\tau_2^{(0)} n_1}{\tau_1^{(0)} n_2}\right)\frac{t}{\tau_1^{(0)}} = \frac{\tau_2^{(0)} n_1}{\tau_1^{(0)} n_2}\left(\frac{T_1}{T_{i0}} - 1\right) + \frac{1}{1 - \tau_1^{(0)}/\tau_2^{(0)}}\left\{1 - \left[\frac{T_1}{T_{i0}}\left(1 - \frac{\tau_1^{(0)}}{\tau_2^{(0)}}\right) + \frac{\tau_1^{(0)}}{\tau_2^{(0)}}\right]^{-1}\right\}. \quad (4.13)$$

Solutions (4.9) and (4.13) provide an analytic description of the time evolutions of the ion temperatures.

Let us consider some limiting cases allowed by solutions (4.9) and (4.13). First, we consider the case given by the conditions

$$\frac{\tau_2^{(0)}}{\tau_1^{(0)}} \gg 1 > \frac{n_2}{n_1}, \quad (4.14)$$

which, with allowance for formula (3.20), are equivalent to

$$1 > \frac{n_2}{n_1} \gg \frac{Z_1 m_1^{1/2}}{Z_2 m_2^{1/2}}. \quad (4.15)$$

In this case, solution (4.13) can be approximately represented as

$$\frac{\tau_2^{(0)} n_1}{\tau_1^{(0)} n_2}\left(\frac{t}{\tau_1^{(0)}} + 1 - \frac{T_1}{T_{i0}}\right) \cong 1 - \frac{T_{i0}}{T_1}. \quad (4.16)$$

Since the right-hand side of this relationship is positive and is smaller than unity and since the left-hand side contains the large factor $\dfrac{\tau_2^{(0)} n_1}{\tau_1^{(0)} n_2} \gg 1$, solution (4.16) can be written in the form

$$T_1(t) \cong T_{i0}\left(1 + \frac{t}{\tau_1^{(0)}} - \frac{\tau_1^{(0)} n_2}{\tau_2^{(0)} n_1}\frac{t/\tau_1^{(0)}}{1 + t/\tau_1^{(0)}}\right) \cong T_{i0}\left(1 + \frac{t}{\tau_1^{(0)}}\right), \quad (4.17)$$

in which case solution (4.9) becomes

$$T_2(t) \cong T_{i0}\left[\left(1 - \frac{\tau_1^{(0)}}{\tau_2^{(0)}}\right) + \frac{\tau_1^{(0)}}{\tau_2^{(0)}}\left(1 + \frac{t}{\tau_1^{(0)}}\right)^{-1}\right]^{-1}. \quad (4.18)$$

Solution (4.18) describes slight changes in the temperature T_2 around the value T_{i0} on time scales of about $\tau_1^{(0)}$. We emphasize that the limiting value $T_2(\infty) \cong T_{i0}(1 + \tau_1^{(0)}/\tau_2^{(0)})$ differs from the initial temperature T_{i0} by the small amount $T_{i0}\tau_1^{(0)}/\tau_2^{(0)}$. This indicates that, under conditions (4.14), the heavier ion species is heated only slightly, whereas the temperature of the lighter ion species increases according to the law

$$T_1(t) \cong T_{i0}\left(1 + \frac{t}{\tau_1^{(0)}}\right) \quad (4.19)$$

until the heating process becomes dominated by collisions. In Fig. 1, this case corresponds to the lower curve.

The opposite limiting case is given by the conditions

$$\frac{\tau_2^{(0)}}{\tau_1^{(0)}} \ll \frac{n_2}{n_1} < 1, \quad (4.20)$$

which, with allowance for formula (3.20), are equivalent to

$$\frac{n_2}{n_1} \ll \frac{Z_1^2 m_1}{Z_2^2 m_2}. \quad (4.21)$$

In this case, from solution (4.13) we immediately obtain

$$T_1(t) \cong T_{i0}\left[1 - \frac{\tau_2^{(0)}}{\tau_1^{(0)}}\left(1 + \frac{t}{\tau_2^{(0)}}\right)^{-1}\right]\left(1 - \frac{\tau_2^{(0)}}{\tau_1^{(0)}}\right)^{-1}. \quad (4.22)$$

On time scales such that $t \gg \tau_2^{(0)}$, we have

$$T_1(t) \cong T_{i0}\left[1 + \frac{\tau_2^{(0)}}{\tau_1^{(0)}} - \frac{(\tau_2^{(0)})^2}{\tau_1^{(0)} t}\right]. \quad (4.23)$$

On the other hand, substituting solution (4.22) into Eq. (4.9) yields

$$T_2(t) \cong T_1(t)\left(1 + \frac{t}{\tau_2^{(0)}}\right). \quad (4.24)$$

Equation (4.22) describes slight changes in the temperature T_1 around the value T_{i0} on time scales of about $\tau_2^{(0)}$. At the same time, the temperature T_2 of the heavier ion species increases almost linearly according to law (4.24). In Fig. 1, this case corresponds to the upper curve: the heavier ions are rapidly heated to a considerable extent, whereas the temperature of the lighter ions remains essentially the same. This unusual situation, in which the heavier ions are heated faster than the lighter ions, is associated with the fact that the ratio of the probability of stimulated scattering by heavier ions to the probability of stimulated scattering by lighter ions increases as the density of the heavier ion species decreases, so that, when the number of heavier ions is sufficiently small, the wave energy is transferred predominantly to them. Note that, in this case, restriction (4.21) on the density of heavier ions is very stringent. Thus, for a fully ionized HO plasma, it yields $n_2/n_1 \ll 10^{-3}$.

Finally, for sufficiently large values of the parameter $Z_2^2 m_2/Z_1^2 m_1$, there exists a fairly wide range of values of the ratio $\tau_2^{(0)}/\tau_1^{(0)}$ that lies between ranges (4.14) and (4.20) and is determined by the inequalities

$$\frac{n_2}{n_1} \ll \frac{\tau_2^{(0)}}{\tau_1^{(0)}} \ll 1, \quad (4.25)$$

or, equivalently,

$$\frac{Z_1^2 m_1}{Z_2^2 m_2} \ll \frac{n_2}{n_1} \ll \left(\frac{Z_1^2 m_1}{Z_2^2 m_2}\right)^{1/2} \ll 1. \quad (4.26)$$

Under the condition

$$\frac{T_2^2}{T_1^2} \ll \frac{\tau_2^{(0)} n_1}{\tau_1^{(0)} n_2}, \quad (4.27)$$

the solution to Eqs. (4.1) and (4.2) in this parameter range has the form

$$T_1(t) = T_{i0}\left(1 + \frac{t}{\tau_1^{(0)}}\right), \quad (4.28)$$

$$T_2(t) = T_{i0}\left(1 - \frac{t}{\tau_2^{(0)}}\right)^{-1}. \quad (4.29)$$

At the initial instant, this solution satisfies condition (4.27). However, on time scales of $t \sim \tau_2^{(0)}$, solution (4.29) increases rapidly, so that condition (4.27) fails to hold. For $t \gg \tau_2^{(0)}$, the condition opposite to condition (4.27) is satisfied, in which case Eqs. (4.1) and (4.2) have the solution

$$T_1(t) \cong T_{i0}/\left(1 - \frac{\tau_2^{(0)}}{\tau_1^{(0)}}\right) \cong T_{i0}\left(1 + \frac{\tau_2^{(0)}}{\tau_1^{(0)}}\right), \quad (4.30)$$

$$T_2(t) \cong T_{i0}\frac{\tau_2^{(0)} n_1}{\tau_1^{(0)} n_2}\frac{(t - \tau_2^{(0)})}{\tau_2^{(0)}}. \quad (4.31)$$

Hence, under conditions (4.25), as well as under conditions (4.20), the heavier ions are heated faster than the lighter ones. For a fully ionized HO plasma, restriction (4.26) yields $10^{-3} \ll n_2/n_1 \ll 3 \times 10^{-2}$, which indicates that the density of heavier ions can be somewhat higher than that consistent with conditions (4.20).

5. ION HEATING DUE TO COLLISIONAL ENERGY EXCHANGE

Here, we consider the situation in which the energy redistribution during turbulent heating is dominated by collisional energy exchange between two ion species. As before, we assume that $m_2 \gg m_1$ and that the heavier ion species is present as an admixture; i.e., $n_1 \gg n_2$. According to expression (3.10), the latter assumption, in particular, yields the condition

$$\tau_{12} = \frac{n_1}{n_2}\tau_{21} \gg \tau_{21}. \quad (5.1)$$

This condition allows us to make the following two assumptions. First, the lighter ions are heated in the interaction with waves and their cooling by collisions with heavier ions proceeds at a comparatively slow rate. Second, heating of the heavier ions is basically governed by the energy transferred to them via collisions with lighter ions. Under these assumptions and under conditions (4.14), which imply that the heavier ion species is only slightly heated by turbulence, we can ignore the turbulent heating of the heavier ions in comparison with the energy transfer from the lighter ions. As a result, the heating of the heavier ions is described by the equation

$$\frac{dT_2}{dt} = \frac{T_1 - T_2}{\tau_{21}(T_1)}. \quad (5.2)$$

From Eq. (4.1) under conditions (4.14), we obtain the equation describing the heating of the lighter ions

$$\frac{dT_1}{dt} = \frac{T_{i0}}{\tau_1^{(0)}}. \quad (5.3)$$

In Eq. (5.3), we ignored collisions, and, in Eq. (5.2) for the heavier ions, we ignored turbulent heating. In order

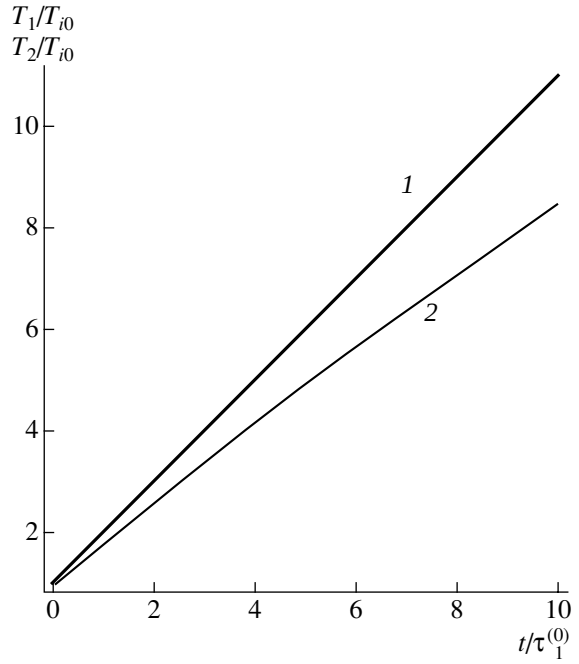

Fig. 2. Solution to Eqs. (5.2) and (5.3) for $\tau_{21}(T_{i0})/\tau_1^{(0)} = 0.1$. Curves *1* and *2* show the time dependences of T_1/T_{i0} and T_2/T_{i0}, respectively.

for these simplifications to be justified, it is necessary to satisfy the conditions

$$\frac{T_{i0}}{\tau_2^{(0)}}\frac{T_2^2}{T_1^2} \ll \frac{T_1 - T_2}{\tau_{21}(T_1)} \ll \frac{T_{i0}}{\tau_1^{(0)}}\frac{n_1}{n_2}, \tag{5.4}$$

which take the following form in terms of the explicit expressions for the effective collision times:

$$\begin{aligned} &\frac{Z_1^2 n_1 m_1}{Z_2^2 n_2 m_2}\frac{T_2^2}{T_1^2} \\ &\ll \frac{8\sqrt{2\pi}e_1^2 e_2^2 m_1^{1/2}\Lambda}{3(\kappa T_1)^{3/2} m_2}(T_1 - T_2)\frac{\kappa n_1 n_2}{AR v_s} \ll 1. \end{aligned} \tag{5.5}$$

By virtue of conditions (4.15), implying that the parameter $Z_1^2 n_1 m_1 / Z_2^2 n_2 m_2$ is small, the parameter range satisfying conditions (5.5) is fairly wide. The solution to Eq. (5.3) for the time evolution of the temperature of the lighter ions has the form (4.19). In accordance with Eq. (5.2), the temperature of the heavier ions is lower than the temperature of the lighter ions, but the greater the difference between the temperatures of the ion species, the higher the rate of heating of the heavier ions.

The temperature difference on time scales of $t < \tau_1^{(0)}$ can be deduced from Eqs. (5.2) and (5.3):

$$\begin{aligned} &T_1 - T_2 \\ &\cong \frac{T_{i0}\tau_{21}(T_{i0})}{\tau_1^{(0)}}\left[1 - \exp\left(-\frac{t}{\tau_{21}(T_{i0})}\right) + \frac{3t}{2\tau_1^{(0)}}\right]. \end{aligned} \tag{5.6}$$

We see that, on time scales of about $\tau_1^{(0)}$, the difference in the temperature of the two ion species is about $T_{i0}\tau_{21}(T_{i0})/\tau_1^{(0)}$. If the collisions are sufficiently frequent, then, on time scales of $\tau_1^{(0)} \gg \tau_{21}(T_{i0})$, the difference is much less than T_{i0}. On time scales much longer than $\tau_1^{(0)}$, the temperature of the lighter ions becomes much higher than its initial value, so that the effective collision time $\tau_{21}(T_1)$ increases [see expression (3.10)] and, according to Eq. (5.2), the heavier ions are heated at a progressively decreasing rate. Figure 2 illustrates how the temperatures of the lighter ions (curve *1*) and of the heavier ions (curve *2*) increase with time $t/\tau_1^{(0)}$. The time evolutions shown in the figure are solutions to Eqs. (5.2) and (5.3) for $\tau_{21}(T_{i0})/\tau_1^{(0)} = 0.1$. In accordance with solution (4.19), the temperature of the lighter ions increases linearly. As for the heavier ions, they are initially (on time scales of $t > \tau_{21}(T_{i0})$) heated at a rate very close to the rise in the temperature of the lighter ion species; however, as the lighter ions are heated further, the heating rate of the heavier ions becomes progressively slower. In this situation, the lighter ions are heated by turbulence, while the heavier ions are heated at the expense of collisional energy transfer from the lighter ions.

When condition (5.4) fails to hold, the ion heating should be described by general equations (3.18) and (3.19). One possible reason for the violation of condition (5.4) is a rapid increase in the ratio T_2/T_1 in the early (collisionless) heating stage. This possibility can be illustrated with an example of a fully ionized HO plasma, for which $\tau_2^{(0)}/\tau_1^{(0)} = 1024(n_2/n_1)^2$. Figure 3 illustrates how the temperatures of the lighter ions (curve *4*) and of the heavier ions (curves *1–3*, *5*) increase with time $t/\tau_1^{(0)}$. The time evolutions shown in the figure are solutions to Eqs. (3.18) and (3.19) for $\tau_{21}(T_{i0})/\tau_1^{(0)} = 0.01$ and $\tau_2^{(0)}/\tau_1^{(0)} = 1024(n_2/n_1)^2$ and for different values of the ratio n_2/n_1: 0.005, 0.01, 0.011, 0.03, and 0.1. The lowermost light curve is the time evolution $T_2(t)$ for $n_2/n_1 = 0.1$. In this case, we have $\tau_2^{(0)}/\tau_1^{(0)} \cong 10$; consequently, in accordance with conditions (4.14), the lighter ions are heated faster than the heavier ions and the heating process is similar to that illustrated in Fig. 2. For $n_2/n_1 = 0.03$, we have $\tau_2^{(0)} \cong \tau_1^{(0)}$,

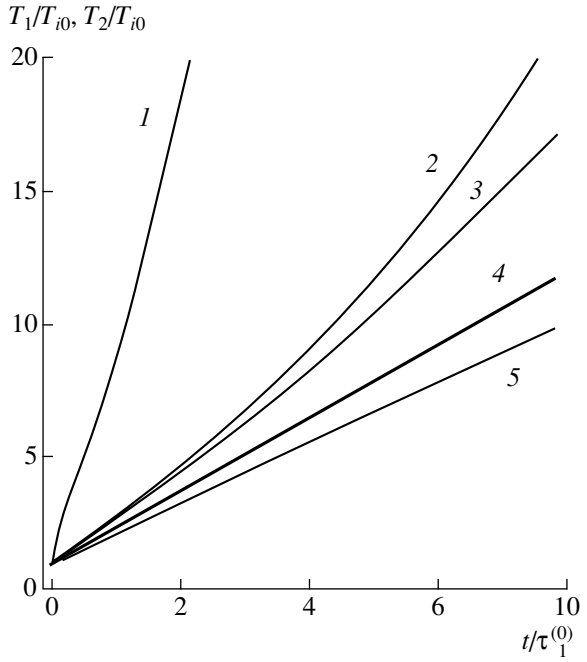

Fig. 3. Solution to Eqs. (3.18) and (3.19) for $\tau_{21}(T_{i0})/\tau_1^{(0)} = 0.01$ and $\tau_2^{(0)}/\tau_1^{(0)} = 1024(n_2/n_1)^2$ and for different values of the ratio n_2/n_1: (*1*) 0.005, (*2*) 0.01, (*3*) 0.011, (*4*) 0.03, and (*5*) 0.1. Curves *1–3* and *5* illustrate the dependence of T_2/T_{i0} on the time $t/\tau_1^{(0)}$, and curve *4* shows the same dependence of T_1/T_{i0}.

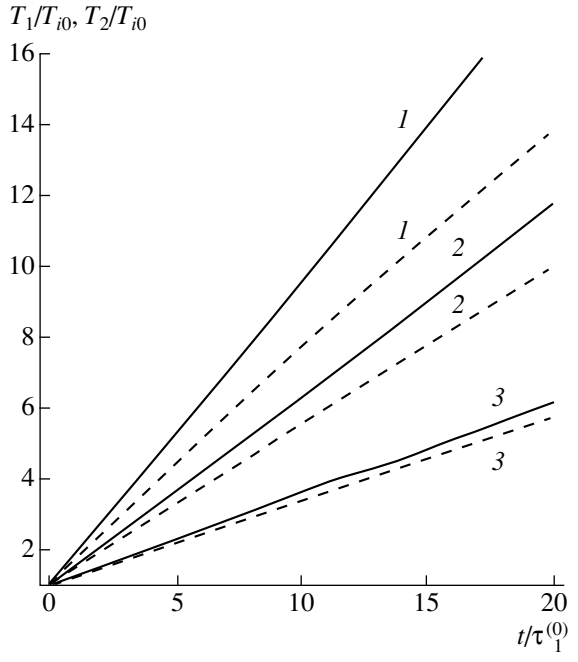

Fig. 4. Solution to Eqs. (3.18) and (3.19) for $\tau_{21}(T_{i0})/\tau_1^{(0)} = 0.1$ and $\tau_2^{(0)}/\tau_1^{(0)} = 1024(n_2/n_1)^2$ and for different values of the ratio n_2/n_1: (*1*) 0.2, (*2*) 1, and (*3*) 3. The solid curves illustrate the dependence of T_1/T_{i0} on the time $t/\tau_1^{(0)}$, and the dashed curves illustrate the same dependence of T_2/T_{i0}.

so that the time evolutions $T_2(t)$ and $T_1(t)$ coincide. The three lowest values of the density of the heavier ion species, $n_2/n_1 = 0.005$, 0.01, and 0.011, satisfy condition (4.25), under which the temperature of the heavier ions increases faster than that of the lighter ions. In Fig. 3, these densities refer to the three uppermost curves. It can be seen that, although collisions are fairly frequent, the temperature of the heavier ions can increase significantly faster than that of the lighter ions and, moreover, the heavier ions can be heated at a progressively increasing rate. In all these cases, the laws according to which the temperature of the lighter ions increases are almost linear and the heavy curve in Fig. 3 satisfies these laws to within 5%. Hence, in contrast to the case of collisionless heating, in which the temperature of the lighter ions approaches a constant value given by solution (4.30), we see that, under conditions (4.25), the energy transfer from the heavier ion species, rapidly heated by turbulence, can increase the rate of heating of the lighter ions, which, however, always remains slower than the heating rate of the heavier ion species.

Figure 4 illustrates how the temperatures of the lighter ions (solid curves) and the heavier ions (dashed curves) increase with time $t/\tau_1^{(0)}$ when the density of the heavier ions is not low. The three solid curves and the three dashed curves were obtained for $\tau_{21}(T_{i0})/\tau_1^{(0)} = 0.1$ and $\tau_2^{(0)}/\tau_1^{(0)} = 1024(n_2/n_1)^2$ and for different values of the ratio n_2/n_1: 0.2, 1, and 3 (from top to bottom). In each of the three cases, we can see that the lighter ions are hotter than the heavier ions and that the higher the density of the heavier ions, the slower the rates of heating of both ion species and the smaller the temperature difference between them at a given time. The lighter ions are heated according to a linear law. As for the heavier ions, they are heated at a progressively decreasing rate when $n_2/n_1 < 1$ and at a constant rate when their density is high. In the case illustrated in Fig. 4, as in that shown in Fig. 2, the lighter ions are heated in the interaction with waves, while the heating of the heavier ions is governed by collisional energy transfer from the lighter ions.

6. CONCLUSIONS

Having considered ion heating in a plasma with two ion species of different charge-to-mass ratio, we can formulate the following results. First, the ion species for which the parameter $Z_\alpha^2 n_\alpha^2 m_\alpha$ is smaller is heated at a faster rate. Second, under conditions in which collisions are unimportant, both of the ion species are

heated to a fairly large extent only when $Z_1^2 n_1^2 m_1 \sim Z_2^2 n_2^2 m_2$, in which case their temperatures increase at equal rates. When the parameter $Z_\alpha^2 n_\alpha^2 m_\alpha$ differs considerably between the two ion species, and when collisions are unimportant, only one of the species is heated substantially at a fast rate, while the temperature of the other species rapidly approaches a constant value that differs insignificantly from the initial temperature. Finally, taking into account energy exchange in collisions between ions of different species removes this limitation on the temperature of the ion species heated at a slower rate. In this case, if the masses of the ion species are significantly different, then the lighter ions are almost always heated at a constant rate, in which case, however, the temperature difference between the species can grow over time, in particular, at a progressively increasing rate.

As an example of a plasma system in which the conditions adopted in our study are satisfied, we consider the GOL-3 multi-mirror device [23, 24]. The parameters of HO plasmas in the previous and planned GOL-3 experiments are as follows: $T_e \sim 2$ keV, $T_e/T_i \sim 10^2$, $n_e \sim n_\mathrm{H} \sim 10^{15}$ cm^{-3}, and $n_0/n_\mathrm{H} \ll 1$. For our estimates, we assume that the plasma is fully ionized and that the oxygen concentration is comparatively low, $n_0/n_\mathrm{H} \sim 10^{-2}$. In the GOL-3 plasma, the electron temperature gradients are fairly large: in a certain small plasma region, they are as strong as 1 keV/40 cm, and, in a larger region, they are weaker (about 1 eV/cm). We also assume that $|\partial T/\partial z| \sim 1$ eV/cm; this value exceeds the threshold for IAT by a factor of about 50. The strong damping of the low-frequency mode is ensured by the condition $r_{D1}/r_{D2} \sim 0.8 < 1$. In turn, condition (2.4), under which the IAT spectrum can be described by formula (2.3), is satisfied by a large margin: its right-hand side is larger than the left-hand side by a factor of 10. In this case, the characteristic frequencies of turbulent heating of the ion species are equal to $(\tau_1^{(0)})^{-1} \cong 2.2 \times 10^6$ s^{-1} and $(\tau_2^{(0)})^{-1} \cong 2.2 \times 10^7$ s^{-1}, which indicate that oxygen ions are heated at a faster rate than hydrogen ions. Since the turbulent heating rates are low in comparison with the characteristic frequencies of collisions among ions of the same species, $(\tau_{11})^{-1} \cong 1.7 \times 10^7$ s^{-1} and $(\tau_{22})^{-1} \cong 1.0 \times 10^8$ s^{-1}, the bulk of the ions in the plasma obey Maxwellian distribution (3.2). The electron–ion energy exchange can be ignored because the terms in Eq. (3.14) that describe corresponding exchanges with lighter (hydrogen) ions and heavier (oxygen) ions are smaller than the term accounting for turbulent ion heating by a factor of 25 and of 100, respectively. In this case, the parameter characterizing the role of collisional energy exchange is approximately equal to $\tau_{21}/\tau_1^{(0)} \cong 3.2 \times 10^{-2}$, so that the ion heating is described by a dependence analogous to that given by curve *2* in Fig. 3. The above estimates show that the properties of turbulent ion heating that have been revealed in our study can be used to interpret the results of experiments similar to those in the GOL-3 device.

In conclusion, note that condition (2.4), which leads to formula (2.3) for the IAT spectrum, is not always satisfied in a plasma with two ion species of different charge-to-mass ratio. In such a situation, the IAT spectrum can no longer be described by formula (2.3) and the properties of turbulent plasma heating will generally differ from those revealed above (see [21] for details).

ACKNOWLEDGMENTS

This work was supported in part by the Russian Foundation for Basic Research (project no. 02-02-16047) and the Russian Federal Program for State Support of Leading Scientific Schools (project no. NSh-1385.2003.2).

REFERENCES

1. E. K. Zavoĭskiĭ and L. I. Rudakov, At. Energ. **23**, 417 (1967).
2. E. D. Volkov, N. F. Perepelkin, V. A. Suprunenko, and E. A. Sukhomlin, *Collective Phenomena in Current-Carrying Plasmas* (Naukova Dumka, Kiev, 1978).
3. B. B. Kadomtsev, in *Reviews of Plasma Physics*, Ed. by M. A. Leontovich (Atomizdat, Moscow, 1964; Consultants Bureau, New York, 1968), Vol. 4.
4. V. I. Petviashvili, Dokl. Akad. Nauk SSSR **153**, 1295 (1963) [Sov. Phys. Dokl. **8**, 1218 (1963)].
5. L. M. Kovrizhnykh, Zh. Éksp. Teor. Fiz. **48**, 1114 (1965) [Sov. Phys. JETP **21**, 744 (1965)].
6. L. I. Rudakov, Zh. Éksp. Teor. Fiz. **60**, 2134 (1971) [Sov. Phys. JETP **33**, 1148 (1971)].
7. A. S. Kingsep, Zh. Éksp. Teor. Fiz. **62**, 2179 (1972) [Sov. Phys. JETP **35**, 1139 (1972)].
8. V. Yu. Bychenkov, V. P. Silin, and S. A. Uryupin, Phys. Rep. **164**, 119 (1988).
9. V. Yu. Bychenkov, V. P. Silin, and S. A. Uryupin, Fiz. Plazmy **15**, 300 (1989) [Sov. J. Plasma Phys. **15**, 173 (1989)].
10. V. Yu. Bychenkov, V. N. Novikov, V. P. Silin, and S. A. Uryupin, Fiz. Plazmy **15**, 1456 (1989) [Sov. J. Plasma Phys. **15**, 847 (1989)].
11. V. P. Silin and S. A. Uryupin, Zh. Éksp. Teor. Fiz. **102**, 78 (1992) [Sov. Phys. JETP **75**, 41 (1992)].
12. I. Alexeff, W. D. Jones, and D. Montgomery, Phys. Rev. Lett. **19**, 422 (1967).
13. A. Hirose, I. Alexeff, and W. D. Jones, Phys. Fluids **13**, 1290 (1970).
14. B. D. Fried, R. B. White, and T. K. Samec, Phys. Fluids **14**, 2388 (1971).
15. L. L. Pasechnik and V. F. Semenyuk, Zh. Tekh. Fiz. **43**, 1071 (1973) [Sov. Phys. Tech. Phys. **18**, 676 (1973)].

16. I. M. A. Gledhill and M. A. Hellberg, J. Plasma Phys. **36**, 75 (1986).
17. H. X. Vu, J. M. Wallace, and B. Bezzerides, Phys. Plasmas **1**, 3542 (1994).
18. E. A. Williams, R. L. Berger, R. P. Drake, *et al.*, Phys. Plasmas **2**, 129 (1995).
19. I. V. Kuzora, V. P. Silin, and S. A. Uryupin, Phys. Lett. A **258**, 329 (1999).
20. I. V. Kuzora, V. P. Silin, and S. A. Uryupin, Zh. Éksp. Teor. Fiz. **120**, 1194 (2001) [JETP **93**, 1035 (2001)].
21. I. V. Kuzora, V. P. Silin, and S. A. Uryupin, Kratk. Soobshch. Fiz., No. 3, 32 (2003).
22. V. P. Silin, *Introduction to Kinetic Gas Theory* (Nauka, Moscow, 1971).
23. A. V. Burdakov, V. Weinzettl, V. Piffl, and S. V. Polosatkin, in *Proceedings of the 30th Conference on Plasma Physics and Controlled Thermonuclear Fusion, Zvenigorod, 2003*, MC2-16.
24. V. T. Astrelin, A. V. Burdakov, and V. V. Postupaev, Fiz. Plazmy **24**, 450 (1998) [Plasma Phys. Rep. **24**, 414 (1998)].

Translated by O.E. Khadin

Plasma Physics Reports, Vol. 30, No. 4, 2004, pp. 318–329. Translated from Fizika Plazmy, Vol. 30, No. 4, 2004, pp. 349–360.

PLASMA DYNAMICS

Experiments with Small-Size Dynamic Loads in the S-300 High-Power Pulsed Generator

Yu. L. Bakshaev*, A. V. Bartov*, P. I. Blinov*, S. A. Dan'ko*, Yu. G. Kalinin*, A. S. Kingsep*, I. V. Kovalenko, A. I. Lobanov**, V. I. Mizhiritskiĭ*, V. P. Smirnov*, A. S. Chernenko*, and K. V. Chukbar***

** Russian Research Centre Kurchatov Institute, pl. Kurchatova 1, Moscow, 123182 Russia*

*** Moscow Institute for Physics and Technology, Institutskiĭ per. 9, Dolgoprudnyĭ, 141700 Russia*

Received February 20, 2003; in final form, July 27, 2003

Abstract—Results are presented from experimental studies of promising output units for high-current pulsed generators within the framework of the program on inertial confinement fusion research with the use of fast Z-pinches. The experiments were carried out on the S-300 facility (4 MA, 70 ns, 0.15 Ω). Specifically, sharpening systems similar to plasma flow switches but operating in a nanosecond range were investigated. Switching rates to a load as high as 2.5 MA per 2.5 ns, stable switching of a 750-kA current to a low-size Z-pinch, and the radiative temperature of the load cavity wall of up to 50 eV were achieved. © *2004 MAIK "Nauka/Interperiodica".*

1. INTRODUCTION

One of the most promising research trends in designing high-power pulsed sources of soft X-ray (SXR) emission for inertial confinement fusion, as well as in studying the properties of materials under the destractive action of high-power radiation, is based on using pulsed current generators of megaampere (and, in the near future, multimegaampere) range. In these experiments, an imploding Z-pinch with a characteristic lifetime on the order of a few tens of nanoseconds is used as a load. This enables SXR pulses with a power of several hundred terawatts to be generated [1]. In particular, experiments are performed with cylindrical arrays (liners) in the form of a squirrel cage made of micron-diameter wires.

The radial implosion of a liner whose mass is initially distributed over a cylindrical surface of radius r and length l is accompanied by the heating of the liner material and conversion of the magnetic energy into thermal radiation, which is emitted within an extremely short time interval. Such experiments are presently being carried out in a number of large facilities, including the Angara-5-1 [2] and S-300 [3] facilities (Russia), the MAGPIE facility [4] (Great Britain), and the world's largest Z facility [1] (the United States). At the Z facility (with a current of ~20 MA), the generation of an SXR burst with a duration of several nanoseconds and total energy of about 1.8 MJ has been achieved. Such parameters open up the possibility of carrying out experiments with hohlraum targets at energies close to those required for thermonuclear ignition. Unfortunately, in this scheme for the conversion of magnetic energy into X radiation, the latter is emitted into a 4π solid angle and occupies the entire (relatively large) volume of the liner unit. This circumstance significantly reduces the energy density stored in this unit and, consequently, the equivalent radiative temperature.

It is because of this feature that the heating of a target to the temperature needed for the initiation of thermonuclear reaction requires the creation of super-high-power pulsed generators with a current pulse amplitude of 50–60 MA and a duration of 100–150 ns. However, the physics of the above processes can be studied even now with present-day generators operating at lower currents and stored energies. In particular, in experiments on the implosion of a liner with a relatively low mass, a maximum velocity of $V_{max} \sim 10^8$ cm/s, which is required for the efficient generation of thermal radiation, can in principle be achieved. It is also possible to study the formation of a current-carrying cylindrical plasma shell, i.e., to model the initial stage of the processes that will occur in future, higher power facilities. The increase in the intensity of the radiation flux onto the target in a cavity can be achieved by decreasing the cavity size, i.e., the cavity volume and the surface area of the reradiating wall. This obviously requires decreasing the initial liner radius r from which the liner mass is accelerated toward the axis. Since the energy needed for the liner mass acceleration should be deposited in a time $\tau \sim r/V_{max}$, the decrease in the liner radius means that the current pulse must be significantly sharpened.

In this study, we present the results of experiments carried out with small-size loads on the S-300 facility (see [5]) at the Russian Research Centre Kurchatov Institute and the results of numerical simulations of the output unit of a high-current generator. We also consider questions related to diagnostic problems.

1063-780X/04/3004-0318$26.00 © 2004 MAIK "Nauka/Interperiodica"

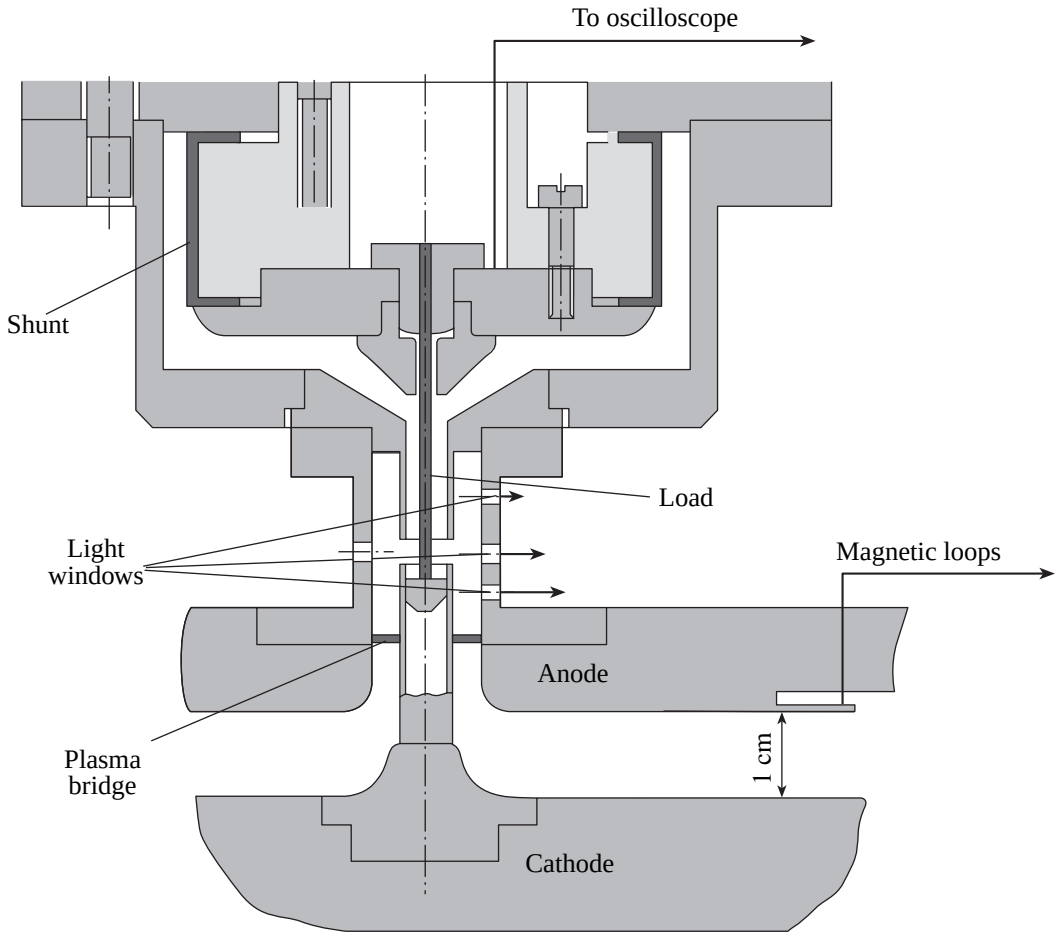

Fig. 1. Schematic of the output unit with a small-size plasma flow switch and a load.

2. EXPERIMENTAL DESIGN AND RESULTS

Figure 1 shows an output unit designed for experiments with small-size cylindrical liners ($r \approx 1$ mm, $l \approx 10$ mm) on the S-300 facility with a concentrator based on a system of vacuum transmission lines. The generator produces a current pulse with an amplitude of 2.5–3 MA and a rise time of $T_{pulse} \sim 70$ ns through an inductive load with $L \sim 10$ nH. A cylindrical load (the liner or a metal wire substitute) is placed at the axis of a cavity whose side wall is a metal tube with an inner radius of 1.7–2.0 mm and a length of 10 mm. One load end is connected to the end of the inner cylinder of the coaxial feeder, which, in turn, is connected to the generator cathode. Another load end is connected to the generator anode through a cylindrical resistor (noninductive shunt) measuring the current, the side wall of the cavity, and the outer cylinder of the coaxial feeder. The shunt, which is made from 8- to 25-μm constantan foil, provides time resolution of $\Delta\tau \sim 1$–2 ns. The foil is chosen to be thick enough for it not to be destroyed during the current pulse; in our experiments, the foil thickness happened to be on the order of the skin depth. (Operation of a shunt with a thickness close or larger than the skin depth is described in the Appendix.) The computation results show that, during the current pulse, variations in the shunt signal caused by the foil heating are less than 10%. Between the cavity end and the end of the cathode cylinder, there was a gap, the length of which was varied from 1 to 2.6 mm. The total current flowing through the disc line (the anode–cathode in Fig. 1) was monitored by averaging and integrating signals from eight dI_{in}/dt detectors arranged over a circle of radius ~5 cm (see Fig. 1).

To sharpen the current pulse to a few nanoseconds, we used a switch with an accelerated current-carrying plasma bridge. A similar system operating in a microsecond range is called the plasma flow switch. Up to now, it was used in regimes with an input-current rise time of several microseconds and allowed one to obtain current pulses with an amplitude on the order of 10^7 A and a rise time of 500–600 ns, whereas, in our case, the characteristic times were on the order of a few nanoseconds. At given pulse parameters, the material, size, and other characteristics of the object from which the plasma bridge is produced should be chosen experi-

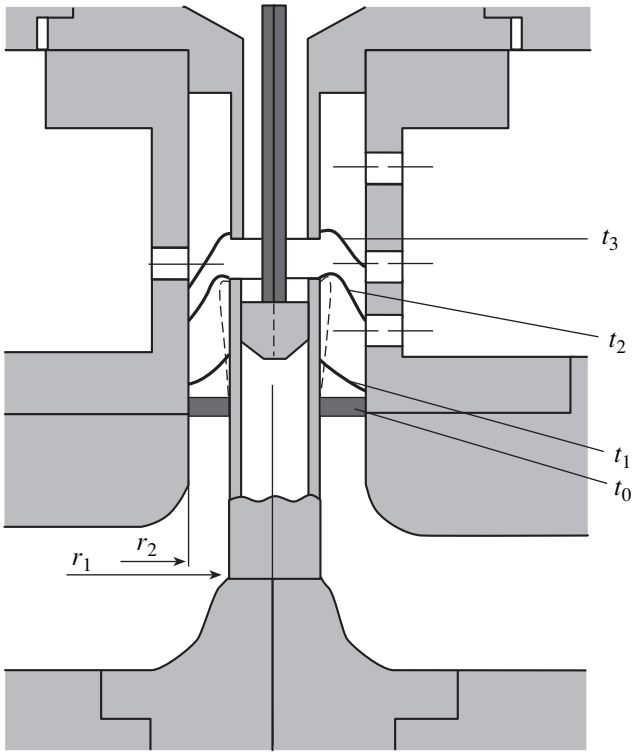

Fig. 2. Central part of the output unit.

mentally to enable a regime of intense radiative plasma cooling, otherwise the gap will be bridged by a plasma cloud and, consequently, the current will not be switched to the load.

In our experiments, the plasma bridge was created by the electric breakdown and subsequent ionization of a polymer film (in some experiments, coated with a thin metal layer) placed in the annular gap of the feeding line, $r_1 < r < r_2$ (see Fig. 2). The pulse voltage in the open circuit can increase over a time of $T_{\text{pulse}} \sim 70$ ns to $U \sim 1$ MV, which significantly exceeds the breakdown voltage. Hence, the breakdown and ionization of the film occur at the very beginning of the pulse, and then almost the entire current flows through the bridge, which begins to be accelerated along the coaxial line under the action of the ponderomotive force $\frac{1}{c}\mathbf{j} \times \mathbf{B}$. Taking into account that $B \propto 1/r$ and the corresponding magnetic pressure P_B is proportional to $1/r^2$, we can estimate the acceleration of the plasma, assuming that the film is uniform and the magnetic field does not penetrate to the rear surface of the plasma bridge: $a \approx P_B/\rho\delta$, where ρ is the plasma density and δ is the thickness of the plasma bridge. Accordingly, the axial displacement of the plasma bridge should depend on the radius as $1/r^2$. In other words, the plasma bridge will bend. The bridge positions at successive instants of time t_0, t_1, t_2, and t_3 are shown in Fig. 2. Near the electrode surface, the bridge acceleration should decrease because of the formation of a boundary layer consisting of dense plasma produced due to the evaporation and ionization of the electrode material. A counteracting process is the thinning of the bridge due to the plasma being pushed away from the surface of the inner cylinder. This can even result in the detachment of the plasma bridge from the wall and the formation of an erosion plasma opening switch in the gap. This picture of bridge motion follows from a qualitative consideration and rough analytical estimates. To consider the dynamics of this type of plasma flow switch in more detail, we performed numerical simulations, the results of which are presented in Section 3.

When the current-carrying plasma bridge crosses the gap between the ends of the inner coaxial cylinders (in the time interval between the instants t_2 and t_3; see Fig. 2), the load is incorporated the current circuit (i.e., the magnetic flux penetrates into the load cavity). The characteristic duration of such a commutation can be estimated as the effective length of the switching region (the width of the end gap + the thickness of the current-carrying sheet in the bridge) divided by the current sheet velocity near the surface of the cathode cylinder. In our experiments on the implosion of liners with an initial radius of ~1 mm, it was necessary to sharpen the leading edge of the current pulse to a few nanoseconds; for this purpose, the plasma bridge should be accelerated to velocities higher than 5×10^7–10^8 cm/s.

The plasma bridge was first produced from a 5- to 10-μm aluminum foil. Then, in order to decrease the mass of the accelerated bridge, 2- to 5-μm polymer Mylar films were used, along with nitrocellulose films having a thickness less than 1 μm, and others. The uniformity of the film breakdown was qualitatively estimated by the uniformity of the discharge glow in frame images recorded with an image tube. The images were taken from the top (see Fig. 1) in the absence of the shunt unit. The velocity with which the plasma bridge moved along the inner electrode was determined by taking streak images of the discharge glow through ~1-mm-diameter holes made in the sidewall of the outer cylinder along the cylinder generatrix (see Fig. 1). One such streak image is shown in Fig. 3.

The highest experimentally observed velocity of the plasma bridge was about 10^8 cm/s. This velocity was achieved with a 1.5-μm annular plastic washer coated with a thin Al layer. The best results were achieved when the Al coating was deposited from the generator side. In the first experiments, 0.5- to 2-mm-diameter metal wires in a 4-mm-diameter tube were used to imitate the liner; in this case, the load inductance (including the shunt) was ~2–3 nH. The shunt signals were used to detect the switching of a significant fraction of the current to the load. The characteristic rise time of the load current ranged from 2.5 to 10 ns in different experiments. The duration of the current pulse through the load varied from 7 to 20 ns, depending on the length

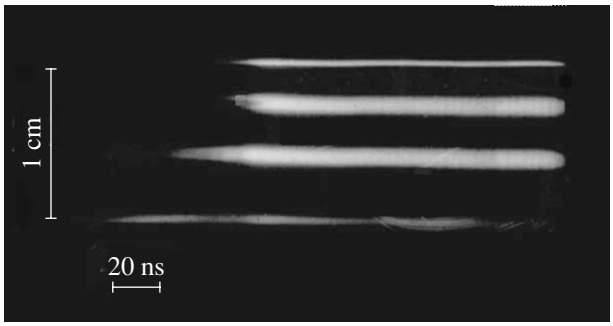

Fig. 3. Visible-light streak image of the plasma bridge motion. The image of the cylinder sidewall is projected onto the streak camera slit. The lower strip corresponds to the initial position of the plasma bridge.

of the gap between the ends of the coaxial line (the longest duration was observed for gap lengths of 1.6–1.8 mm). The pulse duration was evidently determined by the amount of the bridge plasma entering the load cavity through the gap, as well as by the gap breakdown. In some experiments, we recorded current pulses through the load with an amplitude of up to 2.5 MA and a rise time of about 2.5 ns (see Fig. 4, curve *1*). Figure 4 also shows the waveform of the total current that increases to ~3 MA in 70 ns (curve *2*). Thus, a 25-fold sharpening of the leading edge of the current pulse and an increase in the current growth rate to $dI_L/dt \sim 10^{15}$ A/s were achieved for the first time in these experiments. These results, however, are poorly reproducible. It seems that they are close to the limiting characteristics of the switch and can be achieved only for a certain optimum combination of the experimental parameters. In most of the experiments, the current growth rate was $dI_L/dt \sim (1–3) \times 10^{14}$ A/s, which is sufficient for studying the formation of a current-carrying plasma shell and the generation of SXR emission.

To form a plasma bridge with a sharper boundary, we used double washers made of two 1.5-μm Mylar films spaced by a distance of 1–2 mm. In this case, the second film acts as a barrier and explodes after the first film strikes it. In addition, to prevent the premature detachment of the bridge from the inner electrode of the coaxial line (before the bridge reaches the end of the coaxial line) and the subsequent plasma erosion, as happens in ordinary plasma opening switches, we sometimes used a tapered inner electrode (shown by the dashed line in Fig. 2), whose diameter increased in the propagation direction of the bridge. The corresponding waveforms are shown in Fig. 5. Here, curve *4* shows the shunt signal indicating the switching of the current to the load. The signal of pulsed SXR emission from the switch is shown by curve *5*. The first spike in this signal corresponds to the instant of collision between the first film and the barrier (the second film), while the second spike corresponds approximately to the instant at which the current is switched to the load. The fact that the second spike occurs somewhat before the current is switched to the load can be attributed to the aforementioned process of plasma erosion, during which both the plasma bridge resistance and the voltage between the switch electrodes sharply increase. In this particular experiment, the current through the load reached ~750 kA and the switching time was about 5 ns. In contrast to the case with the maximum switching rate (Fig. 4), the current through the load reached its amplitude value over a time that was significantly longer than the switching time.

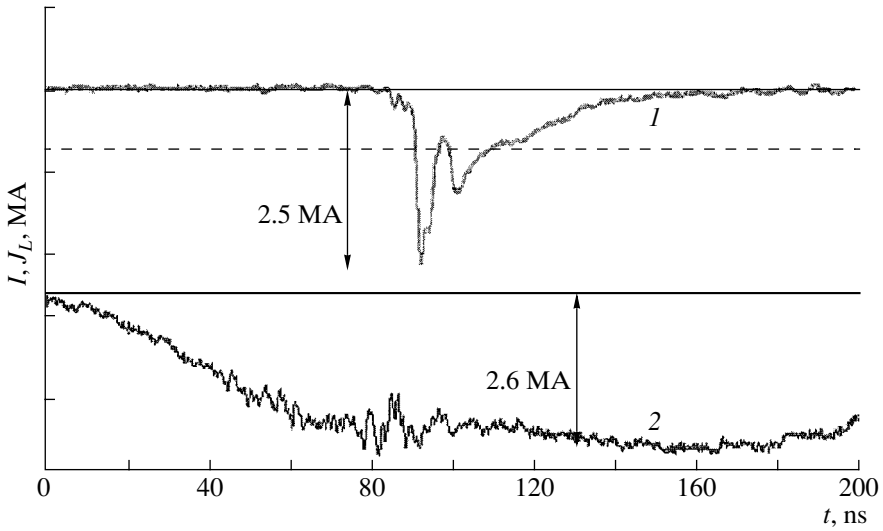

Fig. 4. Waveforms corresponding to the rapid switching of the current to the load: (*1*) current through the load I_L and (*2*) input current I.

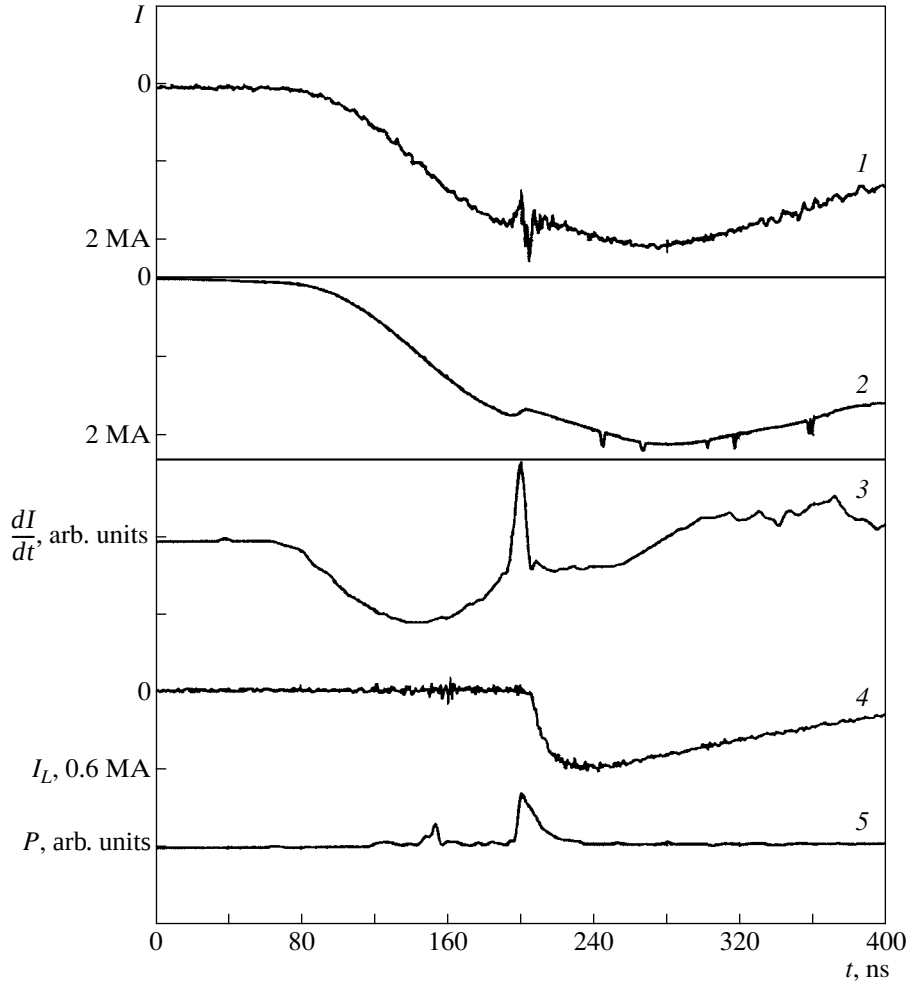

Fig. 5. Commutation of the current to the load with the help of a double plasma bridge and a conical inner electrode: (*1*) total current I obtained by the analog integration of the signal from diagnostic loops, (*2*) total current I obtained by the numerical integration, (*3*) dI/dt signal, (*4*) the current I_L through the load, and (*5*) SXR signal P from the current commutation region.

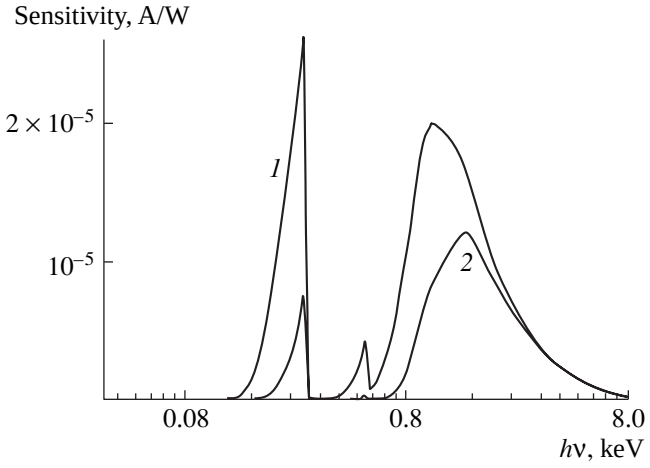

Fig. 6. Sensitivity of an XRD with a Ni cathode and Mylar filters with surface mass densities of (*1*) 0.36 and (*2*) 0.67 mg/cm^2.

In experiments on liner implosion, arrays consisting of eight to sixteen tungsten wires with diameters of 5–6 μm arranged in the form of a squirrel cage with a radius of ~1 mm were used as loads. The arrays were placed on the axis of a metal tube with an inner diameter of 3.8–4.0 mm. The length of the liner was 10 mm. In addition to monitoring the electric signals, we also measured the pulsed X-ray emission with photon energies of $h\nu \geq 50$ eV. The measurements were carried out with the help of two vacuum X-ray diodes (XRDs) equipped with Ni cathodes and Mylar filters with a surface mass density of 0.34 or 0.67 mg/cm^2. The XRD sensitivity curves are shown in Fig. 6. No special calibration of the diodes was performed, and their sensitivity was calculated using the literature data to within a factor of 2.

We present the results of our X-ray measurements below. In some experiments with liners consisting of sixteen tungsten wires arranged over a 2-mm-diameter

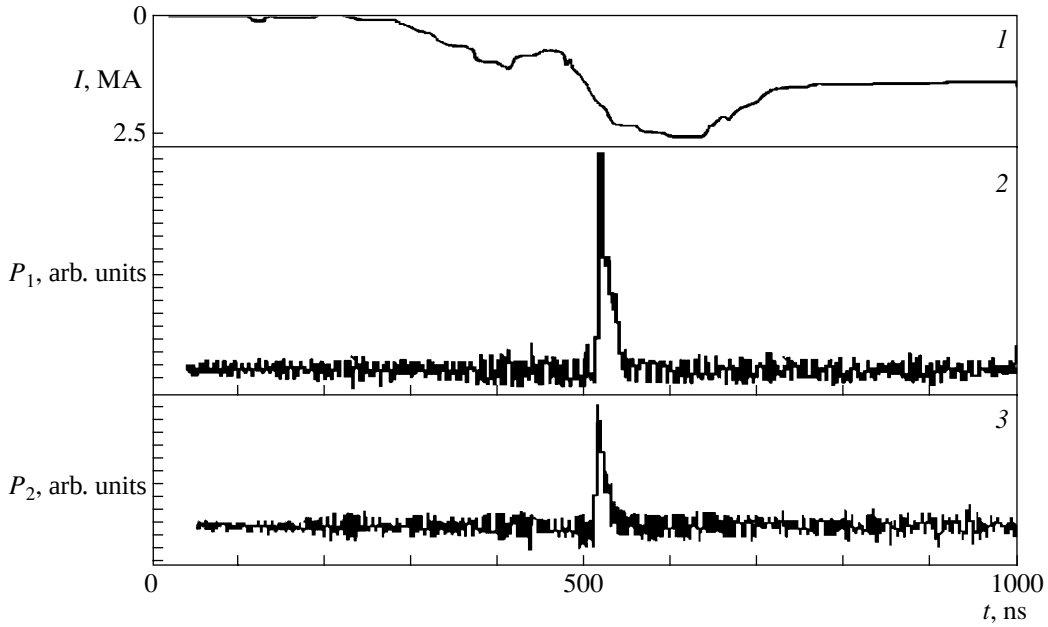

Fig. 7. Waveforms of (*1*) the output current and (*2*, *3*) the XRD signals P_1 and P_2 from detectors equipped with Mylar filters: (*2*) 0.36 mg/cm^2 (reduction factor of 1 : 20) and (*3*) 0.67 mg/cm^2 (reduction factor of 1 : 10).

cylindrical surface, the measurements were performed through a 2-mm-diameter hole in the top end of the load cavity. The detectors were set on the liner axis at a distance of 1.1 m from the hole. Figure 7 shows, as an example, two signals with durations of about 10 ns. The radiative temperature was estimated from the ratio between the signals from two XRDs under the assumption of a Planckian emission spectrum. Estimates show that the radiative temperature was $T \cong 140$ eV, the emitted energy was $E_{h\nu} \approx 20$ J, and the area of the emissive surface was on the order of 2×10^{-5} cm^2.

The above interpretation of the results of X-ray measurements is somewhat ambiguous. This is related to the possible presence of hot spots near the liner axis in the final stage of the Z-pinch implosion and the presence of regions with different temperatures in the liner plasma. We believe it would be more informative and unambiguous to measure the radiative temperature of the inner surface of the load cavity. This surface is heated by both the liner emission and the electric current.

We carried out a series of experiments in which XRDs monitored the inner surface of the cavity through a 1-mm-diameter hole made in the cavity wall (Fig. 8). The loads were the same as in the previous experiments. The lines of sight of the detectors were oriented so that the liner wires did not fall within the detectors' field of view. The XRDs were placed at a distance of $L = 2.3$ m from the liner axis. The effective area of the hole was 0.5 mm^2. In these experiments, signals observed from behind a 0.36-mg/cm^2 filter corresponded to a wall temperature of 38–48 eV, assuming that the emission spectrum from the hole followed the blackbody spectrum.

3. NUMERICAL SIMULATIONS OF A FAST PLASMA FLOW SWITCH

3.1. Mathematical Model

A system consisting of two rigid coaxial electrodes is connected to a pulsed current generator. The inter-

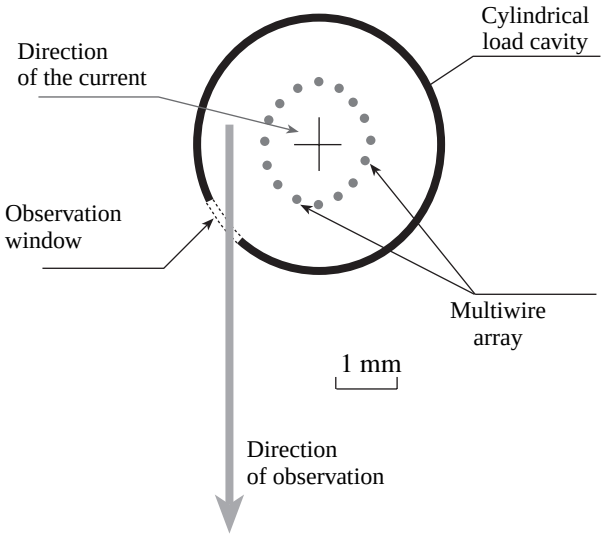

Fig. 8. Schematic of the measurements of X-ray emission from the load cavity.

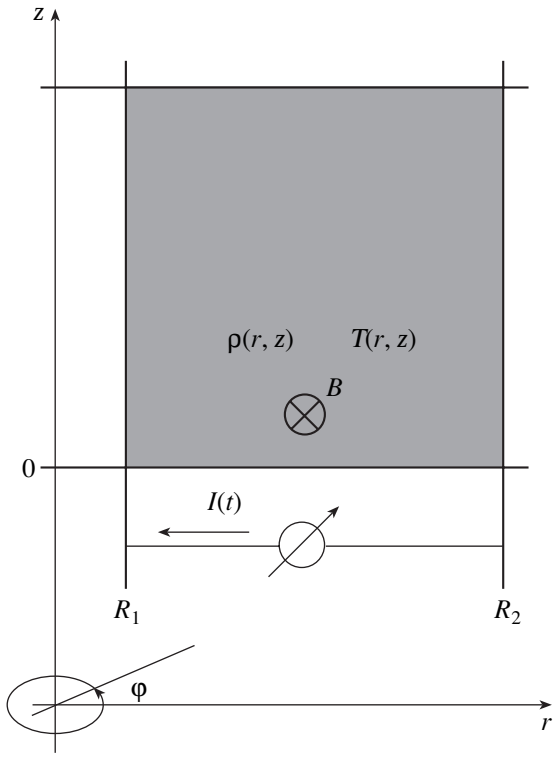

Fig. 9. The model of the plasma flow switch.

electrode space ($R_1 < r < R_2$, $0 < z < Z$) is occupied with a plasma (Fig. 9). It is assumed that, at the initial instant ($t = 0$), the electron temperature T_e is equal to the ion temperature T_i, the plasma is at rest, and the specific mass density ρ of the plasma is constant throughout the entire plasma volume. The electrodes are assumed to be at a zero temperature. The magnetic field at the electrode walls and the upper boundary of the plasma is set at zero: $B(R_1) = B(R_2) = B(Z) = 0$. At the lower plasma–vacuum interface ($z = 0$), the magnetic field is related to the total current in the external electrical circuit by the following relationship, written in dimensionless units (see below):

$$B_\varphi = \frac{0.2I(t)}{r},$$

where $I = I_0 \sin\frac{\pi t}{2T_{\text{pulse}}}$ is the current in the external circuit, T_{pulse} is the current rise time, and r is the distance from the system axis. The motion of a two-temperature plasma in a magnetic field is described by the magnetohydrodynamic (MHD) equations [6–8] with allowance for radiative heat transfer. It is assumed that the magnetic field induction $\mathbf{B}$ has only the φ component: $\mathbf{B} = B_\varphi \mathbf{e}_4$. The evolution of the magnetic field in plasma is described by the equations of electron magnetohydrodynamics (EMHD) [9]

$$\mathbf{E} = -\frac{1}{c}\mathbf{v}\times\mathbf{B} + \frac{1}{nec}\mathbf{j}\times\mathbf{B} + \frac{\mathbf{j}}{\sigma} - \frac{1}{ne}\nabla(nT_e) + \frac{1}{ne}\mathbf{R}, \quad (1)$$

$$\mathbf{R} = -\frac{3}{2}n\frac{\omega_{Be}\tau_e}{1+(\omega_{Be}\tau_e)^2}\mathbf{b}\times\nabla T_e, \quad \mathbf{b} = \frac{\mathbf{B}}{|\mathbf{B}|}, \quad (2)$$

$$\mathbf{j} = \sigma\mathbf{E} = \frac{c}{4\pi}\nabla\times\mathbf{B}, \quad (3)$$

$$\frac{\partial\mathbf{B}}{\partial t} = -c\nabla\times\mathbf{E}, \quad (4)$$

$$\frac{3}{2}n\left[\frac{\partial T_e}{\partial t} + \left(\left(\mathbf{v} - \frac{\mathbf{j}}{ne}\right)\nabla\right)T_e\right] + nT_e\nabla\cdot\left(\mathbf{v} - \frac{\mathbf{j}}{ne}\right) = -\nabla\cdot\mathbf{q} + Q_e, \quad (5)$$

$$\mathbf{q} = -nT_e\left[\frac{3}{2}\frac{\omega_{Be}\tau_e}{1+(\omega_{Be}\tau_e)^2}\mathbf{b}\times\frac{\mathbf{j}}{ne} + \frac{4.66}{1+(\omega_{Be}\tau_e)^2}\frac{\sigma}{ne^2}\nabla T_e + \frac{5}{2}\frac{\omega_{Be}\tau_e}{1+(\omega_{Be}\tau_e)^2}\frac{\sigma}{ne^2}\mathbf{b}\times\nabla T_e\right], \quad (6)$$

$$Q_e = \frac{\mathbf{j}\cdot\mathbf{j}}{\sigma} + \frac{\mathbf{j}}{ne}\cdot\mathbf{R}, \quad (7)$$

where n is the electron density, T_e is the electron temperature (in energy units), and σ is the plasma conductivity. The difference between the ion and electron velocities is taken into account by introducing the electron current velocity $\mathbf{j}/ne$ into Eq. (5).

We note that in the problem under study, the initial characteristic scale length is by one order of magnitude higher than c/ω_{pi}, so that it could be expected that the EMHD effects would be of minor importance. However, the results of numerical simulations show that this is not the case. The simulation results obtained in the EMHD and MHD approximations turn out to be quite different, which is related to the emergence of space scales significantly smaller than the initial one over the course of MHD evolution, especially near the electrodes.

The above set of equations was solved numerically using a conservative difference scheme on a curvilinear variable mesh constructed by the integro-interpolation method with the splitting of the physical processes [10].

The set of equations (1)–(4) was solved with respect to the magnetic field inductance B_φ. We note that, after excluding the current density by means of Eq. (3), this set becomes nonlinear with respect to B_φ. The calculations were performed by an inexplicit scheme with intermediate iterations over nonlinearity on the current time layer. In the region occupied by the plasma, a reg-

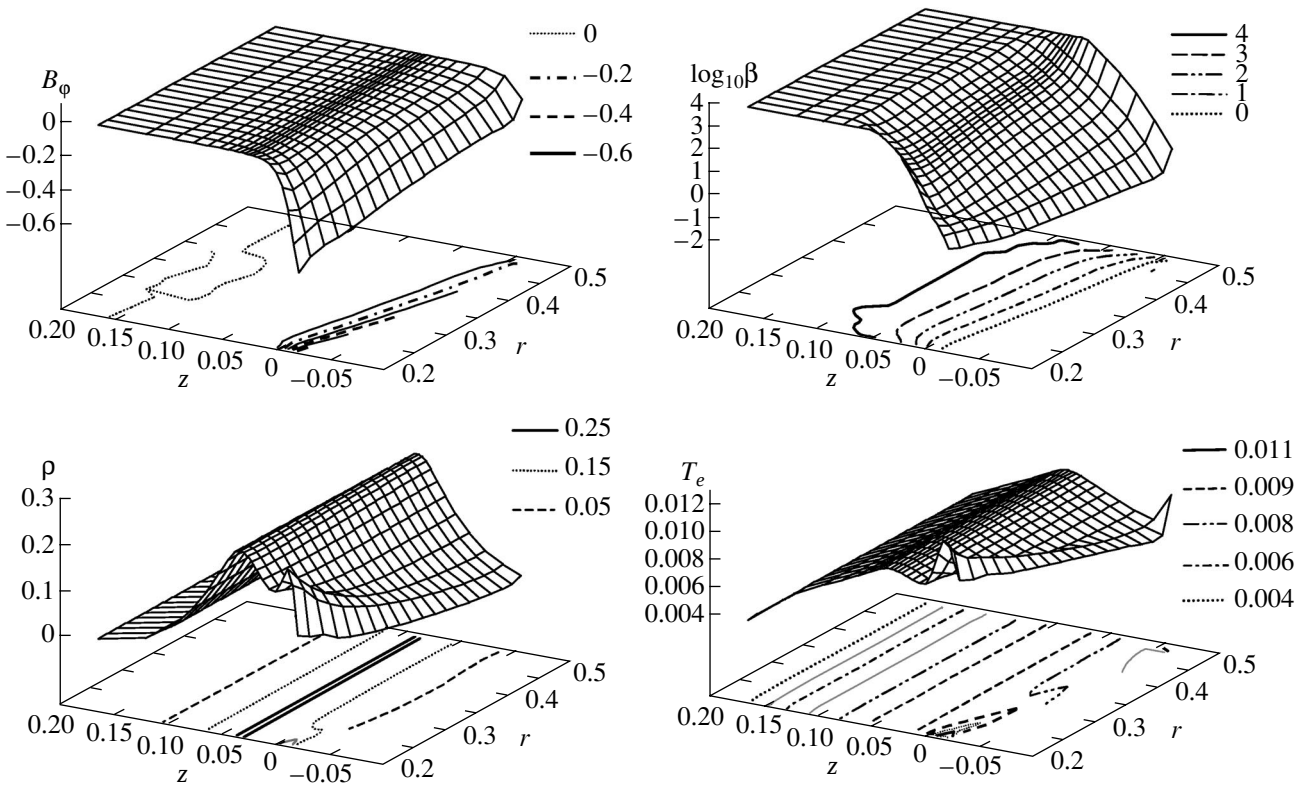

Fig. 10. Distributions of the magnetic field induction B_φ, the mass density ρ, the electron temperature T_e, and the logarithm of the parameter β at $t = 20$ ns. The mesh is composed of 20×20 Lagrange cells.

ular Lagrange mesh was defined. To diminish the deformation of Lagrange cells in the course of computation, the mesh nodes were rearranged using an optimizing procedure with the subsequent conservative recalculation onto a new mesh. The algorithm for the mesh optimization was based on the method described in [11]. The procedure was applied after a preset number of time steps or when a "reversed" cell occurred at the current time step. In the latter case, the time step was decreased.

In numerical simulations, we used dimensionless variables normalized to the following characteristic scales: 100 ns for time, 1 cm for length, 1 mg/cm^3 for the mass density, 1 keV for the temperature, 1 MA for the current, and 1 MG for the magnetic induction.

3.2. Simulation Results

The numerical simulations were performed for different parameters of the plasma and the current pulse in the external circuit. The typical results presented below correspond to the following parameters: $R_1 = 0.2$ cm, $R_2 = 0.5$ cm, $T_{\text{pulse}} = 100$ ns, pulse amplitude $I_0 = 2.5$ MA, Hall parameter $\omega_{Be}\tau_e = 0.1$, $\rho = 0.3$ mg/cm^3, and the initial temperatures $T_e = T_i = 10$ eV. As in the experiment, the outer electrode acted as an anode. The plasma material was pure carbon. The computational results are shown in Figs. 10–12. The dimensionless parameter β (the ratio of the plasma pressure to the magnetic pressure) is shown within a range covering four orders of magnitude.

Under the above initial conditions, plasma is originally in the MHD regime. After the start of the current pulse, the field starts to diffuse into the plasma from the lower boundary of the switch (see Fig. 9). Simultaneously, the plasma expands into a vacuum. This expansion is accompanied by a decrease in the temperature to 5 eV. Near the electrodes, the expansion rate is lower than that in the interelectrode gap because, in the latter, the temperatures of the plasma components decrease more rapidly. At the very beginning of the process (at $t < 10$ ns), the applicability range of EMHD corresponds to a thin layer near the lower boundary; hence, the role of the EMHD terms in Eq. (1) is insignificant. In this stage, a correction to the magnetic field due to the thermoelectronic shift in the electrode regions at the plasma–vacuum interface is about 10 G, which is much lower than the field variations caused by resistive diffusion. Due to the imposed boundary conditions, the electron current density is higher at the lower boundary, near the electrodes. It is maximal near the cathode, where a significant local Joule heating of electrons occurs.

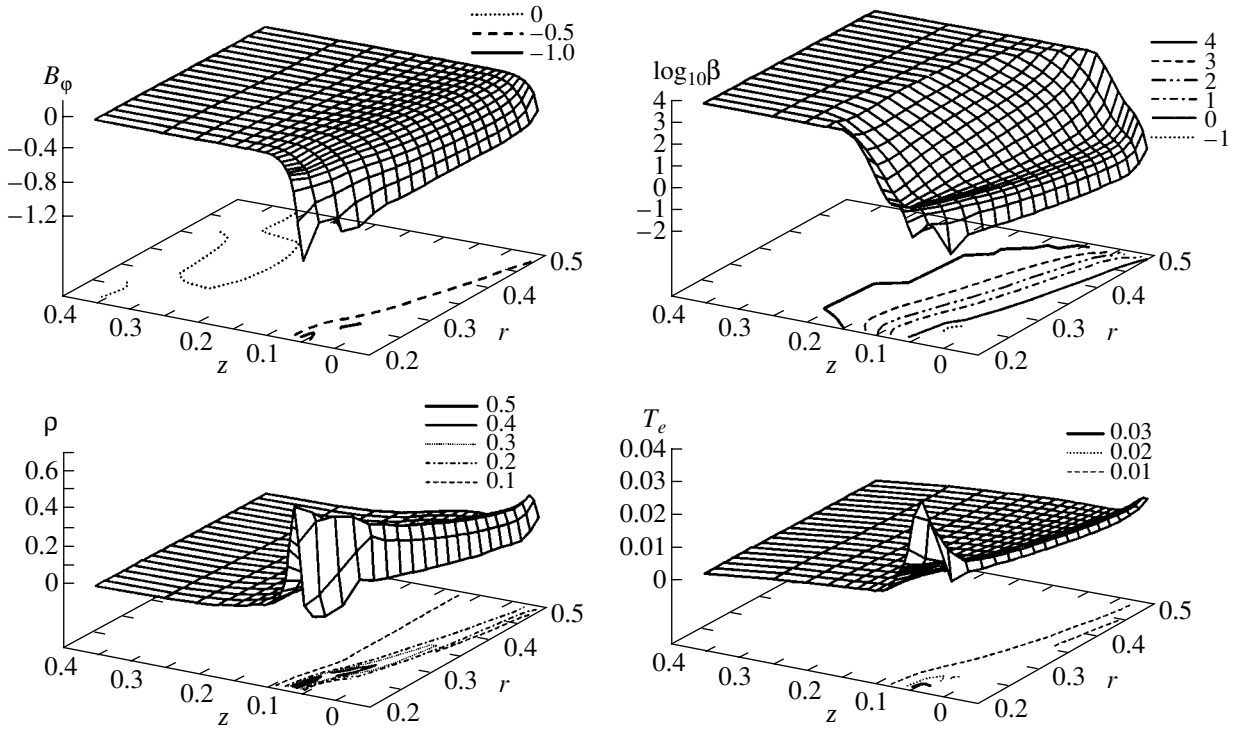

Fig. 11. Distributions of the magnetic field induction B_φ, the mass density ρ, the electron temperature T_e, and the logarithm of the parameter β at $t = 40$ ns. The mesh is composed of 20×20 Lagrange cells.

By the time $t = 10$ ns, the magnetic and plasma pressures near the anode are equal to each other, after which a shock wave (SW) is formed. At $t = 20$ ns (see Fig. 10), a "snow plow" is being formed behind the SW front. The ions are heated to a temperature of 11–12 eV; the electrons, to 7–10 eV. The temperatures are maximum at the plasma–vacuum interface, near the anode: $T_e \cong 12$ eV and $T_i \cong 32$ eV. The velocity of the free boundary reaches 6.8×10^6 cm/s.

By the time $t = 30$ ns, the velocity of the boundary reaches 1.2×10^7 cm/s, and the temperatures reach $T_e \cong 29$ eV and $T_i \cong 100$ eV. By this time, the plasma boundary has traveled a distance of 0.3 cm.

By the 40th nanosecond (Fig. 11), the role of the density and electron temperature variations near the inner electrode significantly increases and the EMHD effects come into play. At this time, the electron and ion temperatures near the inner electrode are $T_e \cong 38$ eV and $T_i \cong 715$ eV, and the substance is fully ionized. Calculations show that a low-density toroidal "bubble" is formed near the anode. This bubble is initially adjacent to the SW and exists until the end of the calculation. Inside the bubble, the field has local maxima and minima; this corresponds to the formation of current loops. The bubble volume increases with time, while its density decreases. The maximum magnetic field at the lower boundary is 1.86 MG, and it is 0.8 MG inside the bubble. The plasma density reaches its maximum value of 0.38 mg/cm^3 at the SW front, and the maximum velocity of the free boundary is 1.6×10^7 cm/s. By this time, the plasma boundary has traveled a distance of 0.65 cm.

By the time $t = 60$ ns (Fig. 12), the ion temperature reaches its maximum value of 3 keV near the anode at the lower plasma boundary. The rapid deformation of the Lagrange cells is then observed at the lower boundary of the bubble, the velocity of the mesh nodes being as great as 7×10^8 cm/s. It thus becomes necessary to recalculate the mesh at each time step. As a result, we had to terminate our computations at $t = 62$ ns.

Numerical simulations carried out with finer meshes (up to 100 Lagrange cells in each direction) also demonstrate the formation of bubbles near the anode (and in certain versions, near the cathode as well). Due to a significant deformation of the Lagrange cells, the computation time in this case was limited by 40–47 ns. When the radial variations in the plasma density and/or the temperatures of the plasma components are taken into account, the plasma dynamics exhibits EMHD features. These results will be presented in a separate paper.

A characteristic feature of the process under study (in both the MHD and EMHD models) is the high sensitivity of the plasma bridge to the initial conditions. Thus, varying the initial temperature from 7 eV (a situation similar to that discussed above) to 5 eV leads to a significant modification of the plasma dynamics. By the

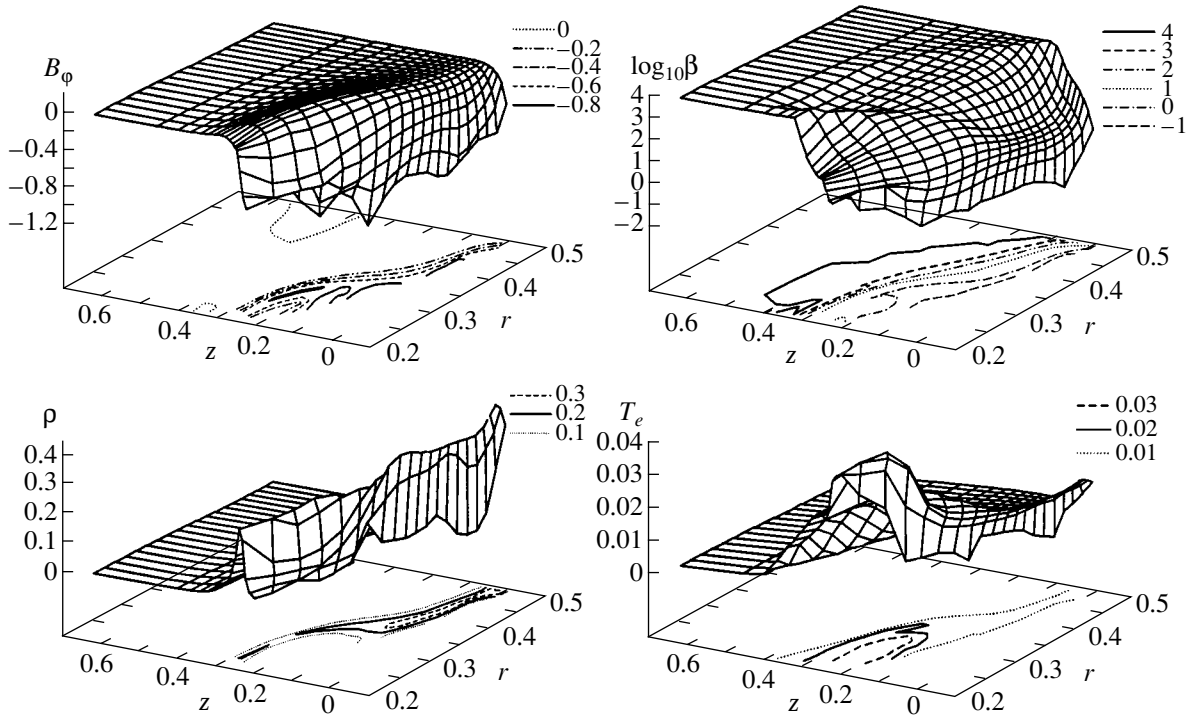

Fig. 12. Distributions of the magnetic field induction B_φ, the mass density ρ, the electron temperature T_e, and the logarithm of the parameter β at $t = 60$ ns. The mesh is composed of 20×20 Lagrange cells.

40th nanosecond, the radial plasma velocity becomes higher than the axial (twice as high by the end of the calculation), and a vortex emerges in the electrode region. In our opinion, the further evolution of this vortex can result in a transition from a hydrodynamic regime to a regime in which the space charge plays a significant role on a characteristic spatial scale of c/ω_{pe}. The latter regime corresponds to the final stage of erosion switch operation. Perhaps it is the high sensitivity to the initial conditions that is responsible for the poor reproducibility of the extreme regimes of the current commutation to the load.

An important computational result is the rapid increase in the perturbation at the inner electrode. It was due to this circumstance that we had to employ a cascade experimental scheme.

4. CONCLUSIONS

The results of experiments performed in the S-300 high-current pulsed generator with imploding wire arrays placed inside a closed cavity provide a good basis for future experiments with hohlraum targets in present-day facilities. The output units operating on the principle of a plasma flow switch that were employed in our experiments were shown to be capable of operating in a nanosecond range. In some experiments, a switching rate to the load as high as 2.5 MA per 2.5 ns was achieved. Using a cascade scheme enables stable operation regimes with a switching rate of up to 750 kA per 5 ns. The radiative temperature of the cavity wall was 40–50 eV.

Two-dimensional numerical simulations of a plasma flow switch were performed using a two-component magnetohydrodynamic model with allowance for radiative heat transfer. The first stage of the output unit operation (up to the switching instant) was numerically investigated in more detail.

ACKNOWLEDGMENTS

We are grateful to R.V. Chikin and V.A. Shchagin for their help in experiments and S.F. Medovshchikov and S.L. Nedoseev for manufacturing the wire arrays. This study was supported by the RF Ministry of Atomic Energy; the RF Ministry of Industry, Science, and Technologies (under the Unique Installations Program); the Russian Federal Program for the State Support of Leading Scientific Schools (grant no. 00-15-96599); and the Russian Foundation for Basic Research (project nos. 01-02-17359 and 01-01-00401).

APPENDIX

Let us solve the time-dependent problem of determining the current flowing through a thin-walled hollow cylinder from the electric-field measurements at the inner surface of the cylinder with allowance for the

skin effect. It is well known that almost all the inverse problems refer to the class of ill-posed problems. In the case at hand, the problem is, in essence, ill-posed because of the exponential decay of a high-frequency electromagnetic field in a conductor (with the decay rate increasing without bound as the current frequency increases). Since only weak echoes of the corresponding harmonics reach the inner surface of the cylinder, even small errors in their determination can lead to a significant discrepancy between the calculated and true current values. The methods for overcoming the ill-posedness consist in abandoning physically unreliable information and reconstructing only the smooth (on the characteristic skin-time scale) current components.

The skinning of an electromagnetic field in a homogeneous metal cylinder with a conductivity σ is described by conventional diffusion equations. For an axially symmetric distribution of the current flowing along the cylinder, all the quantities depend on the radius only and the problem becomes one-dimensional. We may also exploit the fact that the thickness of the cylinder wall δ is small compared to its outer radius. Hence, the set of equations for the azimuthal magnetic field and axial electric field can be reduced to a case of plane geometry with the x axis directed inward along the radius (in this case, the inaccuracy will be on the order of $\delta/R \ll 1$; note that the exact solution presents no difficulties except for some rather cumbersome algebra):

$$\frac{\partial B}{\partial t} = \frac{c^2}{4\pi\sigma}\frac{\partial^2 B}{\partial x^2}, \quad E = -\frac{c}{4\pi\sigma}\frac{\partial B}{\partial x}.$$

Obvious boundary conditions for this set of equations are $B|_{x=0} = 2I(t)/cR$ and $B|_{x=\delta} = 0$, whereas the initial condition is $B|_{t=0} = 0$. Upon solving this set of equations, we obtain the relation between $B|_{x=0} \Leftrightarrow I(t)$ and $\partial B/\partial x|_{x=\delta} \Leftrightarrow E_{\text{in}}$.

The simplest way to find the distribution of the skinned magnetic field in the cylinder is to apply the Laplace transformation in time: $B(x, t) \longrightarrow B_p(x)$. Simple calculations result in the relationship

$$-\left.\frac{dB_p}{dx}\right|_{x=\delta} = \frac{\sqrt{p/D}}{\sinh(\sqrt{p/D}\delta)}B_p|_{x=0}, \quad D = \frac{c^2}{4\pi\sigma}.$$

The inverse transformation relates the measured electric field and the total current via a convolution integral over time. However, it is very problematical to directly use this relation, because the Laplace transform of the function $\sinh(\sqrt{p/D}\delta)/\sqrt{p/D}$, with which $E_{\text{in}}(t)$ is to be convoluted, has a singularity at the point $t = 0$ (the Laplace transform increases without bound as $p \longrightarrow \infty$, whereas even for a Dirac delta function, it tends to a finite value). This is a mathematical manifestation of the claimed ill-posedness.

To recover the smooth components (harmonics) of the current that are slightly skinned over the wall thickness δ, one can expand the function $\sinh(\sqrt{p/D}\delta)/\sqrt{p/D}$ into a series in the small parameter $\sqrt{p/D}\delta$ and keep the first three terms:

$$\frac{\sinh(\sqrt{p/D}\delta)}{\sqrt{p/D}} \cong \delta\left[1 + \frac{1}{3!}\frac{p\delta^2}{D} + \frac{1}{5!}\left(\frac{p\delta^2}{D}\right)^2\right].$$

The first of these terms corresponds to the absence of skinning, the second is the required correction, and the third serves to verify the accuracy of the model (it should be small compared to the second term, although it is reasonable to take it into consideration near the extrema of $I(t)$). It can be seen that, due to the rapid decrease in the coefficients by the expansion terms, the series is well convergent even when the skin effect plays an important role (the decay factor over the wall thickness δ is on the order of unity).

Taking into account the relationship $p_n \Leftrightarrow (d/dt)^n$, which is valid at zero initial conditions, we finally obtain

$$I(t) \cong C\left[V + \frac{1}{6}\frac{4\pi\sigma\delta^2}{c^2}\dot{V} + \frac{1}{120}\left(\frac{4\pi\sigma\delta^2}{c^2}\right)^2\ddot{V}\right],$$

where $V(t)$ is the signal from the detector placed at the inner surface of the cylinder and C is the scaling factor (for example, if one measures the voltage between two electrodes separated by the distance l along the system axis, this factor is equal to $2\pi\delta\sigma R/l$). The ill-posedness manifests itself in this formula as an increased sensitivity to high-frequency harmonics. This sensitivity stems from the series expansion in the derivatives of successively increasing order; however, operating with smoothed dependences $V(t)$ causes no problems.

The same formula is obtained if one uses the time hierarchy in the explicit form in ordinary space, representing the solution to the initial diffusion equation with the same boundary conditions in the form of a series $B(x, t) = B_0 + B_1 + \ldots$, whose terms are obtained from the chain relationships

$$D\frac{\partial^2 B_0}{\partial x^2} = 0, \quad D\frac{\partial^2 B_1}{\partial x^2} = \frac{\partial B_0}{\partial t}, \quad \text{etc.}$$

Accordingly, there is no need to consider questions about the relation between the convergence in the space of ordinary functions and their Laplace transforms. When the time derivatives of $V(t)$ are not too large, the formula proposed correctly describes (both qualitatively and quantitatively) such important consequences of the skin effect as the signal delay and the damping of the peaks of $I(t)$, while simultaneously offering a simple means of maintaining the proper accuracy.

REFERENCES

1. C. Deeney, M. R. Douglas, R. B. Spielman, *et al.*, Phys. Rev. Lett. **81**, 4883 (1998); J. P. Quintenz, P. F. Peterson,

J. S. DeGroot, and R. R. Peterson, in *Proceedings of the 13th International Conference on High Power Beams, Nagaoka, 2000*, p. 309.

2. V. V. Alexandrov, E. A. Azizov, A. V. Branitsky, *et al.*, in *Proceedings of the 13th International Conference on High Power Beams, Nagaoka, 2000*, p. 147.
3. Yu. G. Kalinin, P. I. Blinov, A. S. Chernenko, *et al.*, in *Proceedings of the 13th International Conference on High Power Beams, Nagaoka, 2000*, p. 76.
4. S. V. Lebedev, F. N. Beg, S. N. Bland, *et al.*, Rev. Sci. Instrum. **72**, 671 (2001).
5. A. Chernenko, Yu. Gorbulin, Yu. Kalinin, *et al.*, in *Proceedings of the 11th International Conference on High-Power Particle Beams, Prague, 1996*, p. 154.
6. A. S. Kingsep, V. E. Karpov, A. I. Lobanov, *et al.*, Fiz. Plazmy **28**, 319 (2002) [Plasma Phys. Rep. **28**, 286 (2002)].
7. A. S. Kingsep, V. I. Kosarev, A. I. Lobanov, and A. A. Sevast'yanov, Fiz. Plazmy **23**, 953 (1997) [Plasma Phys. Rep. **23**, 879 (1997)].
8. Yu. G. Kalinin, A. S. Kingsep, V. I. Kosarev, and A. I. Lobanov, Mat. Model. **12** (11), 63 (2000).
9. A. S. Kingsep, K. V. Chukbar, and V. V. Yan'kov, in *Reviews of Plasma Physics*, Ed. by V. V. Kadomtsev (Énergoizdat, Moscow, 1987; Consultants Bureau, New York, 1990), Vol. 16.
10. A. A. Samarskiĭ and Yu. P. Popov, *Difference Methods for Solving Gas-Dynamic Problems* (Nauka, Moscow, 1980).
11. P. Knupp, L. Margolin, and M. Shashkov, J. Comput. Phys., No. 176, 93 (2002).

Translated by N.N. Ustinovskiĭ

Plasma Physics Reports, Vol. 30, No. 4, 2004, pp. 330–337. Translated from Fizika Plazmy, Vol. 30, No. 4, 2004, pp. 361–368.

PLASMA INSTABILITY

MHD Plasma Stability in Alternative Toroidal Systems and the Local Dispersion Relation

A. A. Skovoroda

Nuclear Fusion Institute, Russian Research Centre Kurchatov Institute, pl. Kurchatova 1, Moscow, Russia

Received July 29, 2003

Abstract—The local dispersion relation obtained for an inhomogeneous anisotropic high-pressure plasma in the Chew–Goldberger–Low approximation is used to qualitatively study small-scale MHD plasma instabilities in alternative magnetic configurations in which the plasma compressibility plays a significant stabilizing role. It is established that it is important to satisfy the Bernstein–Kadomtsev condition in order to reduce the growth rate of the quasi-flute oscillations. Moderate plasma anisotropy is shown not to have a substantial destabilizing effect on the MHD plasma stability under the Bernstein–Kadomtsev condition in alternative systems. The situation in which the electron compressibility vanishes while the ion compressibility is nonzero is discussed; it is shown that, in this situation, the Bernstein–Kadomtsev condition becomes more stringent as the longitudinal wavenumber increases. © *2004 MAIK "Nauka/Interperiodica".*

1. INTRODUCTION

At present, there is increased interest in magnetic systems for confining hot plasmas in weak magnetic fields (at high β values). Much of this interest stems from advanced ideas about the improvement of magnetic confinement by optimizing the magnetic field geometry and by modifying the schemes for MHD plasma stabilization [1]. The objective of the present paper is to analyze the MHD stability of plasmas in *alternative* toroidal systems such as small-aspect-ratio tokamaks, stellarators, and systems with closed magnetic field lines [2–4]. These plasma confinement devices were chosen for analysis because they share a common property—the significant stabilizing effect of plasma compression, on which the present-day modification of MHD plasma stabilization schemes has been based. Technologically, the key element in this modification is a toroidal magnetic divertor, which ensures that the magnetic separatrix exhibits a field null. A peculiar feature of the alternative configurations under discussion is that the magnetic field in them is strongly rippled along the field lines. Therefore, one of the goals of the present work is to investigate how the stabilization by compressibility is affected by the nonisothermal nature of the plasma and its anisotropy, as well as by high β values.

To analyze the stability of different MHD modes in magnetic confinement systems is a complicated task and, as a rule, requires numerical simulations. It turns out, however, that a fundamental physical picture of the stability of ideal modes can be derived from analysis of a comparatively simple local dispersion relation. This analysis also shows that the natural oscillations of a homogeneous plasma and unstable MHD modes that arise in an inhomogeneous plasma are mutually coupled to one another [5].

It is simplest to derive the local dispersion relation for the local modes of a plasma cylinder at $\beta \ll 1$ [1]. Recall that the derivation consists of the following steps. The key point is to obtain an expression for the perturbed plasma pressure $\tilde{p}$ in terms of only the radial displacement ξ_r. In the one-fluid approximation, the continuity equation and the adiabatic equation yield $\tilde{p} = -\xi_r p' - \gamma_0 p \nabla \cdot \boldsymbol{\xi}$, where $\boldsymbol{\xi}$ is the plasma displacement vector, γ_0 is the adiabatic exponent, and the prime denotes the derivative with respect to the radius r. The equation of plasma motion along the magnetic field lines gives $\nabla \cdot \boldsymbol{\xi} = [\omega^2/(\omega^2 - k_\parallel^2 c_s^2)]\nabla \cdot \boldsymbol{\xi}_\perp$, where $\boldsymbol{\xi}_\perp$ is the displacement vector transverse to the magnetic field, ω is the oscillation frequency, $k_\parallel = (k_z B_z + mB_\varphi/r)/B$ is the longitudinal wavenumber, B is the absolute value of the magnetic field, $B_{z,\varphi}$ are the magnetic field components, m is the azimuthal mode number, k_z is the wavenumber along the cylinder axis, $c_s = \sqrt{\gamma_0 p/\rho}$ is the speed of sound, and ρ is the plasma mass density. Assuming that β is low and using the definition of the drift velocity $\mathbf{V}_E$ in the electric field of the wave, $d\boldsymbol{\xi}_\perp/dt = \mathbf{V}_E$, we obtain $\nabla \cdot \boldsymbol{\xi}_\perp = 2\xi_r/R$, where $R = rB^2/B_\varphi^2$ is the radius of curvature of the magnetic field line (for details, see, e.g., [6], Section 4). The result is $\tilde{p} = -\xi_r(p' + 2\gamma_0 p\omega^2/R(\omega^2 - k_\parallel^2 c_s^2))$. Substituting this expression into the equation for small MHD oscilla-

1063-780X/04/3004-0330$26.00 © 2004 MAIK "Nauka/Interperiodica"

tions yields the following local dispersion relation for small-scale modes [1, 5]:

$$\omega^2 = k_\parallel^2 V_A^2 + \frac{2k_b^2}{k_\perp^2 R^2}\left(\frac{p'R}{\rho} + \frac{2\omega^2 c_s^2}{\omega^2 - c_s^2 k_\parallel^2}\right), \quad (1)$$

where $V_A = \sqrt{B^2/\rho}$ is the Alfvén speed, the wavenumber in the direction of the binormal is denoted as $k_b = (-k_z B_\varphi + mB_z/r)/B$, and the wavenumber k_r in the direction of the normal is defined by $k_\perp^2 = k_r^2 + k_b^2$.

In the quasiclassical approximation, in which all wavenumbers are assumed to be sufficiently large, the form of dispersion relation (1) for toroidal systems of arbitrary geometry should be the same. This assertion can be exemplified by the well-known equations for ideal ballooning modes (see, e.g., [7], Section 6)

$$-\rho\omega^2\frac{k_\perp^2}{k_b^2}\xi = \mathbf{B}\cdot\nabla\left(\frac{k_\perp^2}{k_b^2}\mathbf{B}\cdot\nabla\xi\right) + 2\frac{[\mathbf{B}\times\boldsymbol{\kappa}]\cdot\mathbf{k}_\perp}{Bk_b}$$
$$\times\left\{p'\xi + \frac{\gamma_0 pB^2}{\gamma_0 p + B^2}\left(\mathbf{B}\cdot\nabla\frac{\tau}{B^2} - 2\frac{[\mathbf{B}\times\boldsymbol{\kappa}]\cdot\mathbf{k}_\perp}{Bk_b}\xi\right)\right\}, \quad (2)$$
$$-\rho\omega^2\tau$$
$$= \mathbf{B}\cdot\nabla\left\{\frac{\gamma_0 pB^2}{\gamma_0 p + B^2}\left(\mathbf{B}\cdot\nabla\frac{\tau}{B^2} - 2\frac{[\mathbf{B}\times\boldsymbol{\kappa}]\cdot\mathbf{k}_\perp}{Bk_b}\xi\right)\right\}.$$

Here, ξ and τ are the transverse (along the normal to the magnetic surface) and longitudinal (along the magnetic field lines) plasma displacements, respectively; $\boldsymbol{\kappa} = \left(\frac{\mathbf{B}}{B}\cdot\nabla\right)\frac{\mathbf{B}}{B}$ is the curvature vector of the magnetic field line; $\mathbf{k}$ is the wave vector; $\mathbf{k}_\perp = \frac{[\mathbf{B}\times[\mathbf{k}\times\mathbf{B}]]}{B^2}$ and $k_b = \left[\frac{\mathbf{B}}{B}\times\nabla a\right]\cdot\mathbf{k}$ are the normal and azimuthal components of the wave vector; a is the label ("radius") of the equilibrium magnetic surface; and the prime denotes the derivative with respect to a. In the quasiclassical approximation, the perturbations in Eqs. (2) are represented as

$$\tau, \xi = C_{1,2}\exp(i\int k_\parallel dl), \quad (3)$$

where $C_{1,2}$ are slowly varying functions along the magnetic field lines. In this case, the second of Eqs. (2) gives the relationship between C_1 and C_2,

$$C_1 = \frac{2c_s^2 Bik_\parallel}{[\omega^2(1+\gamma_0 p/B^2) - c_s^2 k_\parallel^2]R}C_2, \quad (4)$$

and the first of Eqs. (2) yields the dispersion relation

$$\omega^2 = k_\parallel^2 V_A^2 + \frac{2k_b^2}{k_\perp^2 R^2}\left(\frac{p'R}{\rho} + \frac{2\omega^2 c_s^2}{\omega^2(1+\gamma_0 p/B^2) - c_s^2 k_\parallel^2}\right), \quad (5)$$

where $R = -Bk_b/[\mathbf{B}\times\boldsymbol{\kappa}]\cdot\mathbf{k}_\perp$ is radius of curvature of the magnetic field line. Note that dispersion relation (5) contains a combination of parameters that is independent of the choice of the magnetic surface label a. For $\beta \ll 1$, this dispersion relation formally coincides with dispersion relation (1), the only difference being that the magnetic field lines can be of variable curvature and the wavenumbers can change along them.

Dispersion relation (5) makes it possible to qualitatively demonstrate the well-known results on the stability of ideal MHD modes.

(i) For flute oscillations in systems with closed magnetic field lines, we have $k_\parallel \equiv 0$, so that dispersion relation (5) yields the Bernstein–Kadomtsev stability condition

$$p'R(1+\gamma_0 p/B^2)/p + 2\gamma_0 \geq 0. \quad (6)$$

Note that this condition is independent of the choice of the magnetic surface label.

(ii) In systems with a nonzero rotational transform, magnetic shear determines the finite value of $k_\parallel$ (in this case, $k_\parallel = 0$ only at a rational magnetic surface), so that dispersion relation (5) yields a Sydam–Mercier stability condition[1]

$$k_\parallel^2 > k_{\parallel 0}^2 = -2k_b^2 p'/(k_\perp^2 R V_A^2 \rho). \quad (7)$$

(iii) An analogous condition is also obtained for the stabilization of flute oscillations by the ends in an open device in which the plasma is in good electrical contact with the metal ends along the magnetic field lines and the finite value of $k_\parallel$ is determined by the finite device length.

(iv) At the stability boundary $\omega = 0$, dispersion relation (5) yields $k_\parallel^2 = -\frac{2k_b^2 p'}{k_\perp^2 B^2 R}$. This indicates that the longitudinal wavenumber $k_\parallel$ is real only in the regions of an unfavorable curvature of magnetic field lines, in which $p'/R < 0$ (it is assumed that $p' < 0$). It is well known that the physical meaning of ballooning perturbations is associated specifically with this property. The threshold for the onset of a ballooning mode can be estimated from the condition $\int_{l_1}^{l_2} k_\parallel dl \sim 1$, where the integration is carried out along a magnetic field line between the points at which the field line curvature vanishes ($k_\parallel = 0$). We can see that the ballooning instability

[1] To reduce the Sydam–Mercier criterion to its usual form, it is necessary to determine the radial dependences of MHD modes (see, e.g., [1]), i.e., to find the values of the wave vectors.

must necessarily have a threshold in terms of the plasma pressure.

(v) For a finite $k_\parallel$ value, the situation in which Bernstein–Kadomtsev condition (6) is satisfied while Sydam–Mercier criterion (7) is not corresponds to an instability growing at the rate of acoustic perturbations, $\gamma \sim k_\parallel c_s$, which is considerably slower than the rate of Alfvén perturbations, $\gamma \sim k_\parallel V_A$, in a low-$\beta$ plasma. An analogous conclusion is also true for ballooning modes.

The above results are also confirmed by a nonlocal analysis with allowance for the actual magnetic field geometry (see [1] for details). Hence, the above form of the local dispersion relation is universal. Physically, the choice of the longitudinal wavenumber depends on the particular problem to be solved.

Dispersion relationship (5) makes it possible to determine the relationship between the types of oscillations in a homogeneous plasma and unstable MHD modes in an inhomogeneous plasma. For magnetic configurations in which the curvature of the magnetic field lines is zero, dispersion relation (5) implies that there are two types of waves: Alfvén waves (with the frequency $\omega = k_\parallel V_A$) and acoustic waves (with the frequency $\omega = k_\parallel c_s$). When the magnetic field line curvature is finite (nonzero), these types of waves turn out to be coupled to one another, and the Bernstein–Kadomtsev condition determines which type is more important. However, the most usual practice is to use the Bernstein–Kadomtsev condition to decide whether or not the plasma compressibility must be taken into account. It should be emphasized that magnetoacoustic oscillations (with the frequency $\omega = kV_A$) are not described by dispersion relation (5) (see further analysis and Section 5 in [5]).

Since, in actual experiments (see, e.g., [2]), the parameters of the electron plasma component can differ substantially from those of the ion plasma component, we consider how dispersion relation (5) can be generalized to an anisotropic plasma of finite pressure. To do this, we will use the kinetic results that were obtained in Section 15 of [5] in the Chew–Goldberger–Low approximation, in which the plasma length is assumed to be large, $\omega\tau \gg 1$, where τ is the period of revolution of a particle along the magnetic confinement system (see, e.g., [6], Section 4). The main purpose of the generalization is to reveal new effects that influence the MHD plasma stability and that have not yet been taken into account.

2. KINETIC THEORY OF LOCAL MHD PERTURBATIONS

The most complete description of the kinetic theory of local perturbations with frequencies ω below the ion cyclotron frequency ω_{ci} in the approximation in which the Larmor radii of the particles are assumed to be zero (i.e., the characteristic frequencies of the perturbations are assumed to be much higher than the drift and magnetic drift frequencies and the terms on the order of $k_\perp^2 V_\perp^2/\omega_{ci}^2$ are ignored in comparison with unity) was given in Section 15 of [5]. We use the general dispersion relation that was obtained in the limit in which the plasma conductivity along the magnetic field lines is infinitely high (the longitudinal component of the dielectric tensor tends to infinity, $\varepsilon_{33} \longrightarrow \infty$):

$$\left(\varepsilon_{11} - \frac{c^2 k_\parallel^2}{\omega^2}\right)\left(\varepsilon_{22} - \frac{c^2 k^2}{\omega^2}\right) + \varepsilon_{12}^2 = 0. \qquad (8)$$

Here, the components of the dielectric tensor have the form (we follow the notation used in [5] for the arguments of the distribution function $f(E, \mu)$, namely, $E = V^2/2$ is the energy per unit mass M and $\mu = V_\perp^2/2B$ is the magnetic moment per unit mass)

$$\varepsilon_{11} = \frac{c^2}{V_A^2} + \frac{c^2 k_\parallel^2 \sigma_-}{\omega^2} + \frac{k_b^2 c^2}{\omega^2 k_\perp^2 R^2 B^2}\left[-R(p_\parallel' + p_\perp') - B^2(\sigma_- + \sigma_\perp) + \sum M\left\langle \frac{\omega\left(V_\parallel^2 + \frac{1}{2}V_\perp^2\right)^2}{\omega - k_\parallel V_\parallel}\frac{\partial f}{\partial E}\right\rangle\right],$$

$$\varepsilon_{12} = -i\frac{k_b c^2}{\omega^2 R B^2}$$

$$\times\left[-B^2(\sigma_- + \sigma_\perp) + \sum M\left\langle \frac{\omega\left(V_\parallel^2 + \frac{1}{2}V_\perp^2\right)V_\perp^2}{2(\omega - k_\parallel V_\parallel)}\frac{\partial f}{\partial E}\right\rangle\right], \qquad (9)$$

$$\varepsilon_{22} = \frac{c^2}{V_A^2} + \frac{c^2 k_\parallel^2 \sigma_-}{\omega^2} + \frac{k_\perp^2 c^2}{\omega^2 B^2}\left[-B^2\sigma_\perp + \sum M\left\langle \frac{\omega V_\perp^4}{4(\omega - k_\parallel V_\parallel)}\frac{\partial f}{\partial E}\right\rangle\right],$$

$$\sigma_- = \frac{p_\parallel - p_\perp}{B^2}, \quad \sigma_\perp = -\frac{1}{B^2}\sum M\left\langle \frac{V_\perp^4}{4B}\frac{\partial f}{\partial \mu}\right\rangle,$$

where the prime denotes the derivative with respect to radius, the angular brackets stand for averaging over the distribution function, and the summation is over all particle species (electrons and ions) (for details, see [5], Section 1).

For small values of the parameter β ($\varepsilon_{12} \longrightarrow 0$), general dispersion relation (8) describes two types of independent oscillations with the dispersion relations

$$\varepsilon_{11} - c^2 k_\parallel^2/\omega^2 = 0, \tag{10}$$

$$\varepsilon_{22} - c^2 k^2/\omega^2 = 0. \tag{11}$$

Dispersion relation (10) describes Alfvén and acoustic waves and is a generalization of dispersion relation (5). Dispersion relation (11) describes magnetoacoustic oscillations. In an anisotropic high-β plasma in a nonuniform magnetic field, acoustic, magnetoacoustic, and Alfvén waves are mutually coupled to one another.

In order to determine the conditions under which these waves become coupled, we analyze dispersion relation (8) in a number of important cases with quasi-flute oscillations ($k_\parallel \ll k_\perp$).

2.1. Isotropic Isothermal Maxwellian Plasma

In this case, magnetoacoustic perturbations are stable ($\varepsilon_{22} - c^2k^2/\omega^2 \neq 0$), and the dispersion relation can be rewritten in the form

$$\varepsilon_{11} - \frac{c^2 k_\parallel^2}{\omega^2} = -\frac{\varepsilon_{12}^2}{\varepsilon_{22} - \dfrac{c^2 k^2}{\omega^2}}. \tag{12}$$

Using the equation $\dfrac{df}{dE} = -\dfrac{M}{T} f$ for a Maxwellian distribution function, we represent dispersion relation (8) as

$$\omega^2 = k_\parallel^2 V_A^2 + \frac{2k_b^2}{k_\perp^2 R^2}\left\{\frac{Rp'}{\rho} + \frac{p}{\rho}\left[\sum_j\left(-i\sqrt{\pi}z_j W(z_j)\left(z_j^4 + z_j^2 + \frac{1}{2}\right) - z_j^2\left(z_j^2 + \frac{3}{2}\right)\right)\right.\right.$$
$$\left.\left. - \beta\frac{\left(\sum_j(-i\sqrt{\pi}z_j W(z_j)(1+z_j^2) - z_j^2)\right)^2}{4\left(1 + \frac{1}{2}\beta\sum_j(-i\sqrt{\pi}z_j W(z_j))\right)}\right]\right\}, \tag{13}$$

where $z_j = \omega/k_\parallel V_{Tj}$, $V_{Tj}^2 = 2T/M_j$, and $\beta = 2p/B^2$. The function $W(z)$, which is widely used in the electrodynamics of Maxwellian plasmas, is given by the formula

$$-i\sqrt{\pi}z W(z) = \int_{-\infty}^{\infty} \frac{\omega}{\omega - k_\parallel V_\parallel}\left(\frac{M}{2\pi T}\right)^{1/2}\exp\left(-\frac{MV_\parallel^2}{2T}\right)dV_\parallel. \tag{14}$$

Introducing the growth rate γ of the MHD instability by the definition $\omega = i\gamma$ and using the relationship $-izW(z) = \hat{z}\exp(\hat{z}^2)\mathrm{erfc}(\hat{z})$, where $\hat{z} = \gamma/k_\parallel V_T$ and $\mathrm{erfc}(x)$ is the probability integral of the real argument, we readily see that dispersion relation (13) reduces to the equation for determining the real value $\gamma > 0$. This result reflects the well-known fact that, in the approximation in which the Larmor radii of the particles are assumed to be zero, the rapid oscillations under consideration do not interact resonantly with the plasma particles (see, e.g., [5], Section 2).

A simple analysis of dispersion relation (13) shows that, for $\gamma = 0$ and $k_\parallel \neq 0$ ($\hat{z}_{e,i} = 0$), it yields Sydam–Mercier stability criterion (7) and, for $k_\parallel \equiv 0$ ($\hat{z}_{e,i} \gg 1$), it leads to the adiabatic exponent $\gamma_0 = \gamma_{0e} = \gamma_{0i} = \dfrac{14 + 5\beta}{8(1+\beta)}$ (see [8], p. 89) and also gives Bernstein–Kadomtsev stability criterion (6). Hence, the above kinetic analysis makes it possible to determine the adiabatic exponents for electrons and ions in the Bernstein–Kadomtsev stability criterion and does not reveal any changes in the stability criteria. As an example, Fig. 1 illustrates how the solution to dispersion relation (13) depends on the longitudinal wavenumber (the magnetic shear) for different values of the parameters $-Rp'/p$ and β.

Since $\hat{z}_i \gg \hat{z}_e$, we can see that, for finite $k_\parallel$ values, there exists a transition region in which the electron compressibility in the Bernstein–Kadomtsev condition vanishes ($\hat{z}_e \sim 1$) while the ion compressibility does not ($\hat{z}_i \gg 1$). In this transition region, the coefficient 2

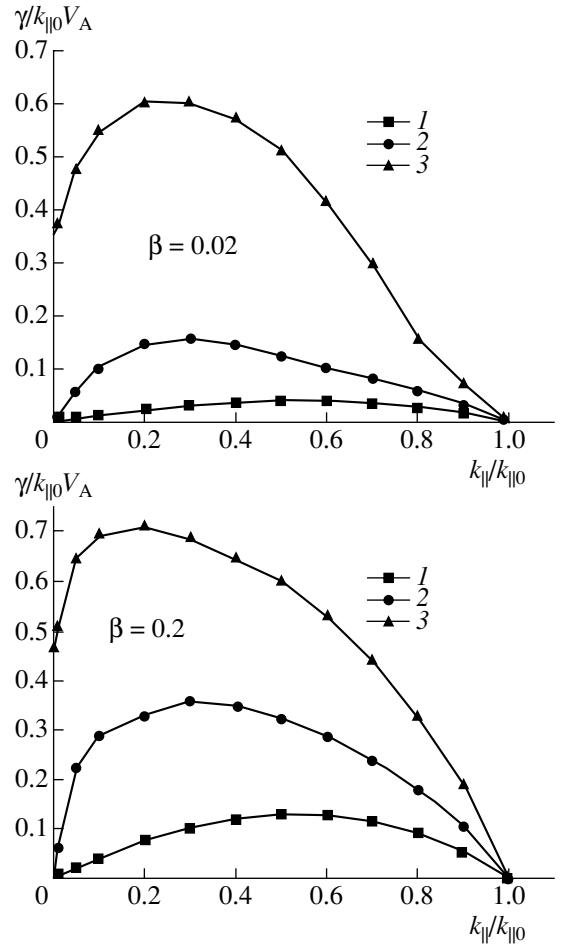

Fig. 1. Dependence of the dimensionless growth rate on the dimensionless longitudinal wavenumber for (*1*) $-Rp'/p = 1$ (the Bernstein–Kadomtsev criterion is satisfied), (*2*) $-Rp'/p = 2$ (the transition region), and (*3*) $-Rp'/p = 4$ (the Bernstein–Kadomtsev criterion is violated).

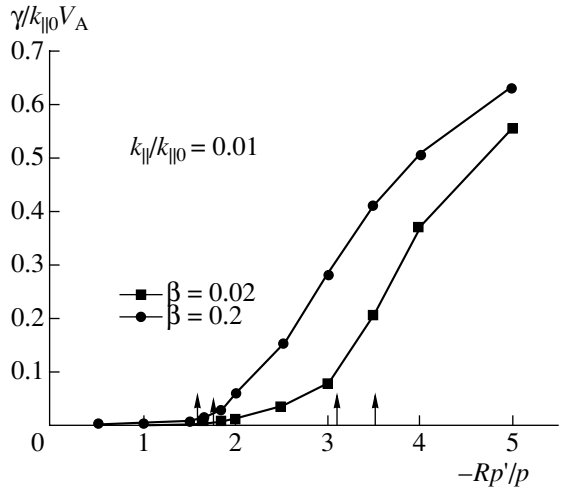

Fig. 2. Dependence of the dimensionless growth rate on the dimensionless pressure gradient. The arrows indicate the transition region between the regions in which the Bernstein–Kadomtsev condition is satisfied and is violated (the region of strong instability is to the right of the arrows).

drops out of Bernstein–Kadomtsev condition (6), which thus becomes more stringent. Figure 2 shows how the solution to dispersion relation (13) depends on the pressure gradient for a small shear (a small longitudinal wavenumber) and for different β values. It can be seen that the instability growth rate is slow only when the more stringent Bernstein–Kadomtsev condition (without the coefficient 2) is satisfied. Hence, we arrive at the following conclusion: the stability condition for a plasma with hot electrons, namely, the requirement that the longitudinal wavenumber be close to zero, is more stringent than the same stability condition for a plasma with hot ions.

It turns out that this conclusion can also be derived by generalizing dispersion relation (1) in the two-fluid ideal MHD approximation.

Two-fluid ideal MHD approximation at $\beta \ll 1$. In the two-fluid ideal MHD approximation, the perturbed plasma pressure $\tilde{p}$ has the form

$$\tilde{p} = -\xi_r p' + \sum_{j=e,i} \tilde{p}_j^c, \tag{15}$$

where the plasma pressure p is the sum of the ion pressure p_i and electron pressure p_e. The part of the perturbation that is associated with the compressibility of the ions and electrons is described by the formula

$$\tilde{p}_j^c = -\gamma_{0j}\rho_j\left(\nabla\cdot\boldsymbol{\xi}_\perp + \frac{\mathbf{B}}{B}\cdot\nabla\xi_{\|j}\right), \tag{16}$$

where ρ_j, $\xi_{\|j}$, and γ_{0j} are the mass density, longitudinal displacement, and the adiabatic exponent of the electron and ion fluids. Repeating the derivation given in the Introduction yields

$$\tilde{p} = -\xi_r\left(p' + \frac{2\gamma_{0e}p_e}{R}\frac{\omega^2}{\omega^2 - c_{se}^2k_\|^2} + \frac{2\gamma_{0i}p_i}{R}\frac{\omega^2}{\omega^2 - c_{si}^2k_\|^2}\right), \tag{17}$$

where $c_{se,i}^2 = \gamma_{0e,i}p_{e,i}/\rho_{e,i}$.

Setting $\gamma_0 = \gamma_{0e} = \gamma_{0i}$ and using expression (17), we obtain the local dispersion relation [cf. dispersion relation (1)]

$$\omega^2 = k_\|^2V_A^2 + \frac{2k_b^2}{k_\perp^2R^2}\left(\frac{Rp'}{\rho} + 2\frac{c_{si}^2\omega^2}{\omega^2 - c_{si}^2k_\|^2} + 2\frac{\hat{c}_s^2\omega^2}{\omega^2 - c_{se}^2k_\|^2}\right), \tag{18}$$

where $\hat{c}_s^2 = \gamma_0T_e/M_i$, with T_e the electron temperature and M_i the mass of an ion.

As is seen, dispersion relation (18) does not lead to any changes in the form of the stability criteria. The only change in the quantities is that the values of the instability growth rates as functions of the longitudinal wavenumber now differ from the values obtained above, the difference being especially pronounced at longitudinal wavenumbers close to $k_\parallel = 0$. Let us obtain the equation for the derivative $y = d\omega^2/dk_\parallel^2$ at the initial portion ($k_\parallel = 0$) of the dispersion curve $\omega = 0$ in the case of an isothermal plasma ($T_e = T_i$). To do this, we first differentiate dispersion relation (18) with respect to $k_\parallel^2$. The same dispersion relation (18) then helps us to eliminate some terms in the resulting relation. Finally, setting $\omega^2 = yk_\parallel^2$, we arrive at the desired equation for y:

$$y^2 - yc_{se}^2 \frac{1 + \dfrac{\gamma_0 p}{Rp'}}{1 + \dfrac{2\gamma_0 p}{Rp'}} + \frac{c_{si}^2 c_{se}^2}{1 + \dfrac{2\gamma_0 p}{Rp'}} = 0. \qquad (19)$$

Under the Bernstein–Kadomtsev condition $\left(1 + \dfrac{2\gamma_0 p}{Rp'} < 0\right)$, one of the two solutions to Eq. (19) is always negative (which corresponds to the instability of the acoustic mode). Further, in the transition region ($1 + \dfrac{\gamma_0 p}{Rp'} > 0$), the derivative $y = c_{se}^2\left(1 + \dfrac{\gamma_0 p}{Rp'}\right)/\left(1 + \dfrac{2\gamma_0 p}{Rp'}\right)$ in the unstable solution is large (see Fig. 3). Under the more stringent Bernstein–Kadomtsev condition ($1 + \dfrac{\gamma_0 p}{Rp'} < 0$), however, the derivative is appreciably smaller, $y = c_{si}^2\left(1 + \dfrac{\gamma_0 p}{Rp'}\right)^{-1}$. Figure 3 illustrates the results of a numerical solution of dispersion relation (18) in the transition region for different values of the longitudinal wavenumber. A comparison with an analogous calculation carried out in [1] shows that a third stable solution appears and that the growth rate of the acoustic instability becomes markedly faster because, in the transition region, the electron compressibility vanishes in the Bernstein–Kadomtsev condition. Figure 3 agrees with the corresponding kinetic calculation, the results of which are shown in Fig. 1.

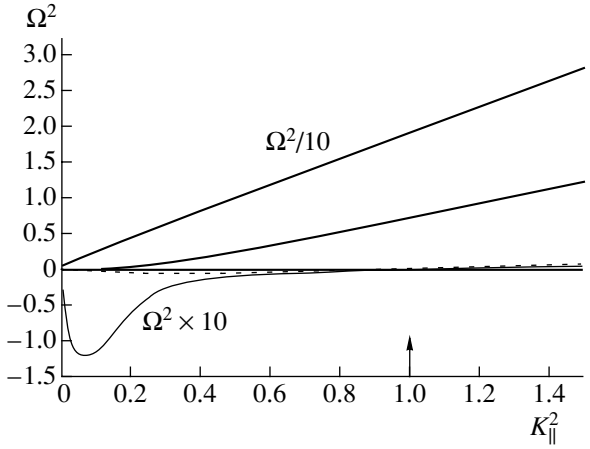

Fig. 3. Dependence of $\Omega^2 = \omega^2/k_{\parallel 0}^2 V_A^2$ on $K_\parallel^2 = k_\parallel^2/k_{\parallel 0}^2$ in the transition region for the Bernstein–Kadomtsev condition at $\gamma_0 p/Rp' = -0.75$, $T_e = T_i$ and $c_s^2/V_A^2 = 0.02$. The arrow refers to the Sydam–Mercier criterion. The dotted curve was calculated in the one-fluid MHD approximation [1].

2.2. Anisotropic Maxwellian Plasma

It is well known that the anisotropy of the distribution function can give rise to new MHD instabilities, namely, firehose and mirror instabilities. Let us consider how they manifest themselves in the local dispersion relation. Using the distribution function

$$f = n\frac{M}{2\pi T_\perp}\left(\frac{M}{2\pi T_\parallel}\right)^{1/2} \exp\left[-\frac{M}{2}\left(\frac{V_\perp^2}{T_\perp} + \frac{V_\parallel^2}{T_\parallel}\right)\right], \qquad (20)$$

we represent dispersion relation (8) as

$$\left\{\omega^2 - k_\parallel^2 V_A^2(1 + \beta_\perp - \beta_\parallel) - \frac{k_b^2 c_s^2}{k_\perp^2 R^2}\left[\frac{R(p_\perp + p_\parallel)'}{p_\perp + p_\parallel} + 1 - \frac{2}{p_\perp + p_\parallel}\sum_j p_{\perp j}\left(F(z_j)\left(\frac{T_{\perp j}}{T_{\parallel j}} + 2z_j^2 + 2z_j^4\frac{T_{\parallel j}}{T_{\perp j}}\right) + z_j^2\frac{T_{\parallel j}}{T_{\perp j}}\right)\right]\right\} \qquad (21)$$

$$\times\left\{\omega^2 - k_\perp^2 V_A^2\left[1 + 2\beta_\perp - 2\sum_j \beta_{\perp j}\frac{T_{\perp j}}{T_{\parallel j}}F(z_j)\right]\right\}$$

$$= \frac{k_b^2 c_s^4}{R^2}\left(1 - \frac{2}{p_\perp + p_\parallel}\sum_j p_{\perp j}F(z_j)\left(\frac{T_{\perp j}}{T_{\parallel j}} + z_j^2\right)\right)^2,$$

where $\beta_\perp = \dfrac{n}{B^2}\sum_j T_{\perp j}$, $\beta_\parallel = \dfrac{n}{B^2}\sum_j T_{\parallel j}$, $z_j = \dfrac{\omega}{k_\parallel}\sqrt{\dfrac{M_j}{2T_{\parallel j}}}$, $c_s^2 = \dfrac{p_\perp + p_\parallel}{\rho}$, and where we have introduced the function $F(z) = 1 + i\sqrt{\pi}zW(z)$.

Dispersion relation (21) implies that the firehose instability develops under the condition $(1 + \beta_\perp - \beta_\parallel) < 0$ and that the condition for the onset of the mirror instability has the form $\left(1 + 2\beta_\perp - 2\sum_j \beta_{\perp j}\dfrac{T_{\perp j}}{T_{\parallel j}}F(z_j)\right) < 0$

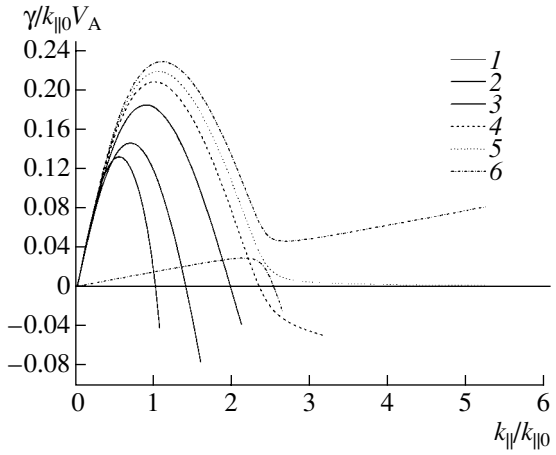

Fig. 4. Dependence of the dimensionless growth rate on the dimensionless longitudinal wavenumber for different degrees of ion anisotropy $T_{\perp i}/T_{\|i}$ = (*1*) 1, (*2*) 2, (*3*) 3.5, (*4*) 4.5, (*5*) 5, and (*6*) 5.5 at $T_{\perp e} = T_{\|e} = T_{\|i}$, $-R(p_\perp + p_\|)'/(p_\perp + p_\|) = 1$ (a more stringent version of the Bernstein–Kadomtsev condition is satisfied), $\beta = 0.2$, and $k_{\|0}/k_\perp = 0.001$. At $T_\perp/T_\| \sim 5$, the condition for the onset of the mirror instability is satisfied.

(see [8], p. 81). It should be stressed that the mirror instability is driven by magnetoacoustic oscillations.

An anisotropic plasma of practical interest is that in which $T_\perp > T_\|$. Such plasmas are often encountered in rippled confinement systems utilizing electromagnetic wave heating methods and neutral-beam injection heating methods. Arsenin and Kuyanov [9] noted that the conditions in an anisotropic plasma such that $T_\perp > T_\|$ may be favorable for the MHD stabilization by compressibility. This is why it is expedient to examine this point in more detail.

Since the compressibility shows itself at $z_{e,i} \gg 1$, a decrease in $T_\|$ when the total pressure is kept fixed may be beneficial for stabilization. For $k_\| = 0$ ($z_{e,i} \longrightarrow \infty$), the mirror and firehose instabilities do not occur and the Bernstein–Kadomtsev condition for an anisotropic plasma takes the form

$$R\frac{(p_\perp + p_\|)'}{p_\perp + p_\|} + 1 + \frac{1}{p_\perp + p_\|}\sum_j p_{\perp j}\left(2 + 3\frac{T_{\|j}}{T_{\perp j}}\right) - \frac{\beta}{1 + 2\beta_\perp}\left(1 + \frac{p_\perp}{p_\perp + p_\|}\right)^2 > 0. \quad (22)$$

It is seen that even strong plasma anisotropy ($T_\perp \gg T_\|$) has little effect on condition (22) for stability of the flute modes. However, the situation in which $\omega = 0$ and $k_\| \neq 0$ ($z_{e,i} = 0$) is radically different. In this case, the stability condition has the form

$$k_\|^2 > \frac{k_{\|0}^2}{1 + \beta_\perp - \beta_\|}\left[1 + \frac{1 - \frac{2}{p_\perp + p_\|}\sum_j p_{\perp j}\frac{T_{\perp j}}{T_{\|j}}}{\frac{(p_\perp + p_\|)'R}{p_\perp + p_\|}} - \frac{\beta\left(1 - \frac{2}{p_\perp + p_\|}\sum_j p_{\perp j}\frac{T_{\perp j}}{T_{\|j}}\right)^2}{\frac{(p_\perp + p_\|)'R}{p_\perp + p_\|}\left(1 + 2\beta_\perp - 2\sum_j \beta_{\perp j}\frac{T_{\perp j}}{T_{\|j}}\right)}\right], \quad (23)$$

where $k_{\|0}^2 = -k_b^2(p_\perp + p_\|)'/(k_\perp^2 R V_A^2 \rho)$. We can see that the Sydam–Mercier criterion for stability of a plasma with a sufficiently strong anisotropy can change radically even when the parameter β is small.

The dependence of the growth rates of unstable oscillations on the longitudinal wavenumber at different degrees of plasma anisotropy is shown in Fig. 4, which illustrates the results of calculations from dispersion relation (21) under condition (22). We can see that, at small longitudinal wavenumbers, the dispersion relation is essentially independent of the degree of anisotropy. When the anisotropy is sufficiently large, the condition for the onset of the mirror instability is satisfied and an additional magnetoacoustic instability branch appears that grows at a rate on the order of the growth rate of the ion acoustic oscillations. Hence, moderate plasma anisotropy does not substantially degrade the stabilization of quasi-flute oscillations by plasma compressibility.

Figure 4 also implies that, in an anisotropic plasma, Alfvén, ion acoustic, and magnetoacoustic oscillations are mutually coupled to one another, giving rise to quasi-flute MHD instabilities of an inhomogeneous plasma.

3. CONCLUSIONS

The local dispersion relation derived above for an inhomogeneous plasma provides a convenient tool for studying the qualitative picture of small-scale MHD instabilities in magnetic confinement systems. With this relation, it has been possible to establish that, in alternative configurations, it is important to satisfy the Bernstein–Kadomtsev condition in order to reduce the growth rate of the quasi-flute oscillations. It has been shown that moderate plasma anisotropy does not have a considerable destabilizing effect on the MHD plasma stability in alternative systems under the Bernstein–Kadomtsev condition.

The local dispersion relation shows that the natural oscillations of a homogeneous plasma—such as Alfvén, ion acoustic, and magnetoacoustic oscilla-

tions—and unstable quasi-flute MHD oscillations of an inhomogeneous anisotropic plasma are mutually coupled to one another.

ACKNOWLEDGMENTS

This work was supported in part by the Department of Atomic Science and Technology of the RF Ministry of Atomic Industry, the Russian Federal Program for State Support of Leading Scientific Schools (project no. NSh-2024.2003.2), and the Russian Foundation for Basic Research (project no. 03-02-16768).

REFERENCES

1. A. B. Mikhailovskii and A. A. Skovoroda, Plasma Phys. Controlled Fusion **44**, 2033 (2002).
2. V. V. Arsenin, E. D. Dlougach, V. M. Kulygin, *et al.*, Nucl. Fusion **41**, 945 (2001).
3. A. I. Morozov, V. P. Pastukhov, and A. Yu. Sokolov, in *Proceedings of the International Workshop on D-^{3}He Based Reactor Studies, Moscow, 1991*, p. 1C1.
4. A. Hasegava, L. Chen, and M. E. Mauel, Nucl. Fusion **30**, 2405 (1990).
5. A. B. Mikhailovskii, *Electromagnetic Instabilities of Nonuniform Plasmas* (Énergoatomizdat, Moscow, 1991).
6. A. B. Mikhailovskii, *Plasma Instabilities in Magnetic Confinement Systems* (Atomizdat, Moscow, 1978).
7. V. D. Pustovitov and V. D. Shafranov, in *Reviews of Plasma Physics*, Ed. by B. B. Kadomtsev (Énergoatomizdat, Moscow, 1987; Consultants Bureau, New York, 1990), Vol. 15.
8. B. B. Kadomtsev, *Plasma Physics and the Problem of Controlled Thermonuclear Reactions*, Ed. by M. A. Leontovich (Izd. Akad. Nauk SSSR, Moscow, 1958; Pergamon, London, 1959).
9. V. V. Arsenin and A. Yu. Kuyanov, Fiz. Plazmy **27**, 675 (2001) [Plasma Phys. Rep. **27**, 635 (2001)].

Translated by O.E. Khadin

Plasma Physics Reports, Vol. 30, No. 4, 2004, pp. 338–342. Translated from Fizika Plazmy, Vol. 30, No. 4, 2004, pp. 369–374.

TRANSPORT PROCESSES

Description of the Anomalous Diffusion of Fast Electrons by a Kinetic Equation with a Fractional Spatial Derivative

O. G. Bakunin

Russian Research Centre Kurchatov Institute, pl. Kurchatova 1, Moscow, 123182 Russia

Received July 7, 2003

Abstract—It is proposed to use fractional spatial derivatives to describe the effect of anomalous diffusion of fast electrons in a stochastic magnetic field on the shape of the distribution function. A self-similar kinetic equation is considered. The use of self-similar variables makes it possible to determine the velocity range in which the distribution function is distorted to the greatest extent. Calculations show that the quantities associated with the stochasticity of the magnetic field lines can be estimated from the experimentally measured characteristic energies of suprathermal electrons in the energy range in which the behavior of the distribution function changes substantially. *© 2004 MAIK "Nauka/Interperiodica".*

1. INTRODUCTION

The theoretical description of anomalous transport processes in plasma often involves the use of scalings. In transport theory, one of the most widely applicable scalings is that for the root-mean-square deviation R of a randomly walking particle in terms of the Hurst exponent H [1]:

$$R \propto t^H, \tag{1}$$

where t is the observation time. This scaling describe both the superdiffusion ($1/2 < H < 1$) and subdiffusion ($0 < H < 1/2$) of a particle. The case $H = 1/2$ corresponds to the classical diffusion. The results of an analysis of anomalous diffusion processes in tokamak plasmas in the self-organized criticality model [2, 3] have attracted widespread attention. It turns out that the exponent H varies in a fairly narrow range, $H = 0.62$–0.72. It is possible to study the relations between different scalings describing different physical parameters of the same system, e.g., the relation of the Hurst exponent to the exponent describing the power-law tail of the autocorrelation function [4].

The purely empirical character of scalings of form (1) makes it necessary to search for quasi-diffusion equations that would provide a more rigorous justification of the scalings. One possible approach to solving this problem is to describe superdiffusion and subdiffusion by equations with fractional derivatives [5, 6]. Originally, this approach was employed to analyze anomalous diffusion in conventional coordinate space. Thus, the familiar Richardson law for the relative diffusion [7] of particles in turbulent flow,

$$R^2 \propto t^3 \gg t \quad \text{or} \quad D \approx \frac{R^2}{t} \propto R^{4/3}, \tag{2}$$

can be rewritten as the following equation with a fractional spatial derivative:

$$\frac{\partial n(t, x)}{\partial t} = \varepsilon \frac{\partial^{2/3} n(t, x)}{\partial x^{2/3}}. \tag{3}$$

Here, D is the particle diffusion coefficient, ε is the mean energy dissipation rate in turbulent flow, and n is the particle density. A rigorous mathematical justification of this approach was given in book [8] and reviews [9–11]. However, information about the behavior of solutions to quasi-diffusion equations can often be derived from elementary dimensionality considerations. Thus, a dimensionality analysis of Eq. (3) yields the simple relationship

$$\frac{n(t, x)}{t} \propto \frac{n(t, x)}{x^{2/3}}, \tag{4}$$

which is, in fact, Richardson scaling (2).

Another possible approach involves the use of equations with a fractional derivative with respect to time. For instance, the relevant equation obtained by Chukbar [13] in the Dreĭzin–Dykhne model [12] has the form

$$\frac{\partial^{3/2} n(t, x)}{\partial t^{3/2}} = D_{\text{eff}} \frac{\partial^2 n(t, x)}{\partial x^2} - \frac{n(0, x)}{2\sqrt{\pi} t^{3/2}}, \tag{5}$$

where D_{eff} is the effective particle diffusion coefficient. Sometimes, this form of the equation is more correct. Chukbar [13] discussed the advantages and disadvantages of each of these two approaches. The next logical step was to describe non-Maxwellian particle distribu-

tion functions f in terms of fractional derivatives in velocity space [14, 15]:

$$\frac{\partial f(t, v)}{\partial t} = D_v \frac{\partial^\sigma f(t, v)}{\partial v^\sigma}, \quad (6)$$

where D_v is the particle diffusion coefficient in phase space and σ is the fractional order of the derivative. It should be noted that the form of kinetic equations is significantly affected by the processes associated with the inhomogeneity of the medium. Even in classical theory, these processes give rise to terms containing spatial derivatives of the distribution function. In some cases, these derivatives can be fractional.

In this paper, we propose to use fractional spatial derivatives to describe the effect of anomalous diffusion of fast electrons in a stochastic magnetic field on the shape of the distribution function. We will consider a self-similar kinetic equation and establish the relationship between the Hurst exponent for anomalous spatial diffusion of fast electrons and the exponents characterizing the behavior of the distribution function of suprathermal electrons. Moreover, it will be shown that, in terms of self-similar variables, it is possible to determine the velocity range in which the distortion of the distribution function is especially great. It will also be shown that, based on the results of calculations, the quantities associated with the stochasticity of the magnetic field lines can be estimated from the experimentally measured characteristic energies of suprathermal electrons in the energy range in which the behavior of the distribution function changes substantially.

2. APPROXIMATE DESCRIPTION OF THE EFFECTS OF THE STOCHASTIC MAGNETIC FIELD IN THE KINETIC EQUATION

The solution of the total kinetic equation describing the effect of the stochastic magnetic field on the electron distribution function is a very difficult task. This is why even the first studies relied on a host of simplifying assumptions [16]. Thus, Gurevich *et al.* [16] considered only suprathermal electrons and represented the distribution function in a self-similar form. Later, Aleksandrov *et al.* [17] proposed self-similar variables that made it possible to apply classical methods for solving the kinetic equation for runaway electrons [18–20] to steady-state spatially nonuniform models [21, 22].

Gurevich *et al.* [16] used the following diffusive approximation of the collisional term describing the effect of the stochastic magnetic field on the behavior of fast electrons in the kinetic equation with a Fokker–Planck collision integral:

$$-|\mu| v D_m \frac{\partial^2 f}{\partial x^2} = \frac{1}{v^2}\frac{\partial}{\partial v}\left[v^2 \nu_e(v)\left(vf + \frac{T_e(x)}{m}\frac{\partial f}{\partial v}\right)\right] + \nu_e(v)\frac{\partial}{\partial \mu}\left[(1-\mu^2)\frac{\partial f}{\partial \mu}\right], \quad (7)$$

$$\nu_e(v, x) = \frac{4\pi e^4 \Lambda n_e(x)}{m^2 v^3}, \quad \mu = \cos\theta.$$

Here, $f(x, v, \mu)$ is the electron distribution function, D_m is the anomalous diffusion coefficient, ν_e is the electron collision frequency, T_e is the bulk electron temperature, n_e is the electron density, and θ and v are the pitch angle and absolute value of the electron velocity. This form of the collisional term agrees well with the generally accepted expression for the magnetic diffusion coefficient [23, 24]:

$$D_m = \frac{\Delta^2}{l}, \quad (8)$$

where Δ is the distance by which a magnetic field line is displaced in the transverse direction as passing over a distance l in the longitudinal direction.

However, as the understanding of turbulent diffusion in a stochastic magnetic field deepened, nondiffusive approximations have also come into use. In the present paper, it is proposed to approximate the term accounting for the effect of the stochastic magnetic field by the derivatives of fractional order γ:

$$\frac{\partial^\gamma f(v, x)}{\partial x^\gamma}. \quad (9)$$

The value of γ can be chosen to satisfy a particular nondiffusive scaling describing turbulent diffusion in a stochastic magnetic field. Thus, the widely used percolation approach [25, 26] yields the expression

$$D_m = \Delta b_0 R^{-\frac{1}{\nu D_H + 1}}, \quad (10)$$

where $R = b_0 \frac{l}{\Delta} \gg 1$ is the Kubo number, b_0 is the relative amplitude of the magnetic field fluctuations, and $\nu = 4/3$ and $D_H = 1 + \frac{1}{\nu}$ are the percolative exponents. In fact, this expression generalizes the Kadomtsev–Pogutse scaling $D_T \approx b_0 \Delta$ [27] to a form in which the magnetic diffusion coefficient depends parametrically on the Kubo number with an arbitrary exponent w:

$$D_m = \Delta b_0 R^{-w}. \quad (11)$$

If we assume that $D_m \approx$ const, then we arrive at the nondiffusive scaling

$$\Delta^{\frac{1+w}{w}} \propto l. \quad (12)$$

For $w = 1$, the result reduces to expression (8). The case $w = 3/10$ corresponds to percolation limit (10). Note that, in order to derive the scaling for turbulent diffusion, it is necessary to make an additional assumption about the law $l = l(t)$ of the longitudinal particle motion. Dimensionality considerations yield the following relationship between the exponent γ, which determines the order of the fractional derivative, and the exponent w:

$$\gamma = \frac{1+w}{w}. \tag{13}$$

Of course, this is not the only possible way of using nondiffusive scalings to obtain kinetic equations with fractional spatial derivatives. In what follows, we will consider a more general case. It has been repeatedly suggested [28] that the coefficient of turbulent diffusion of fast electrons can depend on their longitudinal velocity in radically different manners. Thus, for classical magnetic diffusion, this dependence is $D_T \approx D_m v_\parallel \propto v_\parallel$ and, for turbulent diffusion in crossed fields, it is $D_T \propto 1/v_\parallel$. This is why, in the present paper, it is proposed to approximate the term accounting for the effect of a stochastic magnetic field by the expression

$$D_* v_\parallel^\beta \frac{\partial^\gamma f(v,x)}{\partial x^\gamma}, \tag{14}$$

where D_* is the proportionality coefficient and the quantities β and γ characterize the model chosen to describe anomalous transport processes.

3. SELF-SIMILAR ANALYSIS OF THE KINETIC EQUATION

Here, we analyze the character of self-similar solutions to the time-independent kinetic equation describing the distortion of the tail of the distribution function of suprathermal electrons due to their anomalous diffusion in a stochastic magnetic field:

$$\begin{aligned} &D_* v_\parallel^\beta \frac{\partial^\gamma f(v,x,\mu)}{\partial x^\gamma} \\ &= \frac{1}{v^2}\frac{\partial}{\partial v}\left[v^2 \nu_e(v)\left(vf + \frac{T_e(x)}{m}\frac{\partial f}{\partial v}\right)\right] \\ &\quad + \nu_e(v)\frac{\partial}{\partial \mu}\left[(1-\mu^2)\frac{\partial f}{\partial \mu}\right]. \end{aligned} \tag{15}$$

We ignore the term accounting for the effect of the electric field E [16], because the corresponding distortion is significant only at sufficiently high electron energies,

$$\varepsilon > \varepsilon_E \approx \frac{4\pi e^3 n_e \Lambda}{E}. \tag{16}$$

Usually, the electric field is as strong as $E \approx 5 \times 10^{-2}$ V/cm, so that for a plasma density of $n \approx 2 \times 10^{13}$ cm^{-3}, we obtain $\varepsilon \approx 100$ keV.

Following [17, 21, 22], we represent the distribution function of suprathermal electrons in the self-similar form

$$f(x, v, \mu) = \frac{F(\xi, \mu)}{T_e^\alpha(x)}, \tag{17}$$

where the dimensionless variable $\xi = \dfrac{m_e v^2}{2T_e(x)} = \dfrac{v^2}{v_T^2}$ characterizes the electron energy, v_T is the electron thermal velocity, and α is the self-similarity exponent. This representation allows us to reduce the problem of describing a spatially inhomogeneous medium to that of solving an equation that is very similar in structure to the equation for runaway electrons in a homogeneous plasma [18–20]. The technique for solving such equations is well developed and makes it possible to qualitatively analyze the behavior of the solutions by comparing the orders of terms in a nondimensionalized kinetic equation [16–22]. In fact, in the solution to the kinetic equation, the effects of the spatial inhomogeneity are accounted for by the parameter α, which serves to control the temperature and density profiles. This simplification is quite justified for problems associated with the analysis of localized regions in which magnetic field lines show stochastic behavior. Based on the experience gained in working with self-similar variables [17, 21, 22], we can retain only the lowest order term in the expression describing the effect of the stochastic magnetic field in the kinetic equation written in a self-similar form:

$$\frac{\partial^\gamma f(v,x)}{\partial x^\gamma} = \frac{\partial^\gamma}{\partial x^\gamma}\left[\frac{F(\xi,\mu)}{T(x)^\alpha}\right] \approx \frac{1}{T_e(x)^\alpha}\xi^\gamma \frac{\partial^\gamma F}{\partial \xi^\gamma}\frac{1}{L_\gamma}, \tag{18}$$

where the parameter $\dfrac{1}{L_\gamma} = T(x)\dfrac{\partial^\gamma}{\partial x^\gamma}\left[\dfrac{1}{T(x)}\right]$ characterizes the plasma inhomogeneity. Since we will be interested only in power-law plasma profiles, we assume that $T_e(x) \propto x^\eta$. We can now rewrite the basic kinetic equation as

$$\begin{aligned} &-\frac{\delta|\mu|^\beta \xi^{\frac{\beta+1}{2}}}{\xi}\xi^\gamma \frac{\partial^\gamma F}{\partial \xi^\gamma} \\ &= \frac{1}{\xi}\frac{\partial}{\partial \xi}\left(F + \frac{\partial F}{\partial \xi}\right) + \frac{1}{2\xi^2}\frac{\partial}{\partial \mu}\left[(1-\mu^2)\frac{\partial F}{\partial \mu}\right], \end{aligned} \tag{19}$$

where the quantity $\delta = \dfrac{D_* v_T^\beta}{2\nu_e(v_T)L_\gamma}$ includes the terms describing the spatial inhomogeneity of the plasma. According to [17, 21, 22], we impose the condition $\delta =$

const to obtain an equation that is similar in structure to the kinetic equation describing suprathermal electrons in a constant electric field. This condition, which is supplementary to representation (17), enables us to relate the temperature and density profiles in the plasma. For the conditions prevailing in a tokamak plasma, namely, $T \approx 2$ keV, $n \approx 2 \times 10^{13}$ cm^{-3}, $b_0 \approx 5 \times 10^{-5}$, $D \approx 1$ m^2/s, and $\lambda \approx \left(\frac{\partial \ln T(x)}{\partial x}\right)^{-1} \approx 20$ cm, we obtain the estimate $\delta \approx 5 \times 10^{-4}$. Using the methods developed in the theory of runaway electrons, we can determine the energy ranges in which the distribution function behaves in different ways.

The term describing the effect of the stochastic magnetic field is considered as a perturbation, and the parameter δ is assumed to be small. Then, by comparing the term describing the effect of the stochastic magnetic field with the term describing scattering, we can determine the energy range in which the electron distribution function is close to a spherically symmetric Maxwellian function:

$$\delta\xi^{\frac{2\gamma+\beta+1}{2}} < \frac{1}{\xi}. \tag{20}$$

or, equivalently, $\xi < \frac{1}{\delta^{\frac{2}{2\gamma+\beta+3}}}$. In this parameter range, it is expedient to expand the function F in Legendre polynomials:

$$F(\xi, \mu) = a_0 F_0(\xi) + a_1 F_1(\xi)\mu + \ldots. \tag{21}$$

In the range in which the distribution function is significantly distorted, we compare the term describing the effect of the stochastic magnetic field with those accounting for friction and diffusion in velocity space:

$$\frac{1}{\xi} < \delta\xi^{\frac{2\gamma+\beta+1}{2}} < 1. \tag{22}$$

In the range $\xi < \frac{1}{\delta^{\frac{2}{2\gamma+\beta+1}}}$, the distortions of the distribution function are great enough for the solutions to be sought in the form proposed in [18–20]:

$$F(\xi, \mu) = \exp(G(\xi, \mu)), \tag{23}$$

where the function G is expanded in powers of the small parameter $\delta^{\frac{2}{2\gamma+\beta+1}}$.

In the energy range

$$\delta\xi^{\frac{2\gamma+\beta+1}{2}} > 1 \tag{24}$$

the self-similar solution behaves asymptotically as a power-law tail of the distribution function:

$$F(\xi, \mu) \propto \frac{\Phi(\mu)}{\xi^{\alpha}}, \tag{25}$$

in which case, however, it is impossible to determine the specific form of the function Φ.

Thus, we have briefly characterized the solution to the kinetic equation [16–21]. However, the main objective of the present paper is to determine the limits of the range in which the distribution function is distorted to the greatest extent, specifically, the limits

$$\xi_1 \approx \frac{1}{\delta^{\frac{2}{2\gamma+\beta+3}}}, \quad \xi_2 \approx \frac{1}{\delta^{\frac{2}{2\gamma+\beta+1}}}, \tag{26}$$

which can be used to analyze the data from measurements of the distribution function. Note that the case $\gamma = 2$ refers to diffusive transport. For the above values of the plasma parameters, the energies corresponding to limits (26) are estimated to be $\varepsilon_1 \approx 20$ keV and $\varepsilon_2 \approx 30$ keV. These energies are appreciably lower than the threshold for generating runaway electrons, $\varepsilon_E \approx 100$ keV, which makes it possible to investigate anomalous diffusion effects experimentally. The distribution function of suprathermal electrons is unlikely to be measured with the accuracy required to verify theoretical predictions. This way, however, it seems possible to obtain a quite realistic qualitative picture of how the distribution function changes its behavior [16–20]. This is why the main goal of the present paper is to derive scalings for the limits ξ_1 and ξ_2. Measurements of these limits from the characteristic changes in the distribution function will provide information about the mechanism for anomalous transport in a stochastic magnetic field.

Let us now make several remarks on the structure of the kinetic equations under discussion. With the above results in mind, we simplify Eq. (15) to the maximum possible extent by keeping only the terms with the highest order derivatives in the range where the distribution function is highly non-Maxwellian:

$$\frac{\partial^{\gamma} f}{\partial x^{\gamma}} \approx \frac{\partial^2 f}{\partial v^2}. \tag{27}$$

If we take into account the fact that the variable ξ runs through all values from zero to infinity, then we can draw an analogy between this kinetic equation and approximate nonlocal diffusion equations with fractional spatial derivatives, such as the equation

$$\frac{\partial n(t, x)}{\partial t} = D\frac{\partial^{\kappa} n(t, x)}{\partial x^{\kappa}}. \tag{28}$$

We take the second time derivative of Eq. (28) to obtain

$$\frac{\partial^2 n(t, x)}{\partial t^2} = D\frac{\partial^{2\kappa} n(t, x)}{\partial x^{2\kappa}}. \tag{29}$$

Here, the range $\kappa < 2$ corresponds to superdiffusion in coordinate space. In the kinetic equation under consideration, the role of time is played by the variable ξ, so that similar regimes occur for $\gamma < 4$.

In accordance with the particle conservation condition, the self-similar character of the variables leads to the following relationship between the temperature and density profiles:

$$n_e(x) \propto T_e^{\frac{3}{2}-\alpha}. \quad (30)$$

Using the constancy of the self-similarity parameter, $\delta = \text{const}$, we can arrive at the condition for the self-similar profiles to be consistent with the exponents used:

$$\frac{T_e^{1+\beta}}{n_e(x)} T_e \frac{d^\gamma}{dx^\gamma}\left(\frac{1}{T_e(x)}\right) = \text{const}. \quad (31)$$

Assuming that, in the range under analysis, the temperature behaves according to a power law, $T_e(x) \propto x^\eta$, we obtain the equation

$$\eta(\beta + \alpha - 1/2) - \gamma = 0. \quad (32)$$

Resolving this equation yields the model profiles of the plasma parameters:

$$T_e(x) \propto x^{\frac{\gamma}{\beta+\alpha-1/2}}, \quad n_e(x) \propto x^{-\frac{(\alpha-3/2)\gamma}{\beta+\alpha-1/2}}. \quad (33)$$

Of particular interest is the fact that, for $\alpha > 3/2$, the monotonic behavior of $T_e(x)$ differs from that of $n_e(x)$. Thus, in the direction chosen in our analysis, the profile $T_e(x)$ decreases, while the profile $n_e(x)$ increases. Hence, the problem of describing the wall regions can be treated in self-similar variables.

4. CONCLUSIONS

A time-independent kinetic equation with a Fokker–Planck collision integral has been proposed that describes the effect of the stochastic magnetic field on the distribution function of suprathermal electrons by means of the term with a fractional spatial derivative. Self-similar solutions to this equation have been analyzed for approximate power-law profiles of the plasma temperature and density. The ranges where the distribution function is significantly distorted have been determined, and the energies at which the distribution function changes its behavior have been estimated. With the parametric scalings obtained in this study, it is possible to use the results from measurements of the distribution function of suprathermal electrons to analyze the mechanisms for turbulent transport in a stochastic magnetic field.

REFERENCES

1. J. Feder, *Fractals* (Plenum Press, New York, 1988; Mir, Moscow, 1991).
2. B. A. Carreras, B. Milligen, M. Pedrosa, *et al.*, Phys. Rev. Lett. **80**, 4438 (1998).
3. B. A. Carreras, B. Milligen, R. Balbin, *et al.*, Phys. Rev. Lett. **83**, 3653 (1999).
4. A. J. Krommes and E. M. Ottaviani, Phys. Plasmas **6**, 3731 (1999).
5. R. Metzler and J. Klafter, Phys. Rep. **339**, 1 (2000).
6. J. W. Haus and K. W. Kehr, Phys. Rep. **150**, 263 (1987).
7. A. S. Monin and A. M. Yaglom, *Statistical Fluid Mechanics* (Nauka, Moscow, 1965; MIT Press, Cambridge, 1975), Vols. 1, 2.
8. S. G. Samko, A. A. Kilbas, and O. I. Marichev, *Fractional Integrals and Derivatives, Theory and Applications* (Nauka i Tekhnika, Minsk, 1987; Gordon and Breach, Amsterdam, 1993).
9. M. B. Isichenko, Rev. Mod. Phys. **64**, 961 (1992).
10. A. J. Maida and P. R. Kramer, Phys. Rep. **314**, 237 (1999).
11. G. M. Zaslavsky and B. A. Niyazov, Phys. Rep. **283**, 73 (1997).
12. Yu. A. Dreĭzin and A. M. Dykhne, Zh. Éksp. Teor. Fiz. **63**, 242 (1972) [Sov. Phys. JETP **36**, 127 (1972)].
13. K. V. Chukbar, Zh. Éksp. Teor. Fiz. **108**, 1875 (1995) [JETP **81**, 1025 (1995)].
14. G. M. Zaslavsky, Chaos **4**, 253 (1994).
15. A. V. Chechkin and V. Yu. Gonchar, Zh. Éksp. Teor. Fiz. **118**, 730 (2000) [JETP **91**, 635 (2000)].
16. A. V. Gurevich, K. P. Zybin, and Ya. N. Istomin, Zh. Éksp. Teor. Fiz. **84**, 86 (1983) [Sov. Phys. JETP **57**, 51 (1983)].
17. N. L. Aleksandrov, A. M. Volchek, N. A. Dyatko, *et al.*, Fiz. Plazmy **14**, 334 (1988) [Sov. J. Plasma Phys. **14**, 196 (1988)].
18. A. V. Gurevich, Zh. Éksp. Teor. Fiz. **38**, 116 (1960) [Sov. Phys. JETP **11**, 85 (1960)].
19. A. V. Gurevich and Yu. N. Zhivlyuk, Zh. Éksp. Teor. Fiz. **49**, 214 (1965).
20. A. V. Gurevich and Ya. N. Istomin, Zh. Éksp. Teor. Fiz. **77**, 933 (1979) [Sov. Phys. JETP **50**, 470 (1979)].
21. O. G. Bakunin and S. I. Krasheninnikov, Fiz. Plazmy **21**, 532 (1995) [Plasma Phys. Rep. **21**, 502 (1995)].
22. S. I. Krasheninnikov, Zh. Éksp. Teor. Fiz. **94**, 166 (1988) [Sov. Phys. JETP **67**, 2483 (1988)].
23. G. G. Getmantsev, Astron. Zh. **39**, 607 (1962) [Sov. Astron. **39**, 477 (1962)].
24. T. H. Stix, Nucl. Fusion **18**, 353 (1978).
25. M. B. Isichenko, Plasma Phys. Controlled Fusion **33**, 795 (1991).
26. M. B. Isichenko, Plasma Phys. Controlled Fusion **33**, 809 (1991).
27. B. B. Kadomtsev and O. P. Pogutse, in *Proceedings of the 7th Conference on Plasma Physics and Controlled Nuclear Fusion Research, 1978* (IAEA, Vienna, 1978), Vol. 1, p. 649.
28. M. B. Isichenko and W. Horton, Comm. Plasma Phys. Controlled Fusion **14**, 249 (1991).

Translated by O.E. Khadin

Plasma Physics Reports, Vol. 30, No. 4, 2004, pp. 343–352. Translated from Fizika Plazmy, Vol. 30, No. 4, 2004, pp. 375–384.

LOW-TEMPERATURE PLASMA

Long-Lived Plasmoids as Initiators of Combustion of Gas Mixtures

I. A. Kossyĭ*, V. P. Silakov*, N. M. Tarasova*, M. I. Taktakishvili*, and D. van Wie**

** Prokhorov Institute of General Physics, Russian Academy of Sciences, ul. Vavilova 38, Moscow, 119991 Russia*

*** John Hopkins University, Laurel, MD, USA*

Received July 2, 2003

Abstract—A slipping surface discharge excited along a multielectrode metal–dielectric system in a chemically active (combustible) CH_4–O_2 mixture has been studied experimentally. Results obtained with the help of high-speed photography, shadowgraphy, optical spectroscopy, and piezoelectric measurements are presented. It is shown that the slipping surface discharge is a source of high-temperature, thermally equilibrium metal plasmoids whose lifetime is much longer than the plasma recombination time (long-lived plasmoids). The experimental investigation of the evolution of plasmoids introduced into a combustible gaseous medium allows one to conclude that the medium significantly increases the lifetime of plasmoids and that plasmoids, in turn, play an important role in the initiation of gas-mixture combustion. © *2004 MAIK "Nauka/Interperiodica".*

1. INTRODUCTION

Plasma objects with abnormally long lifetime (long-lived plasmoids) have been observed in laser sparks [1, 2], microwave discharges [3, 4], high-current arcs [5, 6], and other types of discharges. Interest in long-lived plasmoids generated under laboratory conditions can be attributed primarily to attempts at modeling ball lightning—an intriguing phenomenon that is still poorly understood [7, 8].

In recent years, however, the area of possible applications for long-lived plasmoids has expanded, particularly, in connection with the problem of the electric-discharge initiation of combustion in supersonic (hypersonic) gas flows.

Such flows are difficult to ignite with the help of conventional spark systems (analogous to a spark plug) in particular because of the short time $\tau_c \approx \delta/v$ during which a gas jet interacts with an electric-discharge plasma (here, δ is a characteristic discharge size and v is the flow velocity). At relatively small δ and large v, the interaction time can become shorter than the characteristic induction time τ_i required for igniting a mixture ($\tau_c < \tau_i$).

There are some straightforward ways of increasing τ_c up to values exceeding τ_i. One of them is to significantly increase δ as compared to the size of the usual spark produced between two electrodes. To implement this method of increasing the interaction time, it is necessary to create ignition systems extended in the flow direction.

There is, however, another method of solving this problem. The method implies that the electric discharge should be arranged in such a way that the plasma is detached from the discharge source and is injected in the form of a plasmoid into the gas flow, which entrains the plasmoid and carries it downstream from the source. In this case, the plasma–flow interaction time is determined by the plasmoid lifetime ($\tau_c \approx \tau_p$). So, if the latter exceeds the characteristic induction time τ_i, then the moving gaseous medium can be ignited. This method is similar to the ignition method in which highly heated small metal grains are injected into a gas flow [9], the only difference being that, here, long-lived plasmoids play the role of hot grains.

Both of the above methods can be implemented with the help of the multielectrode discharge systems that were designed at the Prokhorov Institute of General Physics, Russian Academy of Sciences, and are presently used in various applications, including the initiation of combustion in static (stationary) gas mixtures (see [10–12]). In this paper, it is demonstrated for the first time that the high-current slipping surface discharges excited in multielectrode discharge systems can be used as sources of long-lived plasmoids injected into a chemically active medium (combustible CH_4–O_2 or CH_4–OCH_4 + O_2–CFC mixtures).

2. EXPERIMENTAL SETUP

Figure 1 shows a schematic of a reactor with electric-discharge initiation of combustion.

Reactor chamber *2* is a cylindrical quartz tube with the diameter $D_c \cong 50$ mm and length $L_c \cong 100$–200 mm. The chamber is evacuated to a pressure of $p \leq 10^{-2}$ torr and filled with a working gas at a pressure of $100 \leq p \leq 500$ torr.

Combustion is initiated by multielectrode discharge system *1* described, e.g., in [13, 14]. The multielectrode discharge system used in this study is shown schemati-

1063-780X/04/3004-0343$26.00 © 2004 MAIK "Nauka/Interperiodica"

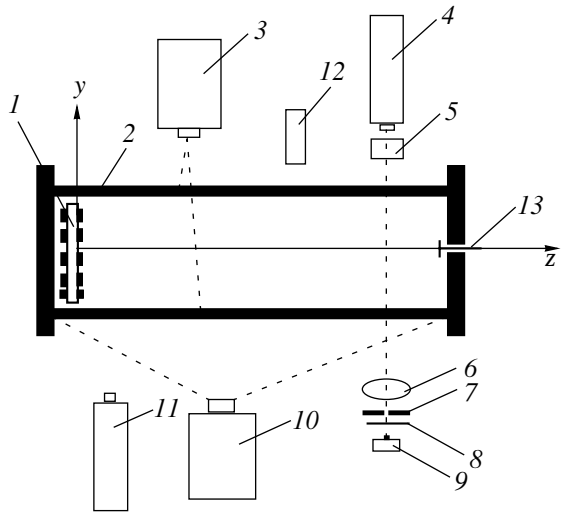

Fig. 1. Experimental setup: (*1*) multielectrode discharge system, (*2*) reactor chamber, (*3*, *10*) FÉR-7 streak cameras, (*4*) nitrogen laser, (*5*) telescope, (*6*) lens, (*7*) diaphragm, (*8*) UFS6 filter, (*9*) photographic camera, (*11*) spectrograph (S 2000 or HR 2000), (*12*) photomultiplier, and (*13*) piezoelectric transducer.

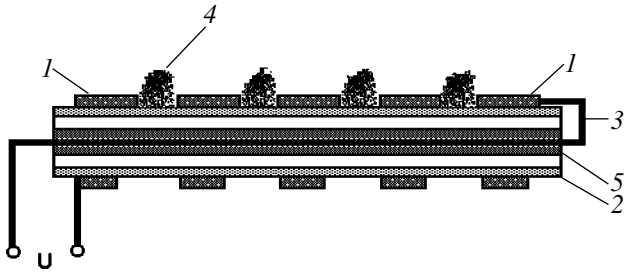

Fig. 2. Schematic of the multielectrode discharge system: (*1*) annular electrodes, (*2*) dielectric (quartz, ceramic, or fluoroplastic) tube, (*3*) return current conductor, (*4*) slipping-discharge plasma, and (*5*) quartz insulating tube.

cally in Fig. 2. This is a system of annular electrodes arranged on a dielectric (ceramic, fluoroplastic, or Plexiglass) tube with the diameter $D_d \cong 6$ mm. The return wire passes through the tube as is shown in Fig. 2. The multielectrode system is designed so that an applied high-voltage pulse with a sufficiently sharp leading edge generates a fast ionization wave that propagates along the multielectrode system and, in a fraction of a microsecond, shorts it out, thus resulting in a high-current ($I \leq 1$–10 kA) low-threshold slipping surface discharge consisting of a train of plasmoids generated in the interelectrode gaps. In our experiments, the slipping discharge was excited by high-voltage pulses with an amplitude of $U \geq 20$ kV and a pulse duration of $\tau_h \cong 10$–20 μs. Typical oscillograms of the discharge voltage and current are shown in Fig. 3.

The evolution of the discharge emission was studied with the help of FÉR-7 streak cameras (Fig. 1, items *3*, *10*). The camera slits could be oriented either along or across the chamber axis (the *z* axis) in order to trace the evolution of the axial and radial profiles of the discharge emission. The evolution of the emission integrated over the spectrum was measured with an FEU-106 photomultiplier (Fig. 1, item *12*).

The emission spectra were studied using S 2000 and HR 2000 (Ocean Optics) spectrographs (Fig. 1, item *11*).

Gas-dynamic perturbations of the working medium were recorded using the laser shadowgraphy technique based on a UV nitrogen laser (Fig. 1, item *4*).

Gas pressure variations at the chamber wall were measured with a piezoelectric transducer (Fig. 1, item *13*).

3. EXPERIMENTAL RESULTS

We studied the evolution of both the axial and radial profiles of the discharge emission. In the former case, the FÉR-7 slit was aligned with the chamber axis so as to view one of the interelectrode gaps, and in the latter case, the slit was oriented across the chamber axis. The measurements were performed for both chemically passive gaseous media (oxygen, argon, or methane) and chemically active (combustible) methane–oxygen and methane–oxygen–CFC mixtures.

The discharge stages preceding combustion were photographed with a sweep speed in the image plane of 75–250 μs/cm, while the time interval corresponding to volume combustion was examined at a sweep speed of 750 μs/cm.

Typical streak images are presented in Figs. 4–6. An analysis of the streak images shows the following:

(i) In all of the gaseous media (both chemically active and passive), the discharge gaps are sources of plasmoids that detach from the multielectrode discharge system and drift along the reactor axis (Figs. 4, 6a).

(ii) When the reactor is filled with a one-component gas (argon, methane, or oxygen), plasmoids generated by the multielectrode system exist for 200–300 μs, which is much longer than the discharge duration (~10–20 μs) and the characteristic recombination time. The plasmoids travel over a distance of 2–3 cm from the region of their origin and then disappear (Figs. 4, 6). The axial velocity of the plasmoids is usually lower than or close to the speed of sound.

(iii) The plasmoid lifetime significantly increases when the discharge chamber is filled with a combustible gas mixture (CH_4–O_2 or CH_4–O_2–CFC). The plasmoids move along the chamber axis for 1–3 ms until volume combustion begins, after which the original plasmoids transform into smaller and less bright plasmoids that continue moving in the axial direction (Fig. 5).

(vi) Streak images taken with slits oriented along and perpendicular to the z axis (Fig. 6) show that the transverse sizes of both the transformed (secondary) and original plasmoids are comparable to their axial sizes and are much smaller than the chamber radius.

The emission spectra of original plasmoids recorded with the S 2000 and HR 2000 spectrographs contain both the line and continuous components. Typical UV emission spectra are shown in Fig. 7. Figure 8 presents the continuum spectrum in the wavelength range $4500 \le \lambda \le 6500$ Å. The spectral intensity I_λ in this wavelength range is close to the equilibrium one [15]:

$$I_\lambda = (\text{const}/\lambda^4)[\exp(hc/\lambda kT) - 1]^{-1}. \quad (1)$$

Since the inequality $\exp(hc/\lambda kT) \gg 1$ is satisfied in this spectral range, Eq. (1) can be reduced to

$$1.4388 \times 10^8/\lambda = B - T\ln(I_\lambda \lambda^4), \quad (2)$$

where λ is in Å, T is the emitter (plasmoid) temperature in K, I_λ is in arbitrary units, and B is a constant independent of λ.

To determine the plasmoid temperature, we switch from the spectral intensity of the continuum and the wavelength to the variables $x = \ln(I_\lambda \lambda^4)$ and $y = 1.4388 \times 10^8/\lambda$ (Fig. 8). According to Eq. (2), the temperature is calculated from the slope of the averaged linear dependence $y(x)$. Thus, for the radiative temperature of the original plasmoid, we obtain $T \cong 5000$ K.

An analysis of the UV line spectrum shows that the main contribution to the spectrum comes from electronically excited atoms and ions of the electrode material (in Fig. 7, this is Ti).

A streak image shown in Fig. 9 illustrates the evolution of a discharge over a relatively long time interval (about 3 ms). The reactor chamber is filled with a methane–oxygen mixture. The streak-camera slit is oriented along the z axis. In this photograph, one can distinguish several phases. The vertical line on the left of the figure corresponds to an emission burst related to the active phase of the multielectrode system operation. This phase lasts for several tens of microseconds ($\Delta t_1 \cong 10$–20 μs). The inclined line originating at the multielectrode system is the trajectory of a plasmoid that is generated on the surface of the multielectrode system and is then accelerated along the z axis. The wider initial segment of the line corresponds to the motion of the original plasmoid that is generated in all of the gaseous media, regardless of their chemical activity. This phase, with a duration of $\Delta t_2 \cong 300$ μs, is represented in more detail in Figs. 4 and 5. The thinner extension of the line corresponds to the motion of the transformed plasmoids that exist in combustible mixtures only. The axial velocity of the plasmoid is $(1–2) \times 10^4$ cm/s. Several oscillations of the long-lived plasmoid between the chamber ends (with a total duration of Δt_3 0.5–1.0 ms) are followed by volume combustion rapidly expanding over the chamber.

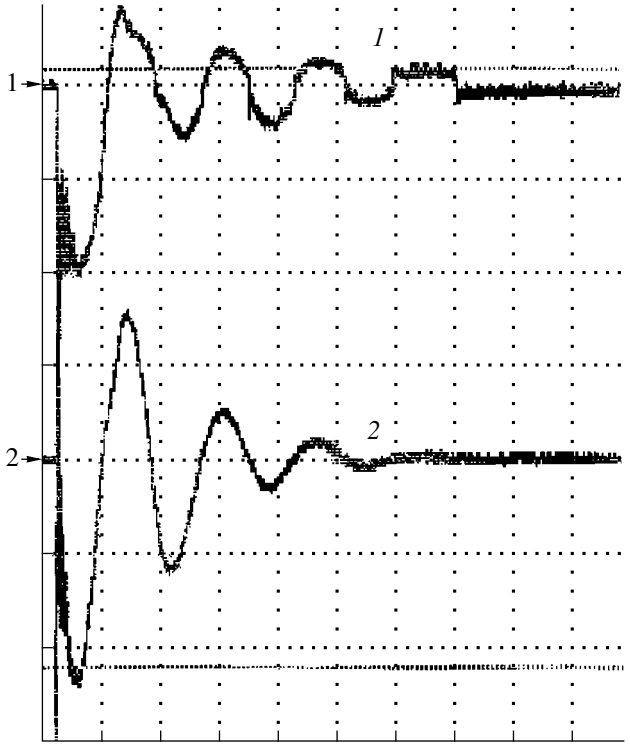

Fig. 3. Oscillograms of the (*1*) discharge voltage (5 V/division) and (*2*) current (200 A/division) in the multielectrode discharge system (discharge in air, p = 200 torr). The time scale is 500 μs/division.

The behavior of the gas mixture combustion is reflected in the signals from the photomultiplier and piezoelectric transducer (see Fig. 10a). For comparison, Fig. 10b shows the corresponding signals for the case of a chemically passive medium (air). The waveform of the photomultiplier signal has a sharp peak corresponding to the emission burst in the active phase of the discharge. Nearly 500 μs later, a component corresponding to volume combustion appears in the photomultiplier signal shown in Fig. 10a. The duration of the mixture combustion is about 1.0–1.5 ms. The oscillograms clearly exhibit spikes corresponding to emission oscillations against the background of uniform combustion (see Fig. 9).

The signal from the piezoelectric transducer also demonstrates oscillations correlating with emission modulations from the burning gas mixture.

The shadowgraphs in Fig. 11 indicate the presence of a shock wave generated by the multielectrode discharge system, as well as perturbations related to the axial motion of plasmoids. The shock-wave velocity in one-component gases is nearly the same as in combustible gas mixtures and amounts to $\sim 4.6 \times 10^4$ cm/s. The axial velocity of the gas perturbations accompanying the shock wave propagation in a methane–oxygen mix-

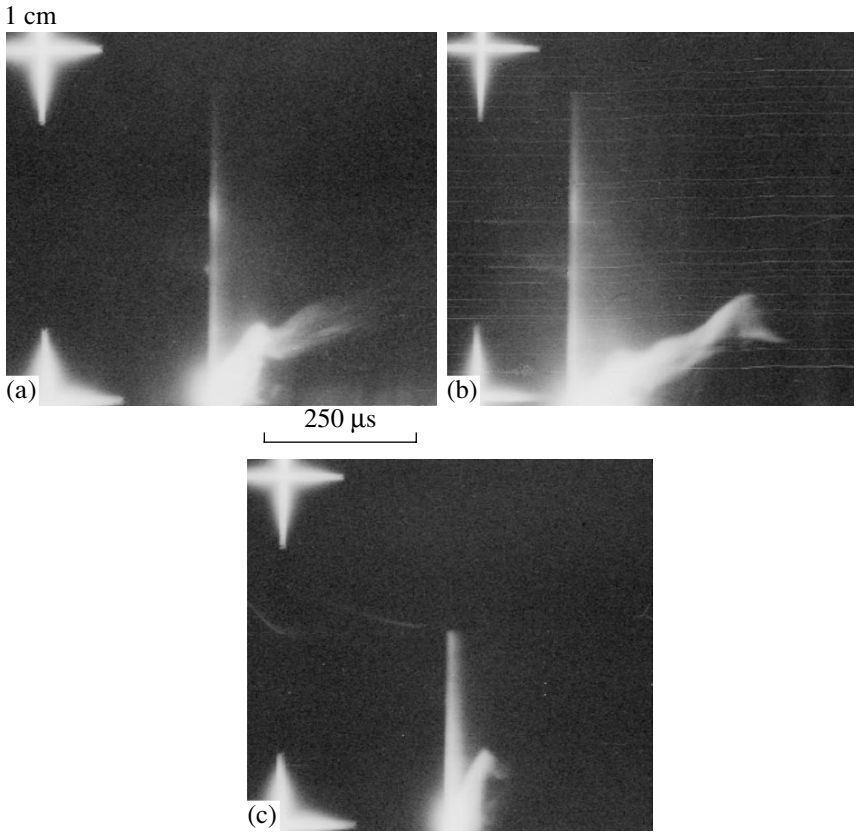

Fig. 4. Streak images of discharges in (a) oxygen, (b) argon, and (c) methane at a pressure of $p = 150$ torr. The camera slit is oriented along the z axis.

ture (Figs. 11a–11e) is close to the plasmoid velocity and amounts to $(1–2) \times 10^4$ cm/s.

4. DISCUSSION OF EXPERIMENTAL RESULTS

Electric discharges are widely applied to initiate the combustion of gas mixtures (see, e.g., monographs [16–18]). As a rule, a low-power spark excited between two electrodes imbedded in a combustible gaseous medium (analogous to the spark plugs employed in internal-combustion engines) is used for this purpose. In this study, as in our previous works [10–12], the ordinary spark is replaced with a high-current pulsed slipping surface discharge.

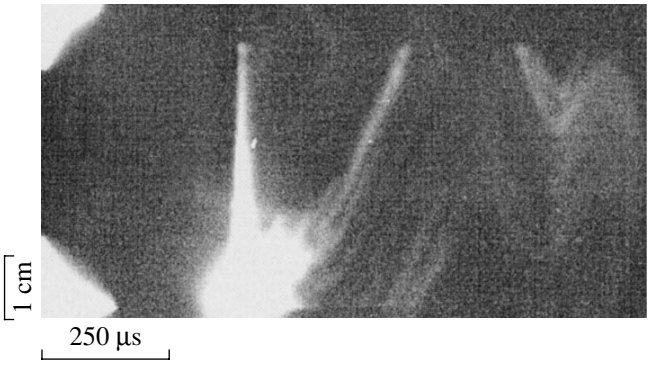

Fig. 5. Streak image of a discharge in the combustible $CH_4 : O_2$ (45 : 180 torr) mixture. The camera slit is oriented along the z axis.

The use of this type of initiator significantly changes the character of the gas combustion far from the initiator as compared to the case of the usual low-power initiation or initiation with the help of a filament heater. When combustion is initiated by a slipping surface discharge, the ordinary combustion dynamics, which is described by a heat or detonation wave propagating from the breakdown region, is replaced with a complicated sequence of phenomena. A very short initiating discharge (from several tens of nanoseconds to several microseconds) is followed by a long (from 0.5 to 2 ms) pause (the induction phase). The gas mixture then ignites almost simultaneously throughout the entire reactor chamber. Both the induction time and the combustion duration depend significantly on the energy released in the slipping surface discharge; specifically, they increase as the released energy decreases.

In this case, the problem of the mechanisms responsible for the activation of a gaseous medium during the induction phase becomes of primary importance. In [10–12], it was found by analyzing streak images (similar to those in Fig. 9) that, in the induction phase, there is a glow region propagating along the *z* axis and oscillating between the ends of the reactor. However, the nature of this glow, which is apparently related to processes resulting in the activation of a gaseous medium, remained poorly understood, and the phenomenon itself was called "the incomplete-combustion wave."

Based on the results of the present experiments, we can assume that the activation of the gaseous medium (which gives rise to chain branching reactions constituting the basis for an explosive combustion) is a consequence of the generation of long-lived high-temperature plasmoids interacting with the ambient gas.

The original plasmoids generated near the surface of the multielectrode system and accelerated along the chamber axis are plasma objects that are in a nearly equilibrium thermal state with a temperature of $T_p \cong$ 5000 K. This explains the fact that plasmoids continue to exist after the active discharge phase over a time that is much longer than the recombination time. The plasmoids are apparently generated in the course of microscopic explosions on the electrode surface. It was shown in [13] that, in vacuum discharges excited by multielectrode systems similar to the one used in the present experiments, plasmoids ejected from the discharge system are plasma objects consisting mainly of metal ions of the electrode material. In a more recent paper by Batrakov *et al*. [19], it was shown experimentally that metal drops leaving the cathode spot of a vacuum arc evaporate intensively and convert into plasma bunches in the immediate vicinity of the cathode surface. The present study demonstrates for the first time that explosive-emission effects accompanied by the generation of metal plasmoids occur not only in high vacuum, but also in gases at high pressures (up to atmospheric). This result is of great interest and deserves particular consideration.

Penetrating into a one-component (chemically passive) gaseous medium, a primary plasmoid is cooled mainly through radiative losses. The lifetime of a plasma bunch in this case is determined by its characteristic cooling time.

The situation is quite different when a plasmoid falls into a combustible (chemically active) gaseous medium. The high temperature of the plasma bunch stimulates the combustion processes in the ambient gas and thus forms an oppositely directed (from the outside into the plasmoid) heat flux that compensates for the radiative losses. As a result, favorable conditions arise for a substantial increase in the lifetime of the plasmoid, whose interaction with a CH_4–O_2 mixture stimulates exoenergic oxidation processes and formaldehyde production. If the formaldehyde content exceeds a certain critical value, then chain branching processes come into play [20], which results in the fast (explosive) combustion of the gas in the reactor volume.

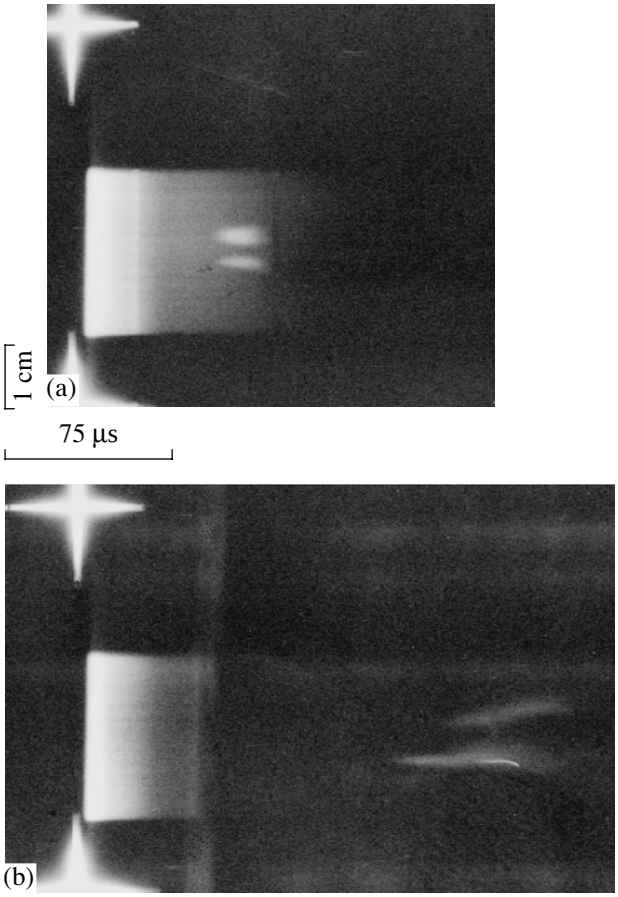

Fig. 6. Streak images of a discharges in (a) argon (p = 200 torr) and (b) the combustible CH_4 : O_2 mixture (45 : 80 torr) at distances of L = (a) 2.0 and (b) 2.5 cm from the multielectrode system along the z axis. The camera slit is orthogonal to the z axis.

The axial propagation of a plasmoid may be attributed to the motion of the heated gas behind the front of a shock wave propagating from the multielectrode system, as is seen in the shadowgraph shown in Fig. 11. The original plasmoids can also acquire an axial momentum due to the action of electrodynamic forces on the slipping-discharge plasma. These forces should certainly be present in our multielectrode discharge system because of the specific arrangement of the return current conductor (see Fig. 2).

The qualitative picture discussed above is also confirmed by estimates showing that the model proposed is basically applicable to the phenomena observed in our experiments.

First of all, let us estimate the lifetime τ_p of an original, thermally equilibrium plasma bunch (more exactly, the characteristic decay time of the bunch glow) in a chemically passive gaseous medium assum-

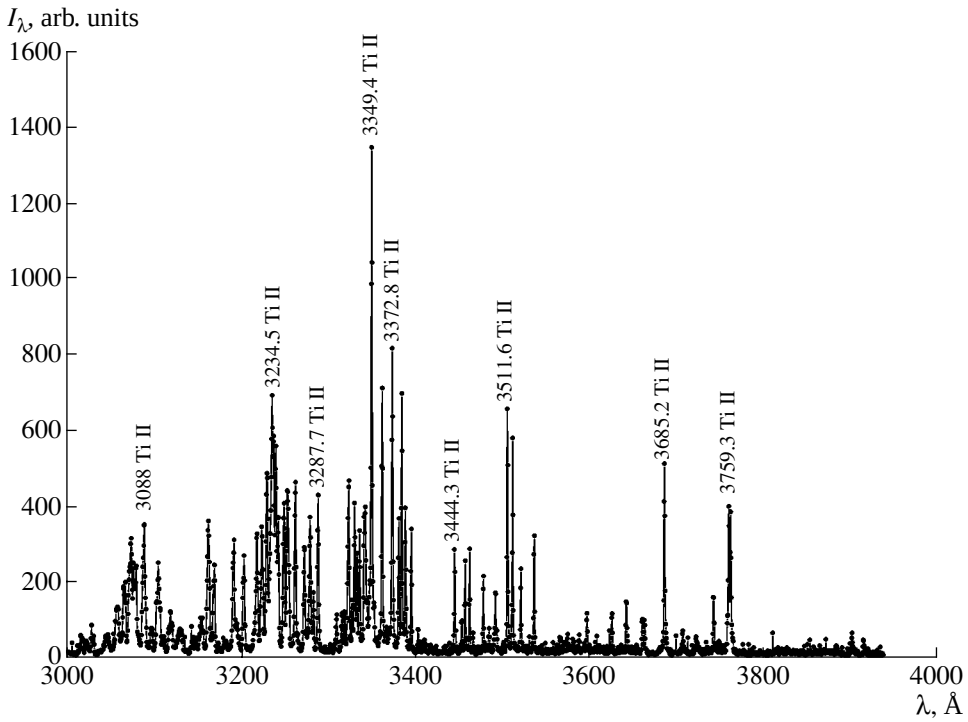

Fig. 7. Emission spectrum of an original plasmoid. The electrodes were made of titanium.

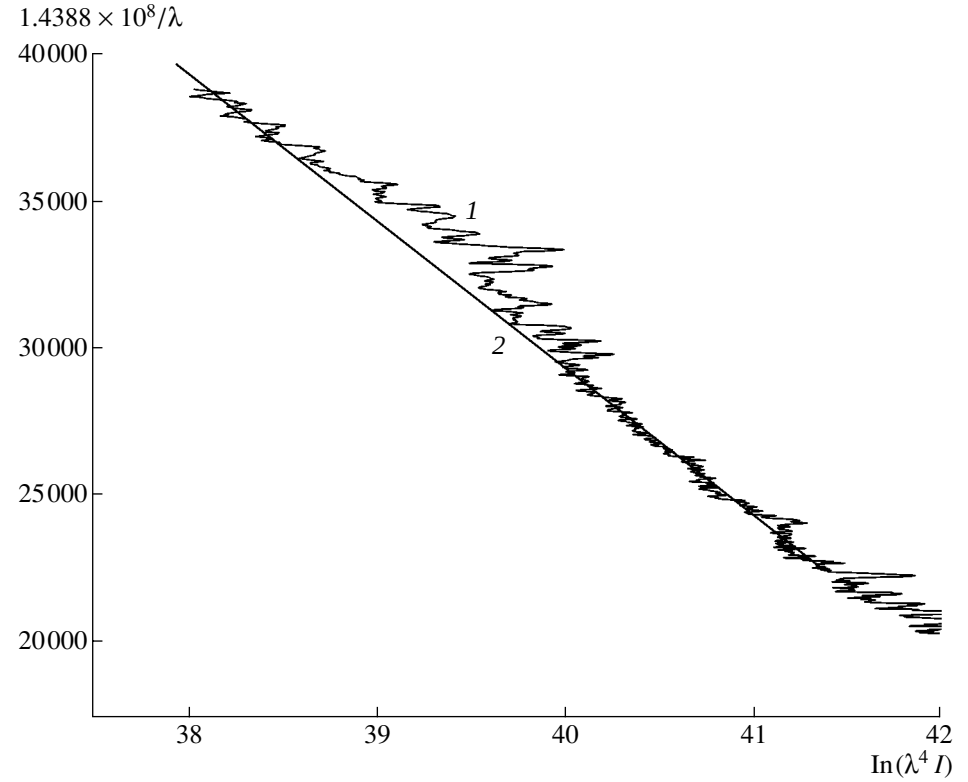

Fig. 8. (*1*) Continuum spectrum of an original plasmoid and (*2*) its fit by formula (2) at $T \cong 4800$ K.

ing that the bunch is primarily cooled through radiative losses. In the isobaric approximation, the time in which the emission power decreases by a factor η is determined by the expression

$$\Delta t_\eta = (c_p/k)p_0\int_{T_\eta}^{T_0} dT'/(T'J(T')), \quad (3)$$

where p_0 is the pressure (both inside and outside the plasmoid), $J(T)$ is the integral (over the spectrum) plasma emissivity, T_0 is the initial plasmoid temperature, and T_η is the plasmoid temperature corresponding to the emission power $P_\eta \approx P_0/\eta$ (P_0 is the plasmoid emission power at $T = T_0$).

Spectral measurements show that, at $p_0 \cong 200$ torr, the temperature of an original titanium plasmoid is $T_0 \cong 5000$ K. From this, it is easy to estimate the density of titanium ions ($n_{\mathrm{Ti}+}$) and atoms (n_{Ti}), as well as the electron density n_e in the plasmoid:

$$n_{\mathrm{Ti}}(T_0) = p_0/kT_0 \approx 4\times 10^{17}\ \mathrm{cm}^{-3},$$
$$n_e(T_0) = n_{\mathrm{Ti}+}(T_0) \approx \sqrt{n_{\mathrm{Ti}}(T_0)(2u_{\mathrm{Ti}+}(T_0)/u_{\mathrm{Ti}}(T_0))(m_e kT_0/2\pi\hbar^2)^{3/2}\exp(-I_{\mathrm{Ti}}/kT_0)} \approx 1.34\times 10^{16}\ \mathrm{cm}^{-3}. \quad (4)$$

Here, $u_{\mathrm{Ti}+}$ and u_{Ti} are the electronic static sums of Ti^+ ions and Ti atoms, respectively, and I_i is the ionization energy of titanium atoms ($I_{\mathrm{Ti}} \cong 6.8$ eV).

If radiative losses related to line emission are ignored, then we have [21]

$$J(T_0) = 1.42\times 10^{-37}T_0^{1/2}n_{\mathrm{Ti}+}(T_0)n_e(T_0) \times (1 + |E_g|/kT_0) \cong 2.71\times 10^{-2}\ \mathrm{kW/cm}^3, \quad (5)$$

where $E_g = -(I_{\mathrm{Ti}} - E^*)$, with E^* being the energy of the lower electronically excited atomic state ($E^* \cong 0.813$ eV).

If the plasmoid temperature is somewhat lower, e.g., $T_1 \cong 4700$ K, then we find

$$n_{\mathrm{Ti}}(T_1) = 4.25\times 10^{17}\ \mathrm{cm}^{-3};$$

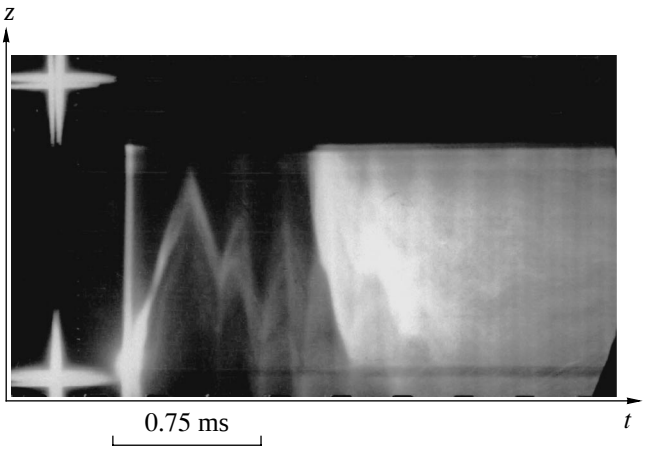

Fig. 9. Typical streak image of combustion initiation in a $CH_4 : O_2$ mixture. The camera slit is oriented along the z axis. Bright crosses on the left of the figure are markers.

$$n_e(T_1) = n_{\mathrm{Ti}+}(T_1) \cong 8.05\times 10^{15}\ \mathrm{cm}^{-3};$$
$$J(T_1) \cong 9.98\times 10^{-3}\ \mathrm{kW/cm}^3.$$

In this case, we have

$$\eta = P_0/P_1 = J(T_0)V_{p(0)}/J(T_1)V_{p(1)} \cong J(T_0)T_0/J(T_1)T_1 \approx 3. \quad (6)$$

Defining the plasmoid lifetime as the time during which the plasmoid emission power decreases by a factor of 3, we find

$$\tau_p \cong \Delta t_{\eta=3} = 2.5p_0\int_{T_1}^{T_0} dT'/(T'J(T')) \cong 270\ \mu\mathrm{s}, \quad (7)$$

which is close to the lifetime determined experimentally from streak images similar to those presented in Fig. 4.

Let us assume that the primary (titanium) plasmoid radiates the power given by expression (5) and consider the case in which this plasmoid falls into a chemically active gaseous medium. A situation can then occur in which the plasmoid radiative losses are compensated for by the energy influx from the ambient medium. In this case, the lifetime of the plasma bunch can increase to values substantially exceeding the induction time τ_i. The energy balance in this case is written as

$$JV_p \approx \Gamma\varepsilon_c S_p, \quad (8)$$

where V_p and S_p are the volume and the surface area of a spherical plasmoid, $\Gamma \cong -D_0\nabla n_0$ is the flux density of chemically active particles with a density n_0 arriving from the ambient medium (in our experiments, methane and oxygen molecules) into the plasma bunch, D_0 is the diffusion coefficient of these particles, and ε_c is the chemical energy released in the oxidation reactions

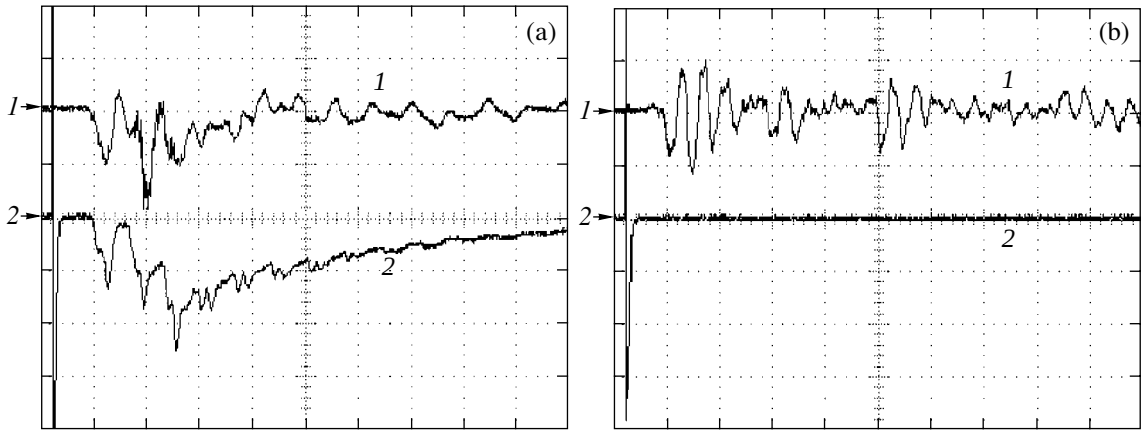

Fig. 10. Signals from (*1*) the piezoelectric transducer (5 V/division in plot (a) and 500 mV/division in plot (b)) and (*2*) the collimated photomultiplier (500 mV/division) for the cases of (a) the combustible $CH_4 : O_2$ mixture (60 : 240 torr) and (b) a chemically passive gas (air) at a pressure of p = 300 torr. The time scale is 500 μs/division.

stimulated by the high-temperature plasmoid. It follows from equality (8) that, at a certain radiative loss power J, radiative losses can be compensated for by an oppositely directed heat flux only at a sufficiently small size of the plasmoid: $r_p \leq r_k$. Assuming that $r_p \cong 0.05$ cm and $J \cong 2 \times 10^{-2}$ kW/cm^3, we find that, at p_0 = 300 torr, equality (8) holds even at ε_c values as low as $\approx 10^{-3}$ eV.

A plasmoid converts the chemical energy of a methane–oxygen mixture into heat and partially returns it into the ambient medium through radiation and heat conduction. This results in the heating of the surrounding gas and the gasdynamic perturbations that accompany this heating. The aforesaid, in our opinion, is demonstrated by the shadowgraphs presented in Fig. 11.

The hard component of the plasmoid emission probably plays a significant role in the heating of the ambient gaseous medium by activating the combustible gas mixture, as was pointed out in [11].

Comparing typical streak images (Fig. 9) with shadowgraphs (Fig. 11) and the signals from the multiplier and piezoelectric transducer (Fig. 10), we can conclude that plasmoids moving in a combustible gaseous medium are sources of gasdynamic perturbations that result in both repetitive "impacts" on the opposite end of the chamber and reflections of combustion-initiating plasmoids from this end.

In the monograph [8], a conclusion was drawn based of a number of accidental observations and a limited number of not very enlightening experiments that metal plasma bunches can sustain themselves in the atmosphere regardless of the mechanism for their formation. We consider the analogies with ball lightning drawn in [8] to be insufficiently justified and remark only that our experiments, which were performed with a multielectrode discharge system generating a train of metal plasmoids, have revealed a substantial increase in the lifetime of plasma bunches in a chemically active gaseous medium.

The investigations reported in the present paper show, in our opinion, that the study of the behavior of a small gas volume heated in one way or another to a high (on the order of $(4–5) \times 10^3$ K) temperature and introduced into a chemically active (combustible) gas mixture is a very challenging problem. This problem was earlier considered in a number of papers (see, e.g., [18, 22, 23]); however, the inverse effect of the medium on the introduced local temperature perturbation through the oppositely directed flux of electrochemical energy, as well as the fact that the medium can be activated by radiation from the local high-temperature region, was not taken into account. Thus, the model proposed by Zel'dovich [22, 23] considers a point heat source (spark) that liberates a certain amount of heat Q_{cal} at the time t = 0. Using this model, the cooling by heat conduction, the expansion of the energy liberation region, and the initiation of combustion under given initial conditions of energy liberation were calculated. Taking into account not only heat conduction losses, but also radiative losses and the inverse action of the medium on the gas volume heated by a spark and the change in the medium state under the action of the emitted radiation (see [11]), can substantially affect the lifetime of the locally heated gas volume and the character of combustion initiation.

The results obtained in this paper are of interest, in particular, for solving the problem of combustion initiation in supersonic (hypersonic) flows of combustible gas mixtures. A plasmoid introduced into the flow can move with the gas for quite a long time until it provokes an explosive combustion far from the discharge initiator. The distance traveled by a plasmoid from the point of its generation to the region where the volume com-

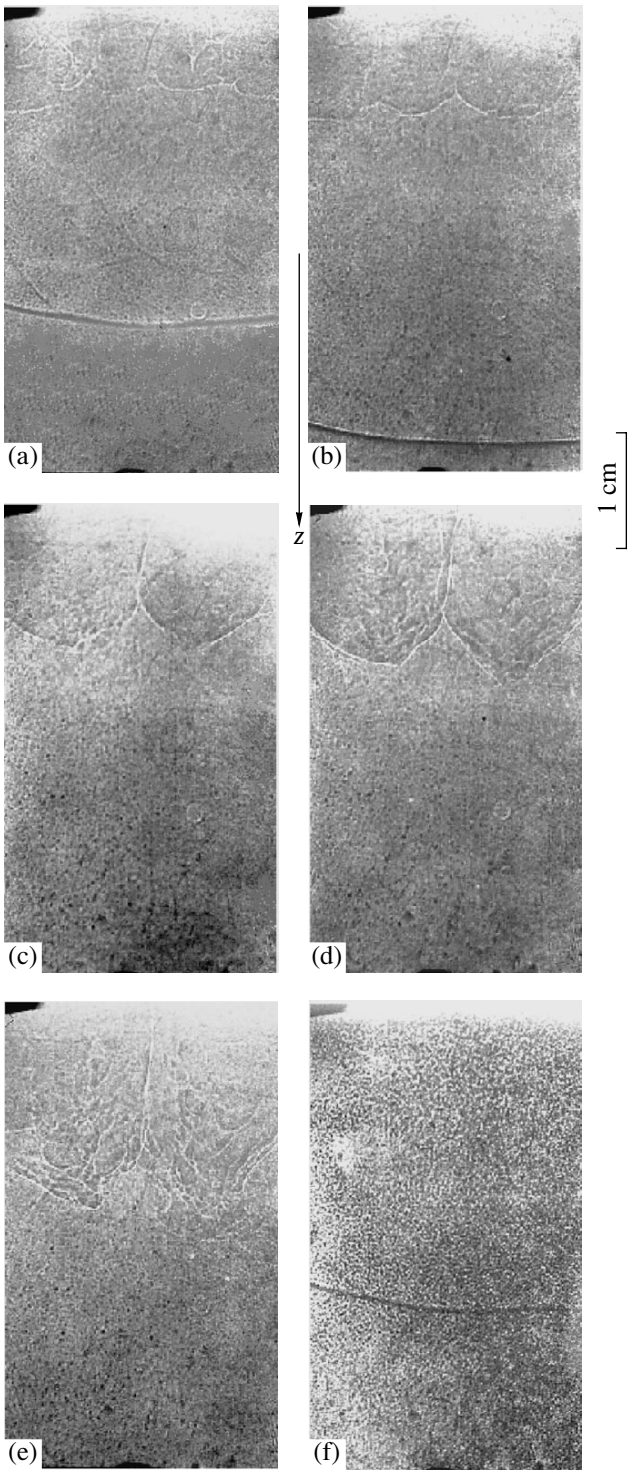

Fig. 11. Shadowgraphs of combustion initiation in (a)–(e) the $CH_4 : O_2$ mixture (60 : 240 torr) and (f) a chemically passive gas (air) at different instants: Δt = (a) 50, (b) 70, (c) 100, (d) 130, (e) 160, and (f) 50 μs.

bustion occurs depends on both the flow velocity and the energy released in the electric discharge initiating combustion.

5. CONCLUSIONS

Our experiments have shown that a slipping surface discharge excited along a multielectrode metal–dielectric system is a source of long-lived, thermally equilibrium plasmoids with a lifetime much longer than the plasma recombination time. When these plasmoids are injected into a chemically inactive gaseous medium, their lifetime is determined by the radiative loss time. On the other hand, when plasmoids are injected into a chemically active (combustible) gaseous medium, their lifetime increases substantially, which may be attributed to the balance between radiative losses and the energy influx from the chemically reacting particles of the combustible gas mixture. The plasmoid sustained by a chemically active medium, in turn, affects the latter by activating the gas mixture and promoting its combustion.

The results obtained show that the generation of long-lived plasmoids holds promise as a method for initiating combustion in supersonic gas flows.

ACKNOWLEDGMENTS

We thank S.M. Temchin and V.A. Kaminskiĭ for fruitful discussions. This work was supported in part by the Russian Foundation for Basic Research (project no. 02-02-16066) and by ISTC and EOARD (the ISTC project no. 2681p).

REFERENCES

1. G. A. Askar'yan, M. S. Rabinovich, M. M. Savchenko, and A. D. Smirnova, Pis'ma Zh. Éksp. Teor. Fiz. **1**, 18 (1965) [Sov. Phys. JETP **1**, 162 (1965)].
2. G. A. Askar'yan, M. S. Rabinovich, M. M. Savchenko, and V. K. Stepanov, Pis'ma Zh. Éksp. Teor. Fiz. **3**, 465 (1966) [Sov. Phys. JETP **3**, 303 (1966)].
3. P. L. Kapitsa, Zh. Éksp. Teor. Fiz. **57**, 1801 (1969) [Sov. Phys. JETP **30**, 973 (1969)].
4. J. R. Powell and D. Finkelstein, Am. Sci. **58**, 2318 (1970).
5. A. G. Basiev, F. I. Vysikaĭlo, V. A. Gurashvili, and E. R. Shchekotov, Fiz. Plazmy **9**, 1076 (1983) [Sov. J. Plasma Phys. **9**, 627 (1983)].
6. A. P. Ershov, S. P. Bytskevich, I. B. Timofeev, and S. N. Chuvashev, Teplofiz. Vys. Temp. **28**, 583 (1990).
7. B. M. Smirnov, *The Problem of Ball Lightning* (Nauka, Moscow, 1988).
8. J. D. Barry, *Ball Lightening and Bead Lightening: Extreme Forms of Atmospheric Electricity* (Plenum Press, New York, 1980; Mir, Moscow, 1983).
9. W. Jost, *Explosion and Combustion Processes in Gases* (McGraw Hill, New York, 1946; Inostrannaya Literatura, Moscow, 1952).
10. S. I. Gritsinin, I. A. Kossyi, M. A. Misakyan, *et al.*, J. Thermophys. Heat Transfer **16**, 450 (2002).
11. I. A. Kossyĭ, V. P. Silakov, and N. M. Tarasova, Fiz. Plazmy **27**, 757 (2001) [Plasma Phys. Rep. **27**, 715 (2001)].

12. S. I. Grytsinin, E. G. Korchagina, I. A. Kossyi, *et al.*, Plasma Sources Sci. Technol. **10**, 125 (2001).
13. A. M. Anpilov, E. M. Barkhudarov, N. K. Berezhetskaya, *et al.*, Plasma Sources Sci. Technol. **7**, 141 (1998).
14. Yu. B. Bark, E. M. Barkhudarov, Yu. N. Kozlov, *et al.*, J. Phys. D **33**, 859 (2000).
15. Ya. B. Zel'dovich and Yu. P. Raizer, *Physics of Shock Waves and High-Temperature Hydrodynamic Phenomena* (Nauka, Moscow, 1966; Academic Press, New York, 1967).
16. N. N. Semenov, *Some Problems of Chemical Kinetics and Reaction Ability* (Izd. Akad. Nauk SSSR, Moscow, 1958).
17. B. Lewis and G. von Elbe, *Combustion, Explosions, and Flame in Gases* (Academic, New York, 1987; Mir, Moscow, 1968).
18. E. S. Shchetinkov, *Physics of Gas Combustion* (Nauka, Moscow, 1965).
19. A. V. Batrakov, N. I. Vogel, S. A. Popov, *et al.*, IEEE Trans. Plasma Sci. **30**, 106 (2002).
20. N. N. Semenov, *Chain Reactions* (Nauka, Moscow, 1986).
21. Yu. P. Raizer, *Gas Discharge Physics* (Nauka, Moscow, 1987; Springer-Verlag, Berlin, 1991).
22. Ya. B. Zel'dovich, Zh. Éksp. Teor. Fiz. **11**, 159 (1941).
23. Ya. B. Zel'dovich and I. Simonov, Zh. Fiz. Khim., No. 11 (1949).

Translated by N.F. Larionova